Seismic anisotropy of surface waves from 6C ground motions

Le Tang

München 2024

Seismic anisotropy of surface waves from 6C ground motions

Dissertation
zur Erlangung des Doktorgrades
an der Fakultät für Geowissenschaften
der Ludwig-Maximilians-Universität München

vorgelegt von
Le Tang

aus
Suzhou, China

München, den 26.09.2024

Erstgutachter:	Prof. Dr. Heiner Igel
Zweitgutachter:	Prof. Dr. Jean-Paul Montagner
Tag der mündlichen Prüfung:	07.02.2025

Contents

List of Figures

List of Tables

Abstract

Rotational ground motion is the angle of ground rotation observed during the deformation of the Earth. The ratio of rotational amplitude to translational motion offers insights into local structure. Over the past few decades, studies on the Earth's internal structure have mainly relied on the time difference of seismic waves to calculate azimuth-related velocity changes, namely azimuthal anisotropy. However, heterogeneity often affects studying anisotropy based on seismic wave travel time, especially in highly complex structures such as southern California. The splitting of shear waves can effectively constrain the anisotropy in the lateral direction, but its depth resolution is limited. To address these challenges, this thesis proposes a new theory that uses the amplitude ratio of 6C (three-component translation and three-component rotation) ground motion to extract the phase velocity of surface waves. The underground medium's azimuthal anisotropy can be characterized by observing 6C surface wave waveforms from different azimuths. The amplitude ratio provides information about the local azimuth-dependent surface wave dispersion relation of the subsurface beneath the 6C station without requiring knowledge of the sources or structures along the path. To validate this theory, active source experiments based on teleseismic surface waves are conducted to study the anisotropy of the upper mantle in southern California. The results indicate that the proposed method makes it possible to retrieve local anisotropy in the upper mantle with well-determined azimuthal anisotropy of the asthenosphere. The observed fast axes suggest local rapid changes in plate deformation and complex mantle flow patterns, offering new insights into geodynamic processes in the region. Furthermore, the interaction of ocean waves with the solid Earth generates two main signals, known as microseisms. These microseisms provide valuable information about the energy exchange between different Earth systems. The 6C motions of a small seismic array at Piñon Flat Observatory (PFO) in southern California make it possible to examine the seasonal azimuth variation of the two main microseismic sources: primary and secondary. Based on the 6C ambient noise source, we develop a new theory with significant practical implications for the field. This theory is based on anisotropy imaging of the 6C ambient noise source, which allows us to measure local seismic anisotropy from 6C cross-correlation functions (CCF) of ambient seismic noise data. The results indicate that the stress-induced anisotropy is well resolved and compatible with other tomography results, providing constraints on the origin of depth-dependent seismic anisotropy. The practical applications of the proposed 6C anisotropy theory demonstrate its potential to enhance our understanding of Earth's anisotropy and its impact on Earth science.

Chapter 1

Introduction

Rotational motion can be directly measured as part of the wavefield gradient using rotational seismographs (Lefevre, 2014; Bernauer et al., 2021; Zembaty et al., 2021; Igel et al., 2007, 2021; Fang & Tang, 2021). With the development of rotational ground motion instruments such as ring lasers (Schreiber et al., 2014; Igel et al., 2005, 2021) or fiber optic gyroscopes (Schreiber et al., 2009), various techniques have been developed to exploit the resulting observations. This has opened up new opportunities for single-station seismological observations, which are crucial for planetary exploration, seafloor observation, and volcanology.

By applying adjoint techniques to such joint observations (Fichtner & Igel, 2009), it demonstrates that 6C (three-components translation and three-components rotation) amplitude ratios are sensitive to near-receiver structures, thereby eliminating path effects of wave propagation. Assuming an isotropic medium or a transversely isotropic (VTI) medium with a vertical axis of symmetry, only S-related waves can produce rotational motion (Tang & Fang, 2021a). This allows us to identify and separate wavefields using polarization properties uniquely (Sollberger et al., 2018; Schmelzbach et al., 2018; Wassermann et al., 2022). Since the rotational component of the S-related wave is perpendicular to the wave propagation direction and should have the same phase as the corresponding translational displacement, the propagation azimuth of an earthquake can also be easily estimated using a single 6C station (Igel et al., 2007; Wassermann et al., 2016; Yuan et al., 2021). The method of estimating local phase velocity from 6C amplitude ratios has been verified by actual observations (Igel et al., 2007; Keil et al., 2021; Fang & Tang, 2021).

Furthermore, Tang & Fang (2023) provided a theoretical formula for the cross-correlation between displacement and rotation and theoretically demonstrated that local phase velocity can also be extracted from the amplitude ratio of ambient seismic noise. Additionally, Noe et al. (2022) numerically exploited the rotational motion of body waves in general anisotropic media. They demonstrated the feasibility of inverting local anisotropic elastic parameters from rotational motion and strain by estimating body wave velocities from amplitude ratios. However, there is no study on the anisotropy of 6C surface waves, but this is of great significance for anisotropy study. Therefore, our study aims to retrieve local anisotropy parameters of subsurface structures from surface waves using translational

displacement and rotation or strain since the amplitude ratio method possesses a locally sensitive kernel, which is a great advantage for studying seismic anisotropy.

Seismic anisotropy has become a separate field, connecting material properties, stress alignment heterogeneity, or pore space with dynamic phenomena such as mantle flow or fluid flow direction (Anderson, 1965; Crampin, 1977; Forsyth, 1975; Anderson & Dziewonski, 1982; Montagner & Tanimoto, 1991; Nataf et al., 1984; Legendre et al., 2021). A comprehensive understanding of seismic anisotropy helps characterize subsurface structures and seismic hazards (Gupta, 1973; Legendre et al., 2021; Teanby et al., 2004). Previous studies have mainly focused on translational displacements, encompassing P-wave azimuthal anisotropy (Hess, 1964; Francis, 1969), P-wave polarization (Schulte-Pelkum et al., 2001; Al-Lazki et al., 2004; Mutlu & Karabulut, 2011), shear wave splitting (Crampin & Chastin, 2003; Vinnik et al., 1989; Silver, 1996), surface wave azimuthal anisotropy, and polarization analysis (Forsyth, 1975; Hess, 1964; Tanimoto & Anderson, 1985; Montagner & Nataf, 1986; Maupin, 1989; Montagner & Tanimoto, 1991).

Azimuthal anisotropy can be studied through surface wave dispersion by determining dispersion curves at different azimuthal angles using single-station, inter-station, or array-based methods. While single-station methods are mainly used to measure fundamental mode dispersion curves (Levshin et al., 1972; Forsyth, 1975; Ekström et al., 1997), more complex methods require prior information about source functions or approximate earth structure (Brown et al., 2022), which limits their application scope. On the other hand, inter-station or array-based methods use the phase difference between seismograms measured at different stations to estimate phase velocity and have been successfully applied to seismic ambient noise combined with cross-correlation analysis (Yao et al., 2006, 2008; Stehly et al., 2009; Legendre et al., 2021; Shapiro & Campillo, 2004; Shapiro et al., 2005).

The limitation of the traditional single-station method or multi-station method is that the dispersion measurement yields the average velocity between the source (active source or passive source) and the station, even though the average inter-station dispersion can be related to the local phase velocity by integration over the inter-station arc (Legendre et al., 2021). Heterogeneity can significantly affect the results using these methods. Single-point anisotropy analysis of surface wave polarization motion (Park & Yu, 1993; Tanimoto, 2004) aims to retrieve azimuthal variations in amplitude or amplitude ratio and obtain constraints on the anisotropic structure directly below the receiver. However, the polarization anomaly at a given station depends on the structure below the station and the structure seen by the wave in a large part of the propagation path unless the structure is uniformly anisotropic over a large area (Maupin, 2004). Due to the limitations of the surface wave anisotropy analysis mentioned above (such as heterogeneity effects and polarization complexity), this paper first attempts to find a method based on 6C observations to characterize the azimuthal anisotropy of the subsurface structure without being affected by along-path heterogeneity or source effects.

Seismic anisotropy informs us about the alignment of small-scale heterogeneity, such as fractures, porous media, crystals, or bedding, often oriented according to the local stress or strain field (Tanimoto & Anderson, 1984; Ribe, 1989; Ghosh & Holt, 2012; Montagner, 1994). This alignment can be connected to the flow direction of the Earth's mantle.

The seismic anisotropy in the upper mantle reveals geodynamic processes and the tectonic evolution of the Earth. The two most powerful methods, surface wave tomography and shear-wave splitting observations cannot investigate the deep local anisotropy with good vertical and lateral resolution, resulting in poor constraints on plate deformation processes of the complex plate boundary beneath the southern California region. The first approach involves using the shear wave splitting phenomenon, observed for nearly vertically propagating waves (e.g., SKS phase) (Vinnik et al., 1984; Silver & Chan, 1988), to estimate the polarization of fast quasi-shear waves, which is assumed to be related to the principal horizontal stress/strain directions (Crampin & Lovell, 1991). This method can be conducted using a single three-component seismic station but lacks depth resolution (Savage, 1999). The second approach uses observations of surface waves from multiple directions on a seismic array of sufficient size to determine the directional anisotropy of Love or Rayleigh waves (Forsyth, 1975). This method offers better depth resolution through the frequency dependence of the surface wave phase velocity (Montagner & Nataf, 1986) but may have limitations in lateral resolution.

Therefore, we apply the proposed 6C anisotropy approach for the first time to estimate local anisotropy parameters in the upper mantle using surface wave observations. With its complex tectonic and geodynamic environment, southern California is ideal for applying this new approach. The dense broadband seismic network in southern California, operational for several decades, allows us to use a subset of stations as an array, use the array-derived rotation (ADR) technique (Spudich et al., 1995; Spudich & Fletcher, 2008) to estimate the rotation, and then apply the single-station technique to the resulting 6C data. We aim to investigate the agreement between the frequency-dependent anisotropy parameter and other geophysical or geodetic observations and how this approach provides new information about the layering and orientation variations of azimuthal anisotropy at depth.

Microseismic noise on Earth is a valuable resource for studying Earth's structure. Translational observations of this noise have been widely used to study the subsurface velocity structure and seismic anisotropy (Shapiro et al., 2005; Yao et al., 2010). However, the potential of rotational observations to provide additional constraints on the Earth's interior has been a scientific challenge. The interaction of ocean waves with the solid Earth produces two common types of microseismic noise (Longuet-Higgins, 1950; Iyer, 1958; Hasselmann, 1963; Obrebski et al., 2012; Stutzmann et al., 2012; Ardhuin et al., 2011, 2015, 2019; Gualtieri et al., 2020, 2021): primary (with 10-20 seconds) and secondary (with 3-10 seconds). It is generally believed that in very shallow waters, the direct interaction of ocean waves with the seafloor can explain the generation mechanism of primary microseismic Rayleigh waves and Love waves with a period of about 10-20 seconds (Gualtieri et al., 2020, 2021; Fukao et al., 2010; Saito, 2010). Meanwhile, the origin of secondary microseismic Rayleigh waves is due to the interaction of two opposing swells, which can generate secondary pressures that interact anywhere on the seafloor (Longuet-Higgins, 1950; Obrebski et al., 2012).

From a theoretical point of view, it is expected that Rayleigh waves should dominate secondary microseismic events due to the vertical pressure exerted by ocean waves on the

seafloor. However, this cannot explain the generation mechanism of secondary microseismic Love waves with horizontal polarization patterns. The current hypotheses for the mechanism of the secondary microseismic Love waves suggest that the presence of bathymetric inclines enables leading to the splitting of the vertical secondary-order pressure force in a component tangent to inclines, which can be responsible for the Love waves (Rind & Down, 1979; Gualtieri et al., 2020, 2021; Le Pape et al., 2021). In addition, the lateral heterogeneity within the Earth may also lead to the generation of Love waves due to scattering effects (Rind & Down, 1979; Gualtieri et al., 2020). Despite this, seismologists have debated the origin of secondary microseismic Love waves for decades. Accurately locating and tracking microseismic sources has been a challenge to understand better the generation mechanisms of these two different vibrations, especially Love waves.

To study the generation mechanism of Love waves, it is crucial to observe their seasonal variation. Previous studies have shown that the direction of the microseismic noise source can be estimated from 6C observations (Hadziioannou et al., 2012; Gualtieri et al., 2020). In addition, 6C ground motions can naturally separate microseismic Rayleigh waves into horizontal components and microseismic Love waves into vertical rotational components (Hadziioannou et al., 2012; Tang & Fang, 2021a), significantly improving Love wave source measurements. We use the emerging 6C observations to estimate the seasonal variation of the microseismic noise source. Since most places worldwide do not have portable rotational sensing systems to analyze long-term ambient noise observations, we use array-derived rotation (ADR), which uses wavefield gradient estimates from surface seismic arrays with appropriate frequency bands. The microseismic rotational motions generated by the small seismic array at the Piñon Flat Observatory in southern California can be used to study seismic anisotropy and allow us to investigate long-term changes in microseismic noise sources.

In addition, our recent theoretical paper (Tang & Fang, 2023) presents a new approach focusing on the amplitude of rotational microseismic noise data. This approach allows the measurement of local phase velocities from the amplitude ratios of the 6C cross-correlation functions, providing local sensitivity to monitor velocity changes in regional structures. To extend this theory to the rotational anisotropy, local seismic anisotropy is investigated from the azimuth-dependent 6C cross-correlation functions. We still use a small seismic array at the Piñon Flat Observatory in Southern California to retrieve rotational ground motions and investigate local seismic anisotropy for the first time. We highlight that ground deformations caused by atmospheric pressure are highly sensitive to the rotational motions generated by the seismic array, especially primary microseismic Love waves, which are essential for characterizing low-noise rotational motion models of the Earth (Brotzer et al., 2023). These studies promote the development of sensitive rotational sensors to expand the potential of 6C observations, allowing the inversion of anisotropy parameters from point measurements.

The thesis consists of four chapters exploring the proposed 6C surface wave anisotropy theory and its practical application in observation. These chapters discuss the use of long-period teleseismic surface waves to study the anisotropy of the upper mantle, the application of cross-correlation theory of ambient seismic noise sources to examine the

anisotropy of the upper crust, and the investigation of the mechanism of the microseismic noise source.

Chapter 2 contains the paper "Single-Point Dispersion Measurement of Surface Waves Combining Translation, Rotation and Strain in Weakly Anisotropic Media: Theory" published in Geophysical Journal International (Tang et al., 2023c) proposes a new theory for measuring the dispersion relation of surface waves in weakly anisotropic media using a single station, which consists of translational displacement and rotation or strain. The azimuth-dependent surface wave dispersion curve can be directly obtained by using the amplitude ratio of translational displacement to rotation or strain. The amplitude ratio gives the localized azimuth-dependent dispersion relations of the formation beneath a receiver without requiring knowledge of the source or structure along the path. The theory shows that the coupled quasi-Rayleigh (qR) wave and quasi-Love (qL) wave will result in elliptically polarized rotational motions in anisotropic media. We conduct numerical experiments, investigate the effects of noise and degree of anisotropy, and demonstrate the potential for field studies.

Chapter 3 contains the paper "Anisotropy and deformation processes in Southern California from rotational observations" published in Geophysical Research Letters (Tang et al., 2023a). Seismic anisotropy in the upper mantle reveals geodynamic processes and the tectonic evolution of the Earth. The two most powerful methods, surface wave tomography and shear-wave splitting observations cannot investigate the deep local anisotropy with good vertical and lateral resolution, resulting in poor constraints on plate deformation processes of the complex plate boundary beneath the Southern California region. Here, we show that the amplitude ratio of translational displacement and rotation makes it possible to retrieve the local anisotropy in the upper mantle. Azimuthal anisotropy in the asthenosphere is well-determined and resolved in lateral and vertical directions. The fast axis retrieved from amplitude observations indicates the local rapid changes in plate deformation and complex pattern of mantle flow, which is compatible with the distributions of horizontal mantle flow illuminated by geodetic measurements, providing new insights into the geodynamic processes of the Southern California region.

Chapter 4 contains the paper "Seismic anisotropy from 6C ground motions of ambient seismic noise" published in Journal of Geophysical Research: Solid Earth (Tang et al., 2024). We propose a new approach capable of measuring local seismic anisotropy from 6C (three-component translation and three-component rotation) amplitude observations of ambient seismic noise data. Our recent theory demonstrates that the amplitude ratio of 6C cross-correlation functions (CCFs) enables retrieving the local phase velocity. This differs from conventional velocity extraction methods based on the travel time. Its local sensitivity kernel beneath the 6C seismometer allows us to study anisotropy from azimuth-dependent CCFs, avoiding path effects. Such point measurements have great potential in planetary exploration, ocean bottom observations, or volcanology. We apply this approach to a small seismic array at Piñon Flat Observatory (PFO) in southern California, array-deriving retrieves rotational ground motions from microseismic noise data. The stress-induced anisotropy is well resolved and compatible with other tomography results, providing constraints on the origin of depth-dependent seismic anisotropy.

Chapter 5 contains the paper "Seasonality of microseismic sources in Southern California from 6C ground motions" which will be submitted to a journal soon. Ocean waves interact with the solid Earth, generating two dominant signals called microseisms, which carry information about energy exchange between different Earth systems. We show that 6C (three-component translation and three-component rotation) observations can resolve its seasonal azimuthal variations. We employ the rotational motions retrieved by a small seismic array at the Pinon Flat Observatory (PFO) in southern California to investigate the two dominant microseismic sources: primary and secondary microseisms. As expected, the primary microseismic Rayleigh waves show strong seasonal variations, whereas the secondary microseismic Rayleigh waves show slight seasonal changes. In contrast, we find that secondary microseismic Love waves exhibit stable seasonality. This discrepancy from the secondary microseismic Rayleigh waves provides us with new insights into the generation mechanism of Love waves. In addition, the results also show that effectively estimating the natural seasonal variation of microseismic sources can provide constraints for studying seismic anisotropy, and the rotational motion of primary microseisms retrieved by seismic arrays is more sensitive to ground deformation caused by air pressure.

Chapter 2

Single-Point Dispersion Measurement of Surface Waves Combining Translation, Rotation and Strain in Weakly Anisotropic Media: Theory

by Le Tang, Heiner Igel and Jean-Paul Montagner
Published in Geophysical Journal International (2023), 235(1), 24-47.
https://doi.org/10.1093/gji/ggad199

2.1 Summary

A new approach is proposed for measuring the dispersion relation of surface waves in weakly anisotropic media using a single station, which consists of translational displacement and rotation or strain. The azimuth-dependent surface wave dispersion curve can be directly obtained by using the amplitude ratio of translational displacement to rotation or strain. Using observations from earthquakes from a variety of azimuths allows us to characterize the anisotropy of subsurface media. The amplitude ratio gives the localized azimuth-dependent dispersion relations of the formation beneath a receiver without requiring knowledge of the source or structure along the path. The theory shows that in anisotropic media the coupled quasi-Rayleigh (qR) wave and quasi-Love (qL) wave will result in elliptically polarized rotational motions. In addition, rotational motion information allows the determination of backazimuth even in general anisotropic media. We carry out numerical experiments, investigate the effects of noise and degree of anisotropy, and demonstrate the potential for field studies.
Key words:
Rotational seismology; Seismic anisotropy; Theoretical seismology.

2.2 Introduction

The study of seismic anisotropy has turned into a field of its own, relating material properties, stress-aligned heterogeneities, or pore space, with dynamic phenomena such as mantle flow or fluid flow directions in crustal rocks (Anderson, 1965; Crampin, 1977; Forsyth, 1975; Anderson & Dziewonski, 1982; Montagner & Tanimoto, 1991; Nataf et al., 1984; Legendre et al., 2021). A complete understanding of seismic anisotropy aids in characterizing the subsurface structure (e.g., Gupta, 1973; Legendre et al., 2021) and earthquake disasters (Teanby et al., 2004). Previous studies on seismic anisotropy focus on translational displacement, including P wave azimuthal anisotropy (Hess, 1964; Francis, 1969), P wave polarization (Schulte-Pelkum et al., 2001; Al-Lazki et al., 2004; Mutlu & Karabulut, 2011), shear wave splitting (Crampin & Chastin, 2003; Vinnik et al., 1989; Silver, 1996), surface wave azimuthal anisotropy and polarization analyses (Forsyth, 1975; Hess, 1964; Tanimoto & Anderson, 1985; Montagner & Nataf, 1986; Maupin, 1989; Montagner & Tanimoto, 1991).

Azimuthal anisotropy based on surface wave dispersion can be studied by determining the dispersion curves of different azimuth angles using single station methods, interstation methods, or array-based methods. The single station method has been used principally to measure fundamental mode dispersion curves (Levshin et al., 1972; Forsyth, 1975; Ekström et al., 1997). Some of the more sophisticated approaches require knowledge of prior information of the source function or approximate earth structure (e.g., Brown et al., 2022) limiting the domain of application. The interstation or array-based method (Forsyth et al., 2005; Pedersen, 2006) makes use of phase differences between seismograms measured at different stations to estimate phase velocity. This has been successfully applied to seismic ambient noise (Yao et al., 2006, 2008; Stehly et al., 2009; Yao et al., 2010; Legendre et al., 2021) combined with cross-correlation analysis (Shapiro & Campillo, 2004; Shapiro et al., 2005). The dispersion measurement of the traditional single-station method or multi-station method is the average velocity between the source (earthquake source or ambient noise fictional source) and the station, even if the average interstation dispersion can be related to the local phase velocity via an integral over the interstation arc (Legendre et al., 2021). Heterogeneity will also greatly affect results using these methods because the initially extracted dispersion curve is the average dispersion information along the surface wave propagation path.

Single-point anisotropy analysis of the polarization motion of surface waves (Park & Yu, 1993; Tanimoto, 2004) seeks to retrieve azimuthal variations of amplitude or amplitude ratios and obtain constraints on the anisotropic structure directly under the receiver. However, the polarization anomaly of a given station depends not only on the structure below the station but also on the structure seen by the wave in a significant part of the propagation path, unless the structure is uniformly anisotropic over a wide range (Maupin, 2004). Because of the limitations (heterogeneity effect and complexity of polarization) of the above surface wave anisotropy analysis, this paper attempts to find a method, characterizing the azimuthal anisotropy of subsurface structure without the influence of heterogeneity along the path or source effects.

The rapid development in rotational sensor technology (Pancha et al., 2000; Schreiber et al., 2005; Bernauer et al., 2021; Zembaty et al., 2021; Igel et al., 2021) allows us to exploit the potential application of rotational motions. Under the assumption of an isotropic medium or transversely isotropic (VTI) medium with vertical symmetry axis, only an S-related wave (including conversions) can generate rotational motions (Tang & Fang, 2021a). This allows us to uniquely identify and separate the wavefield using polarization characteristics (Sollberger et al., 2018; Schmelzbach et al., 2018; Wassermann et al., 2022). Because the rotational component of an S-related wave is perpendicular to the wave propagation direction and should have the same phase as the corresponding translational displacement, the propagation azimuth of an earthquake can also be easily estimated using a single station (Igel et al., 2007; Wassermann et al., 2016). This even works for the direction of moving seismic sources (Yuan et al., 2021).
Fichtner & Igel (2009) gave the verification that the sensitivity kernels of the amplitude ratio (translational displacement and rotation) of surface waves or S waves attain large absolute values only in the vicinity of the receiver, but not the source, and such measurements may be used for local shear-wave speed tomography. The estimation of local phase velocity measurements from amplitude ratios has been verified with real observations and a variety of different rotation sensors (Igel et al., 2007; Wassermann et al., 2016; Keil et al., 2021; Fang & Tang, 2021). Tang & Fang (2023) gave theoretical formulas of cross-correlation between displacement and rotation, and theoretically verified that the local phase velocity can also be extracted from amplitude ratios derived from ambient seismic noise.
Recently, Noe et al. (2022) numerically exploited the characteristics of body waves in a general anisotropic medium, demonstrating the feasibility to invert local anisotropic elastic parameters from rotational motions and strain by estimating the body wave velocity from amplitude ratios. Consequently, we can expect to use the translational displacement and rotation or strain to retrieve locally anisotropic parameters of subsurface structure from surface waves. To demonstrate this novel processing approach is the key goal of this study. The paper is organized into two main sections. First, we establish the theoretical basis of the azimuth-dependent dispersion measurements from a single seismic station in weakly anisotropic media. Second, we numerically investigate the capability of extracting the azimuth-dependent dispersion curve from a single station and illustrate the effect of coupling terms. Furthermore, we compare our approach to the more classic analysis using phase effects.

2.3 Theory

In Cartesian Coordinates, the strain tensor and rotation can respectively be defined as (Aki & Richards, 2002):

$$\varepsilon_{ij} = \frac{1}{2}(u_{i,j} + u_{j,i}) \tag{2.1}$$

$$\Omega_i = \frac{1}{2}(u_{k,j} - u_{j,k}) \tag{2.2}$$

where $u_{i,j}$ represents the partial derivative of translational displacement of i component with respect to j component. i,j, and k vary among x, y, and z.
The relation between stress and strain can be given as:

$$\sigma_{ij} = C_{ijkl}\varepsilon_{kl} \tag{2.3}$$

where C_{ijkl} (i, j, k and l vary among x, y and z) is the fourth-order elastic tensor and σ_{ij} represents the stress tensor. Considering the free surface boundary condition, where we assume that the surface is horizontal, the traction is equal to zero which indicates $\sigma_{iz} = 0$. Therefore,

$$\sigma_{iz} = C_{izkl}\varepsilon_{kl} = 0 \tag{2.4}$$

Under the assumption that the media is only weakly anisotropic, the translational displacement of the anisotropic media can be written as a combination of Rayleigh and Love wave eigenfunctions in the reference isotropic media (Tanimoto, 2004), whose expressions are given below:

$$\mathbf{u} = a_L\mathbf{u}_L + a_R\mathbf{u}_R \tag{2.5}$$

where $\mathbf{u}_L$ and $\mathbf{u}_R$ are the Love and Rayleigh wave translational displacement of the reference isotropic medium, respectively, a_L and a_R are the coefficients to be determined from the stationarity of the Lagrangian. The dispersion relation and polarization of translational displacement in anisotropic media derived from the stationarity of the Lagrangian under the assumption of eq. 2.5 have been verified by comparison with other direct integral results (Tanimoto, 2004). Therefore, we will derive the polarization of rotation and strain under this assumption.
In isotropic media, $\mathbf{u_L}$ and $\mathbf{u_R}$ have the form:

$$\begin{cases} \mathbf{u}_L = [-sin\psi W(z), cos\psi W(z), 0]e^{i\kappa_{l0}(cos\psi x + sin\psi y) - i\omega t} \\ \mathbf{u}_R = [cos\psi V(z), sin\psi V(z), iU(z)]e^{i\kappa_{r0}(cos\psi x + sin\psi y) - i\omega t} \end{cases} \tag{2.6}$$

where $sin\psi^2 + cos\psi^2 = 1$, ψ is the azimuth of the direction of propagation measured from the X-axis. κ is the modulus of the horizontal wavenumber vector $\vec{\kappa}$. κ_{l0} and κ_{r0} represent the wavenumber of Love waves and Rayleigh waves in isotropic media respectively. $W(z)$ is the depth-dependent eigenfunction of the Love wave, $V(z)$ and $U(z)$ of the Rayleigh wave. ω is the circular frequency.
Substituting eqs 2.5 and 2.6 into the Lagrangian (Tanimoto, 2004), we obtain:

$$\mathcal{L}(u_i^*, u_i) = \omega^2 \int_{-\infty}^{0} \rho u_i^* u_i dz - \int_{-\infty}^{0} C_{ijkl}\varepsilon_{ij}^*\varepsilon_{kl} dz \tag{2.7}$$

By using the relations $\partial\mathcal{L}/\partial a_L = 0$, $\partial\mathcal{L}/\partial a_R = 0$ (Tanimoto, 2004), the coefficients in the limit of weak anisotropy under $|A - B| \geq E$ can be expressed as:
For quasi-Love waves:

$$(a_L, a_R) = (1, \frac{E}{A - B}) \tag{2.8}$$

For quasi-Rayleigh waves:

$$(a_L, a_R) = \left(-\frac{E}{A-B}, 1\right) \tag{2.9}$$

A and B are respectively the quasi-Love and Rayleigh waves' eigenfrequency square and E is the coupling term. The detailed expressions of E, A, and B can be found in the appendix of Tanimoto (2004). The translational displacement of quasi-Love wave can be expressed from eqs 2.5, 2.6, and 2.8 as:

$$\mathbf{u}_{qL} = [-sin\psi W(z) + cos\psi TV(z), cos\psi W(z) + sin\psi TV(z), iTU(z)]e^{i\kappa_l(cos\psi x + sin\psi y) - i\omega t} \tag{2.10}$$

The displacement of quasi-Rayleigh waves can be expressed from eqs 2.5, 2.6, and 2.9 as:

$$\mathbf{u}_{qR} = [sin\psi TW(z) + cos\psi V(z), -cos\psi TW(z) + sin\psi V(z), iU(z)]e^{i\kappa_r(cos\psi x + sin\psi y) - i\omega t} \tag{2.11}$$

where $T = \frac{E}{A-B}$. κ_l and κ_r represent the wavenumber of quasi-Love waves and quasi-Rayleigh waves in anisotropic media respectively.
Eqs 2.10 and 2.11 are obtained by Tanimoto (2004), indicating that because of the effect of coupling, the polarization of Love waves in anisotropic media becomes elliptical instead of the linear particle motion in isotropic media. The particle motion of Rayleigh waves has a transverse component, which is no longer confined in the radial-vertical plane. To derive the dispersion relations between displacement and rotation or strain, in the next section, we first derive the polarization of rotation and strain combined with the free surface boundary condition and then obtain the dispersion formulas.

2.3.1 Isotropic media

Polarization and dispersion relation of rotation and strain in isotropic media

Under the assumption of isotropic layered media, there is no azimuth-dependent velocity variation. Combining the boundary conditions eq. 2.4 and displacement function eq. 2.6, we can derive the following equations of eigenfunctions:

$$\begin{cases} V'(0) = \kappa_{r0} U(0) \\ (2\mu + \lambda)U'(0) + \lambda\kappa_{r0} V(0) = 0 \\ W'(0) = 0 \end{cases} \tag{2.12}$$

where μ and λ are the Lamé parameters for isotropic media. U', V' and W' represent the depth derivatives ($\partial_z|_{z=0}$) of the first-order eigenfunctions. Substituting eqs 2.12 and 2.6 into eqs 2.1 and 2.2, we obtain the polarization of rotation and strain at the surface ($z = 0$) in Cartesian coordinate (see Appendix C for detailed expressions). To better understand the polarization of rotation and strain, we project the polarization of eqs 2.6 and (C-1-C-4) onto the R-T coordinate system ($cos\psi = 1, sin\psi = 0$) of the propagation direction (R direction) shown in Fig. 2.1 with two identical vertical axes.

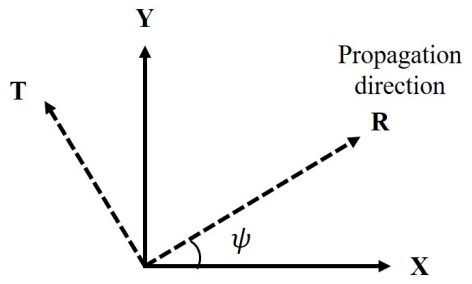

Figure 2.1: Diagram of Coordinate transformation.

In this paper, we analyze the polarization of rotational components $\Omega_i (i = r, t, z)$ and the radial strain component ε_{rr}, which correspond to rotational seismometers and strain sensors or DAS (Distributed Acoustic Sensing), respectively. After the coordinate projection (see section 5.4 of Chou & Pagano (1992) for the transformation relationship), the polarization of translational displacement, rotation, and strain at the surface (z=0) in the R-T coordinate system can be expressed as
For Love waves:

$$\begin{cases} u_r = 0 \\ u_t = W \\ u_z = 0 \end{cases} \tag{2.13}$$

$$\begin{cases} \Omega_r = 0 \\ \Omega_t = 0 \\ \Omega_z = i\kappa_{l0} W/2 \\ \varepsilon_{rr} = 0 \end{cases} \tag{2.14}$$

For Rayleigh waves:

$$\begin{cases} u_r = V \\ u_t = 0 \\ u_z = iU \end{cases} \tag{2.15}$$

$$\begin{cases} \Omega_r = 0 \\ \Omega_t = \kappa_{r0} U \\ \Omega_z = 0 \\ \varepsilon_{rr} = i\kappa_{r0} V \end{cases} \tag{2.16}$$

where we omit the exponential term $e^{i\kappa r - i\omega t}$. In the following derivation we also omit this term.
From a theoretical point of view, it is known that the translational displacement of the Rayleigh wave shows elliptical polarization in the R-Z plane and rotation shows linear polarization in the T direction. Both translational displacement and rotation of the Love wave show linear polarization in two orthogonal directions, respectively. Previous studies of surface waves with rotational components assume isotropic structure (Igel et al., 2007; Kurrle et al., 2010; Keil et al., 2021; Fang & Tang, 2021; Tang & Fang, 2021b, 2023), except

for the analysis of body waves by Noe et al. (2022). In the following, we will demonstrate that in anisotropic media rotational motions are no longer linearly polarized.
Comparing eqs 2.13-2.16, the surface wave dispersion relations can be directly obtained by combining the polarization of translational displacement and rotation or strain.
For Love waves:

$$c_L(\omega) = |\frac{\dot{u_t}}{2\Omega_z}| \tag{2.17}$$

For Rayleigh waves:

$$\begin{cases} c_R(\omega) = |\frac{\dot{u_r}}{\varepsilon_{rr}}| \\ c_R(\omega) = |\frac{\dot{u_z}}{\Omega_t}| \end{cases} \tag{2.18}$$

where $\dot{u}$ represents the first-order temporal derivative of displacement. Eqs 2.17 and 2.18 indicate that the dispersion phase velocity of Love and Rayleigh waves can directly be measured by the ratio of displacement to rotation or strain. This has been used widely in previous studies (Igel et al., 2007; Kurrle et al., 2010; Keil et al., 2021; Fang & Tang, 2021).

2.3.2 Anisotropic media

Because of the coupling between quasi-Rayleigh and quasi-Love waves in (weakly) anisotropic media (Tanimoto, 2004), the polarization of rotation of the two waves is no longer linear and shows elliptical form. An anisotropic medium is generally characterized by azimuth-dependent velocity variations. In the following derivation, we will separately consider three media: vertical transversely isotropic (VTI) media, general orthorhombic media (horizontal transversely isotropic (HTI) media is included), and general anisotropic media, whose expressions of the elastic tensor can be found in Appendix A. Among them, quasi-Love and quasi-Rayleigh waves are completely decoupled in VTI media and the phase velocity does not show azimuthal anisotropy. They are also decoupled for waves propagating along the symmetry axis and its perpendicular direction for HTI media.

Polarization and dispersion relation of rotation and strain in VTI media

The translational motion of VTI media has the same form as for isotropic media which can also be expressed by eq. 2.6. Therefore, the displacement, rotation, and strain also have the same polarization form, except for the vertical strain component $\varepsilon_{zz} = -\frac{C_{13}}{C_{33}} i\kappa V$ of quasi-Rayleigh wave, characterized by different elastic parameters. In addition, the dispersion formulas of VTI media generally also show the same form as isotropic media in eqs 2.17 and 2.18.

Polarization and dispersion relation of rotation and strain in general orthorhombic media

Orthorhombic medium with nine independent parameters is characterized by azimuth-dependent velocity variations derived using the free surface boundary conditions eq. 2.4

as:
For quasi-Love waves:

$$\begin{cases} sin\psi TV'(0) + cos\psi W'(0) = \kappa_l sin\psi TU(0) \\ -sin\psi W'(0) + cos\psi TV'(0) = cos\psi\kappa_l TU(0) \\ C_{33}TU'(0) + C_{13}\kappa_l cos\psi[-sin\psi W(0) + cos\psi TV(0)] + \\ C_{23}\kappa_l sin\psi[sin\psi TV(0) + cos\psi W(0)] = 0 \end{cases} \tag{2.19a}$$

For quasi-Rayleigh waves:

$$\begin{cases} sin\psi V'(0) - cos\psi TW'(0) = \kappa_r sin\psi U(0) \\ sin\psi TW'(0) + cos\psi V'(0) = cos\psi\kappa_r U(0) \\ C_{33}U'(0) + C_{13}\kappa_r cos\psi[sin\psi TW(0) + cos\psi V(0)] + \\ C_{23}\kappa_r sin\psi[sin\psi V(0) - cos\psi TW(0)] = 0 \end{cases} \tag{2.19b}$$

We substitute eqs 2.19a, 2.19b, 2.10 and 2.11 into eqs 2.1 and 2.2, and the polarization of rotation and strain in Cartesian coordinates can respectively be found in Appendix C. We project the polarization of eqs 2.10, 2.11 and C-5-C-8 onto the coordinate system (R-T) of propagation direction (R direction) shown in Fig. 2.1 and the polarization of translational displacement, rotation, and strain at the surface (z=0) can be expressed:
For quasi-Love waves:

$$\begin{cases} u_r = TV \\ u_t = W \\ u_z = iTU \end{cases} \tag{2.20}$$

$$\begin{cases} \Omega_r = 0 \\ \Omega_t = \kappa_l TU \\ \Omega_z = i\kappa_l W/2 \\ \varepsilon_{rr} = i\kappa_l TV \end{cases} \tag{2.21}$$

For quasi-Rayleigh waves:

$$\begin{cases} u_r = V \\ u_t = -TW \\ u_z = iU \end{cases} \tag{2.22}$$

$$\begin{cases} \Omega_r = 0 \\ \Omega_t = \kappa_r U \\ \Omega_z = -i\kappa_r TW/2 \\ \varepsilon_{rr} = i\kappa_r V \end{cases} \tag{2.23}$$

As illustrated in Fig. 2.3, the translational polarization of the quasi-Rayleigh wave deviates from the vertical-radial plane in general orthorhombic media while the quasi-Love wave transforms into elliptical polarization, in which the coupled quasi-Rayleigh wave will appear on the transverse component and the coupled quasi-Love wave will appear on the vertical component (Tanimoto, 2004). The rotational components of both waves exhibit

elliptical polarization. However, both are only polarized in the vertical-transverse plane which is perpendicular to the direction of propagation.

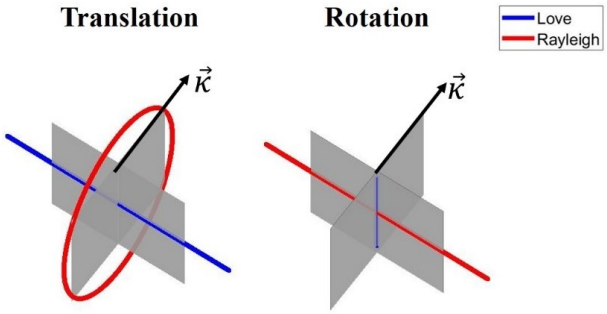

Figure 2.2: Diagram of polarization of translational displacement and rotation in isotropic media. The translational displacement of Rayleigh wave is elliptical polarization, while the love wave is linear polarization.The rotations of Love and Rayleigh waves are linearly polarized.

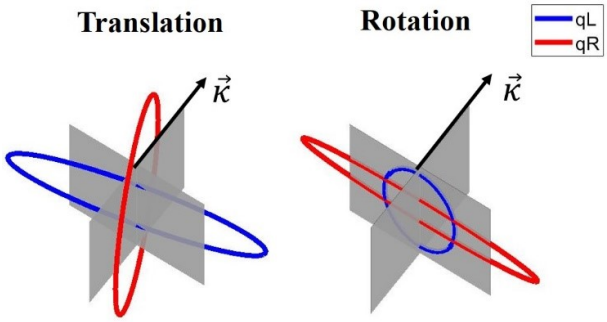

Figure 2.3: Diagram of polarization of translational displacement and rotation in general orthotropic media. The translational displacement and rotations of Love and Rayleigh waves are elliptically polarized.

Comparing eqs 2.20-2.23, the surface wave dispersion relations between translational displacement and rotation or strain can be easily obtained in general orthorhombic media: For quasi-Love waves:

$$c_L(\omega,\psi) = |\frac{\dot{u_t}}{2\Omega_z}| \tag{2.24a}$$

$$\begin{cases} c_L(\omega,\psi) = |\frac{\dot{u_r}}{\varepsilon_{rr}}| \\ c_L(\omega,\psi) = |\frac{\dot{u_z}}{\Omega_t}| \end{cases} \tag{2.24b}$$

For quasi-Rayleigh waves:

$$\begin{cases} c_R(\omega,\psi) = |\frac{\dot{u_r}}{\varepsilon_{rr}}| \\ c_R(\omega,\psi) = |\frac{\dot{u_z}}{\Omega_t}| \end{cases} \tag{2.25a}$$

$$c_R(\omega,\psi) = |\frac{i_t}{2\Omega_z}| \tag{2.25b}$$

Eqs 2.24a and 2.25a give the local azimuth-dependent dispersion relation of general orthorhombic media. An interesting point is that the additional dispersion of eqs 2.24b and 2.25b for general orthorhombic medium come from the coupled waves contributions but they are generally smaller. From a theoretical point of view, the derived dispersion formulas from the coupling term contribution are correct. However, from an observational point of view, measuring the dispersion curves using this approach is prone to errors due to the amplitude of the coupling term. When the coupling term is equal to zero, $T = 0$, the eqs 2.24a, 2.24b, 2.25a and 2.25b degenerate into the isotropic dispersion equations.

Polarization and dispersion relation of rotation and strain in general anisotropic media

Under the assumption of first-order perturbations, general anisotropic media with 21 independent variables degenerate into 13 (monoclinic media in Appendix A) (Smith & Dahlen, 1973; Montagner & Nataf, 1986). The free surface boundary conditions eq. 2.4 results in the following form:
For quasi-Love waves:

$$\begin{cases} C_{45}[cos\psi W'(0) + sin\psi TV'(0) - \kappa_l sin\psi TU(0)] + \\ C_{55}[cos\psi TV'(0) - sin\psi W'(0) - \kappa_l cos\psi TU(0)] = 0 \\ C_{44}[cos\psi W'(0) + sin\psi TV'(0) - \kappa_l sin\psi TU(0)] + \\ C_{45}[cos\psi TV'(0) - sin\psi W'(0) - \kappa_l cos\psi TU(0)] = 0 \\ C_{33}TU'(0) = C_{13}\kappa_l cos\psi[sin\psi W(0) - cos\psi TV(0)] - C_{23}\kappa_l sin\psi[cos\psi W(0) + sin\psi TV(0)] \\ -\frac{C_{36}}{2}[2sin\psi cos\psi\kappa_l TV(0) + cos\psi^2\kappa_l W(0) - sin\psi^2\kappa_l W(0)] \end{cases} \tag{2.26a}$$

For quasi-Rayleigh waves:

$$\begin{cases} C_{45}[-cos\psi TW'(0) + sin\psi V'(0) - \kappa_r sin\psi U(0)] + \\ C_{55}[cos\psi V'(0) + sin\psi TW'(0) - \kappa_r cos\psi U(0)] = 0 \\ C_{44}[-cos\psi TW'(0) + sin\psi V'(0) - \kappa_r sin\psi U(0)] + \\ C_{45}[cos\psi V'(0) + sin\psi TW'(0) - \kappa_r cos\psi U(0)] = 0 \\ C_{33}U'(0) = C_{23}\kappa_r sin\psi[cos\psi TW(0) - sin\psi V(0)] - C_{13}\kappa_r cos\psi[cos\psi V(0) + sin\psi TW(0)] \\ -\frac{C_{36}}{2}[2sin\psi cos\psi\kappa_r V(0) + (sin\psi^2 - cos\psi^2)\kappa_r TW(0)] \end{cases} \tag{2.26b}$$

Due to the complexity of the free surface boundary conditions which cannot simplify, the following derivation except for the third term of eqs 2.26a and 2.26b, we directly substitute eqs 2.10 and 2.11 into eqs 2.1 and 2.2. The polarization in Cartesian coordinates can be found in Appendix C. We project the polarization of eqs C-9-C-12 onto the coordinate system (R-T) of propagation direction (R direction) shown in Fig. 2.1, where translational components are the same as general orthotropic media, and the polarization of rotation

and strain at the surface (z=0) can be expressed as:
For quasi-Love waves:

$$\begin{cases} \Omega_r = 0 \\ \Omega_t = (TV' + \kappa_l TU)/2 \\ \Omega_z = i\kappa_l W/2 \\ \varepsilon_{rr} = i\kappa_l TV \end{cases} \tag{2.27}$$

For quasi-Rayleigh waves:

$$\begin{cases} \Omega_r = 0 \\ \Omega_t = (V' + \kappa_r U)/2 \\ \Omega_z = -i\kappa_r TW/2 \\ \varepsilon_{rr} = i\kappa_r V \end{cases} \tag{2.28}$$

The rotational polarization form in general anisotropic media is the same as that of general orthotropic media shown in Fig. 2.3. The polarization plane is perpendicular to the propagation direction, which means that even in a generally anisotropic medium, we can still use the polarization information of the rotation to obtain the back-azimuth. There is a difference with orthotropic media where it is easy to obtain the dispersion curves using u_z/Ω_t. The additional term V' in Ω_t will affect the ratio value, this point is discussed later. Comparing eqs 2.20, 2.22 with eqs 2.27 and 2.28, we can obtain the surface wave dispersion relation between displacement and rotation or strain:
For quasi-Love waves:

$$c_L(\omega, \psi) = |\frac{u_t}{2\Omega_z}| \tag{2.29a}$$

$$c_L(\omega, \psi) = |\frac{u_r}{\varepsilon_{rr}}| \tag{2.29b}$$

For quasi-Rayleigh waves:

$$c_R(\omega, \psi) = |\frac{u_r}{\varepsilon_{rr}}| \tag{2.30a}$$

$$c_R(\omega, \psi) = |\frac{u_t}{2\Omega_z}| \tag{2.30b}$$

The dispersion eqs 2.29b and 2.30b in general anisotropic media come from the coupled wavefield contributions that are generally smaller. Due to the complexity of the medium, the rotational polarization is difficult to simplify into a simple form in combination with the free surface boundary condition equation. Thus, there is no rotational formula that can be used to calculate the quasi-Rayleigh wave dispersion curve.

2.3.3 Effect of the coupling on the calculation of dispersion curves

The complete decoupling of Rayleigh and Love waves in isotropic and VTI media allows us to easily measure the local dispersion curves. On the contrary, the coupling effect in weakly

anisotropic media results in polarization planes of the displacement not perpendicular or parallel to the direction of propagation. Furthermore, the translational motion of the quasi-Rayleigh wave is no longer limited to the vertical-radial plane and the quasi-Love wave is no longer limited to the radial-transverse plane. There is no clear separation between the two waves unless the group velocity difference is large. Consequently, we have to assess the effect of the coupling when we apply our theory to real data. The effect of the coupling term T depends on the phase velocity difference of the two waves and the degree of anisotropy. This can be described by explicit formulas (Tanimoto, 2004):

$$T = \frac{E}{A - B} \tag{2.31}$$

The numerator and denominator of eq. 2.31 are simultaneously divided by the square of the wavenumber κ:

$$T = \frac{E/\kappa^2}{A/\kappa^2 - B/\kappa^2} = \frac{E/\kappa^2}{c_R^2 - c_L^2} \tag{2.32}$$

Eq. 2.32 indicates that if we fix the wavenumber, and the phase velocity difference of two waves is large enough, the T term tends to zero. Then the coupling term can be neglected. When we use eqs 2.24a and 2.25a to calculate the dispersion curves and we cannot identify the coupled quasi-Rayleigh and quasi-Love waves, using eqs 2.20-2.23, we obtain:

$$|\frac{\dot{u_z}}{\Omega_t}| = |\frac{[\omega TU]_{qL} + [\omega U]_{qR}}{[\kappa_l TU]_{qL} + [\kappa_r U]_{qR}}| \tag{2.33}$$

$$|\frac{\dot{u_t}}{2\Omega_z}| = |\frac{[\omega W]_{qL} + [-\omega TW]_{qR}}{[\kappa_l W]_{qL} + [-\kappa_r TW]_{qR}}| \tag{2.34}$$

As illustrated in eqs 2.33 and 2.34, the vertical translational displacement and transverse rotation contain not only the dominant quasi-Rayleigh wave energy, but also the quasi-Love wave signal generated by the coupling effect, and the transverse translation and vertical rotation contain not only the dominant quasi-Love wave energy but also the quasi-Rayleigh wave signal. As shown in eq. 2.32, the effect of the coupling term T will decrease and tends to zero when the velocity difference between the two modes increases. Consequently, eqs 2.33 and 2.34 degenerate to:

$$|\frac{\dot{u_z}}{\Omega_t}| \approx |\frac{[\omega U]_{qR}}{[\kappa_r U]_{qR}}| = c_R \tag{2.35}$$

$$|\frac{\dot{u_t}}{2\Omega_z}| \approx |\frac{[\omega W]_{qL}}{[\kappa_l W]_{qL}}| = c_L \tag{2.36}$$

It is generally appropriate to calculate the dispersion curves using eqs 2.35 and 2.36 for long-period teleseismic records because of the large velocity difference between fundamental quasi-Rayleigh wave mode and quasi-Love wave modes in that frequency range. The coupling strength is very weak regardless of whether the waveform can be distinguished in the time window. At this time, we do not need to separate the weakly coupled waveform.

In contrast, when the velocity difference between quasi-Rayleigh and quasi-Love waves is small, the coupling effect will become stronger. At this time, it is difficult to distinguish the two coupled waves which will limit the validation of the derived dispersion formulas. In the numerical section, we will compute the effect of the coupling term on measuring dispersion curves for data processing, and demonstrate that if the radiation energy of the focal mechanism is large enough, it will weaken the effects of the coupling on the amplitude ratio.

2.3.4 Analytical azimuth-dependent dispersion relation

To verify the derived dispersion relations above, we use the following analytical solution, which is proposed by Smith & Dahlen (1973). Mochizuki (1986) and Tanimoto (1986) also showed the equivalent formulas in a spherical earth for the first time. We use these to benchmark our numerical results in the next section.
By solving eq. 2.7 simultaneously, the azimuth-dependent dispersion relation is obtained (Tanimoto, 2004), having the same form as derived by Smith & Dahlen (1973); Montagner & Nataf (1986) after neglecting the coupling term E.

$$\delta c_L(\omega,\psi) = \frac{1}{2c_{L0}(\omega)}[L_1(\omega)+L_2(\omega)cos(2\psi)+L_3(\omega)sin(2\psi)+L_4(\omega)cos(4\psi)+L_5(\omega)sin(4\psi)] \tag{2.37a}$$

$$c_L(\omega,\psi) = \delta c_L(\omega,\psi) + c_{L0}(\omega) \tag{2.37b}$$

$$\delta c_R(\omega,\psi) = \frac{1}{2c_{R0}(\omega)}[R_1(\omega)+R_2(\omega)cos(2\psi)+R_3(\omega)sin(2\psi)+R_4(\omega)cos(4\psi)+R_5(\omega)sin(4\psi)] \tag{2.38a}$$

$$c_R(\omega,\psi) = \delta c_R(\omega,\psi) + c_{R0}(\omega) \tag{2.38b}$$

Here we define ψ as the azimuth of the wavenumber vector measured anti-clockwise from the X-axis. $\delta c_L(\omega,\psi)$ and $\delta c_R(\omega,\psi)$ are the first-order perturbations in phase velocity dispersion of azimuth- frequency-dependent quasi-Love and quasi-Rayleigh waves. $c_{L0}(\omega)$ and $c_{R0}(\omega)$ are phase velocity of Rayleigh and Love waves, respectively, for a reference isotropic medium. $c_L(\omega)$ and $c_R(\omega)$ represent the phase velocity of the quasi-Love wave and quasi-Rayleigh wave, respectively. $L_i(\omega)$ and $R_i(\omega)$ $(i = 1, 2, 3, 4, 5)$ are respectively depth integration functions that involve some elastic parameters and eigenfunctions, where we used a simple integration expression derived by Montagner & Nataf (1986), whose explicit expressions can be found in eqs (2), (4), and (5) of Montagner & Nataf (1986). We use the generalized reflection and transmission coefficients method (Chen, 1993) to calculate the eigenfunctions which have been used successfully in many cases (Chen, 1999; Tang & Fang, 2021a).
It is known that eqs 2.37a, 2.37b, 2.38a and 2.38b are derived based on the assumption of

Table 2.1: Layer properties of Model 1-reference isotropic media.

Layer	Depth(km)	V_p(km/s)	V_s(km/s)	ρ(kg/m^3)
1	0-30	6.6	3.8	3000
2	30-∞	8.0	4.6	3300

first-order perturbation which can be called the ordinary perturbation method without the contribution of mode coupling. An implicit assumption when utilizing this solution is that the difference between any two-mode phase velocity is larger than their respective perturbations (Maupin, 1989). This is generally valid for the fundamental mode. Consequently, we will focus on the analysis of the fundamental modes in the following numerical section.

2.4 Numerical analysis

In this section, we test the theory presented above for different anisotropic models. We analyze the effect of surface wave coupling on the estimation of dispersion curves. Synthetic data are generated by simulating the complete seismic wavefield applying a 3D standard staggered-grid finite difference method (Fang et al., 2014) which has been benchmarked with the generalized reflection and transmission coefficients method (Tang & Fang, 2021a). The free surface boundary condition is implemented, and the perfectly-match-layer (PML) boundary condition is applied to the sides and bottom boundary. A moment tensor source with a Ricker wavelet source time function is used to generate the synthetic waveforms. We output translational acceleration components $A_i(i = r, t, z)$ and rotational velocity components $\Omega_i(i = r, t, z)$. For the sake of simplicity, the synthetic data generated in a two-layer model will be used to validate the applicability of the derived theoretical formulas for all models.

2.4.1 Reference isotropic case

Model 1 is set up to be the reference isotropic medium, whose parameters are listed in Table 2.1. This is used to calculate the eigenfunction W, V, and U of eqs 2.6, 2.10, 2.11 and in the analytical solution of eqs 2.37a and 2.38a. We focus on long-period seismograms which means that we will neglect the higher-mode surface waves. However, the numerical modeling has to ensure that there is no (or negligible) higher-mode signal in the selected period range. Then the selected period range is also used for the following weakly anisotropic models.

Fig. 2.4 shows that for periods longer than 12s, there is only the fundamental (0th) mode solution for Model 1. Therefore, in the following numerical analysis, we focus on the period range of 12-80s. As illustrated in Fig. 2.5, all sources (black circles) are located at (0, 0, 1km), whose azimuth ψ is evenly distributed at 15 degrees ranging from 0 to 90 degrees. A station (black triangle) is located at the surface. The radial distance between all sources

and the station is equal to 2500km. The source-receiver geometry of Fig. 2.5 is used for the following models to verify the effectiveness of measuring the azimuth-dependent dispersion characteristics in anisotropic media.

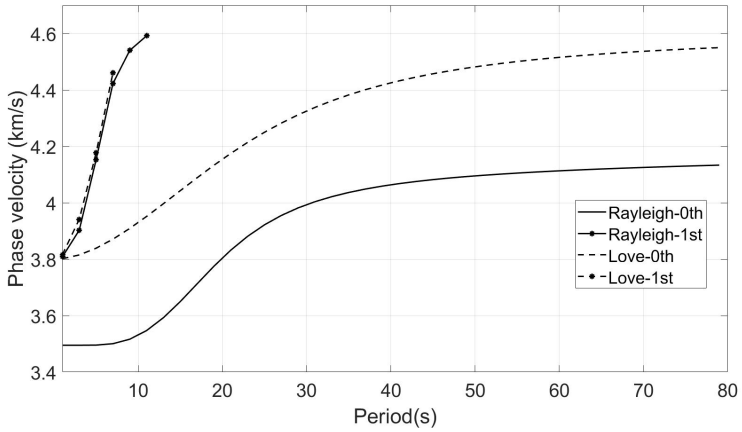

Figure 2.4: Theoretical dispersion curves of the reference isotropic Model 1. Rayleigh-0th: The fundamental mode of Rayleigh wave. Rayleigh-1st: The first higher mode of Rayleigh wave. Love-0th: The fundamental mode of Love wave. Love-1st: The first higher mode of Love wave.

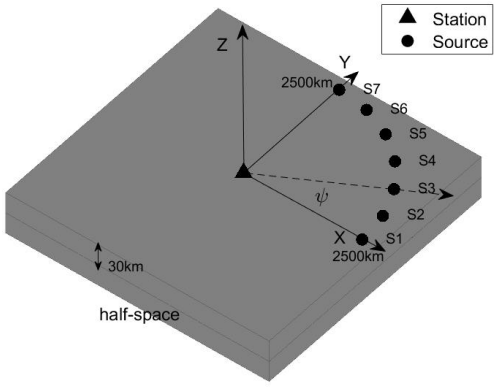

Figure 2.5: Distributions of Sources (black circles) and station (black triangle) of reference isotropic Model 1.

Two sets of synthetic data with different central frequencies, 0.015Hz (Period=66.7s) and 0.034Hz (Period=29.4s) are generated to ensure a 12s-80s wide-band seismogram. The

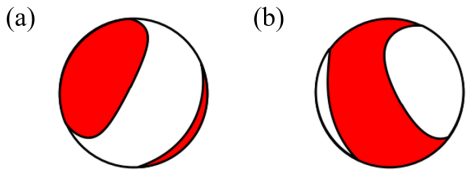

Figure 2.6: Beachball of focal mechanism in eqs 2.39 and 2.40.

magnitude of the moment tensor source is given as (Beachball is shown in Fig. 2.6a)

$$M = \begin{bmatrix} 0.1 & 0.2 & 0.35 \\ 0.2 & 0.25 & 0.5 \\ 0.35 & 0.5 & 0.15 \end{bmatrix} (N \cdot m) \tag{2.39}$$

In this model, the grid spacing is 5km and 3km for the two different central frequencies, respectively, and the time increment is 50ms for the 3D finite difference simulations. Figs 2.7 and 2.8 show the seismograms using the same focal mechanism with different central frequencies, where translational acceleration A_z and rotational velocity Ω_t are associated with Rayleigh waves and A_t and Ω_z are associated with Love waves. This indicates that the radiation energy of the Rayleigh wave is evenly distributed in seven directions and the radiation energy of directions of S4-S6 of the Love wave is much smaller. In combination with eqs 2.17, 2.18 and simulated seismograms of Figs 2.7 and 2.8, we can calculate the dispersion curves in different directions, where we introduce a robust weighted least-squares method based on time-frequency analysis to measure the ratio (see Appendix B). The weight function is equal to 1 for all data points in Model 1.
As illustrated in Fig. 2.9, the measured dispersion points of both the Rayleigh wave (red) and Love wave (blue) using the ratio dispersion of eqs 2.17 and 2.18 match with the analytical solution of the fundamental mode in any direction even with smaller radiation amplitude (see source 4-5 of Love waves). In addition, it also indicates that there are no higher mode seismograms in the selected periods. Consequently, we will select the period range of 12-80s to analyze the effect of coupling waves on dispersion measurements in various anisotropic models.

2.4.2 Contamination through coupled waves

Model 2 is set up to investigate the effect of coupling between quasi-Rayleigh and quasi-Love waves on calculating dispersion curves. For simplicity, we use a HTI medium with a symmetric axis parallel to the X-axis.

Model 2 consists of a half-space HTI medium based on Model 1, where the first layer is the same as that of the reference isotropic Model 1. Table 2.2 lists the medium properties of Model 2. We use five independent parameters as defined by Takeuchi & Saito (1972) to describe the HTI medium of Model 2, where α_V is the P-wave velocity along the symmetric axis, α_H is the P-wave velocity perpendicular to the symmetric axis, β_V is the

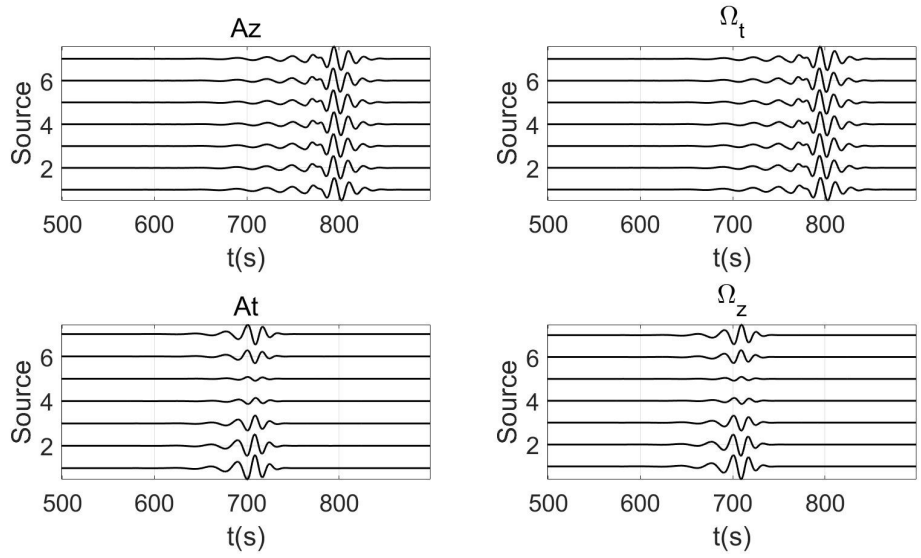

Figure 2.7: Normalized Seismograms of different azimuths with a 0.034Hz (Period=29.4s) central frequency of reference isotropic Model 1. A_z: translational acceleration in the vertical direction; A_t: translational acceleration in the transverse direction; Ω_t: rotational velocity in the transverse direction; Ω_z: rotational velocity in the vertical direction.

Table 2.2: Layer properties of Model 2-HTI media.

Layer	Depth(km)	ρ(kg/m^3)	α_V(km/s)	$\frac{\alpha_H-\alpha_V}{\alpha_H}$	β_V(km/s)	$\frac{\beta_H-\beta_V}{\beta_H}$	η
1	0-30	3000	6.6	0	3.8	0	1
2	30-∞(HTI)	3300	8.0	5%	4.6	5%	0.7721

S-wave velocity along the symmetric axis and β_H is the SH-wave velocity perpendicular to the symmetric axis. The anisotropic strength of HTI medium for both P-wave and S-wave is also 5%. The generated seismograms of Figs 2.10 and 2.11 of Model 2 are based on the same source-receiver geometry (Fig. 2.5), focal mechanism, and period ranges of Model 1. Combining dispersion eqs 2.24a and 2.25a of HTI media with seismograms in Figs 2.10 and 2.11, the dispersion curves are evaluated utilizing the least-square algorithm (Appendix B), where all data points are included indicating that the weight function is equal to 1. As illustrated in Fig. 2.12, the quasi-Rayleigh dispersion curves (red points) calculated by eq 2.25a generally match well with the theoretical dispersion curves (black points) showing azimuthal anisotropy. The phase velocity increases from 0 degrees to 90 degrees in the long period range corresponding to HTI medium. The results (blue points) of quasi-Love wave in the period range of 12s-30s also follow the trend of theoretical solution due to the reason that the short-period wavefield propagates in the isotropic medium of the first layer without the effect of anisotropy. On the contrary, the results of the quasi-Love wave deviate from the theoretical solution in the period range of 35s-80s, especially in the direction of

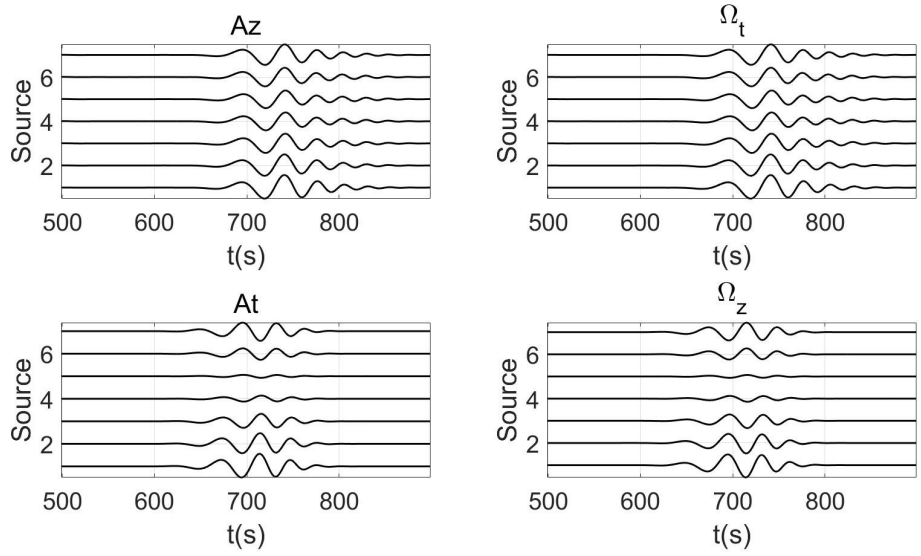

Figure 2.8: Normalized Seismograms of different azimuths with a 0.015Hz (Period=66.7s) central frequency of reference isotropic Model 1. A_z: translational acceleration in the vertical direction; A_t: translational acceleration in the transverse direction; Ω_t: rotational velocity in the transverse direction; Ω_z: rotational velocity in the vertical direction.

S4-S6, indicating that the quasi-Love wave is contaminated seriously by the coupled quasi-Rayleigh waves. As illustrated by the seismograms in Figs 2.10 and 2.11, the radiation amplitude of the quasi-Love wave in the direction of S4-S6 is much smaller, especially the S4 and S5 directions, so that the coupled quasi-Rayleigh waves cannot be ignored (see eq. 2.34). This has an important influence on the results. The radiation amplitude of quasi-Rayleigh waves in all directions is relatively large which can overshadow the influence of coupled quasi-Love waves.

To further illustrate the fact that the coupled wavefield is non-negligible when the radiation amplitude is very weak, we only change the focal mechanism, leaving all other simulation conditions unchanged, using the moment tensor source can be expressed as (Beachball is shown in Fig. 2.6b)

$$M = \begin{bmatrix} 0.1 & 0.2 & -0.35 \\ 0.2 & -0.25 & 0.5 \\ -0.35 & 0.5 & 0.15 \end{bmatrix} (N \cdot m) \tag{2.40}$$

As shown in Figs. 2.13 and 2.14, the radiation energy of the quasi-Love and quasi-Rayleigh waves have strong amplitudes in all directions. We use the same dispersion equation as in Fig. 2.12 to calculate the dispersion curve, and the results are shown in Fig. 2.15. It can be seen that the dispersion curve of the quasi-Love wave has been improved compared with the results in Fig. 2.12. This is consistent with the theoretical dispersion trend, but there

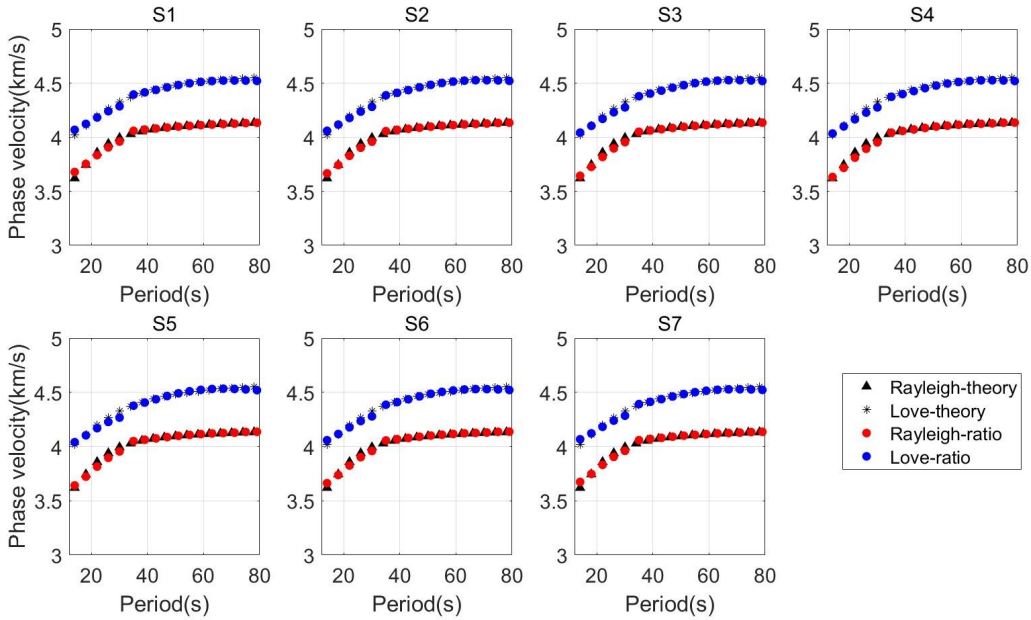

Figure 2.9: Comparisons of dispersion curves of different azimuths calculated using translation-rotation dispersion eqs 2.17 and 2.18 with seismograms in Figs 2.7 and 2.8, and analytical solution of the fundamental mode of reference isotropic Model 1. There is no correlation between the calculated results and the azimuth-dependent radiation pattern.

are still some deviations affected by the coupling. We further note that the deviation of the quasi-Love dispersion curve in Fig. 2.12 is mainly because the weak radiation amplitude will further amplify the coupling.

2.4.3 Azimuth-dependent coupling effects

As the anisotropy of the medium increases, the influence of the coupled wavefield on the amplitude will be larger. However, it can be seen from Figs 2.13 and 2.14 that even though the radiation amplitude of S4-S6 of the quasi-Love wave is relatively large, the calculated dispersion curve shown in Fig. 2.15 still has a small deviation in certain azimuths. The difference in the strength of the azimuthal anisotropy of the two wave types leads to the coupling being a function of azimuth. Fig. 2.16 shows the T (coupling term) value related to the coupled wavefield calculated theoretically for wavenumber $\kappa = 5 * 10^{-5}$ (the expression of T can be found in Appendix of Tanimoto (2004)) in Model 2 which shows the correlation with angle. With this wavenumber, the coupling of S4-S5 is stronger, and the effect on the ratio value is greater. Fig. 2.17 shows the dispersion curve calculated under different degrees of anisotropy while other model conditions are kept constant. We conclude that the influence of the coupled wavefield in the direction of 30 degrees -75 degrees (S3-S6) is

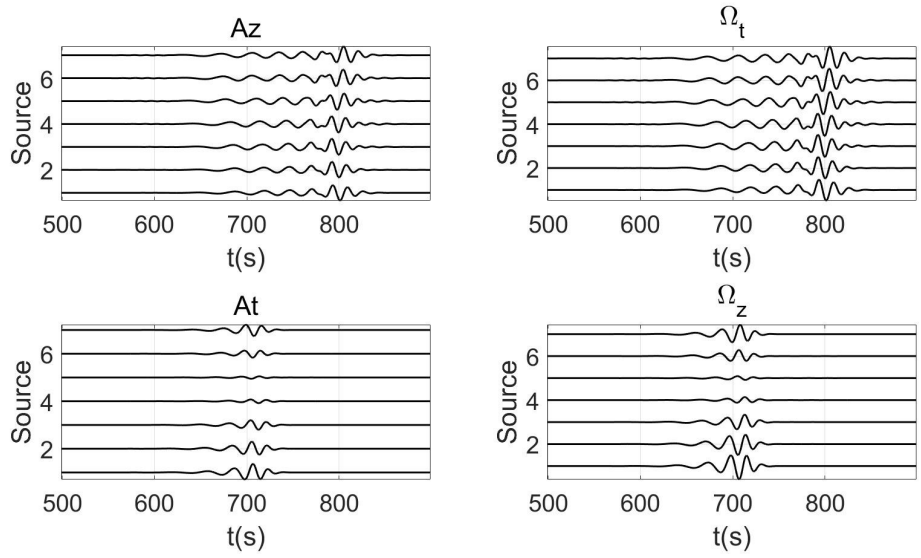

Figure 2.10: Normalized Seismograms of different azimuths with a 0.034Hz (Period=29.4s) central frequency of HTI Model 2 using the focal mechanism of eq. 2.39. A_z: translational acceleration in the vertical direction; A_t: translational acceleration in the transverse direction; Ω_t: rotational velocity in the transverse direction; Ω_z: rotational velocity in the vertical direction.

more stronger.

2.4.4 Seismogram stacking to stabilize solution

In order to weaken the effect of coupled wavefield on the results in some directions when the station is in the radiation node of the source, associated with a small amplitude, and to obtain a stable and reliable dispersion curve, we consider fitting data with multiple source seismograms in the same direction to obtain a reliable phase velocity. This is also in line with the consideration of actual data processing.
The media parameters and geometry of Model 3 are the same with that of model 2, except that 23 seismograms are generated in each direction with 23 different sources to estimate the dispersion value. The number of events is selected randomly, even one event with good radiation amplitude can lead to satisfactory results (see Fig. 2.15). In Model 3, the depth of sources in each direction is randomly distributed in the range of 5-15km, the center period of the wavelet is randomly distributed in the 30s-80s, and each magnitude of the focal mechanism is randomly selected from -1 to 1. Unlike in Models 1 and 2, we also calculate the radial strain seismogram ε_{rr} and radial translation seismogram A_r, which are associated with the quasi-Rayleigh wave, to illustrate the applicability of the translation-strain dispersion equation in eq 2.25a.
The least-square method of time-frequency analysis in Appendix B is also performed to

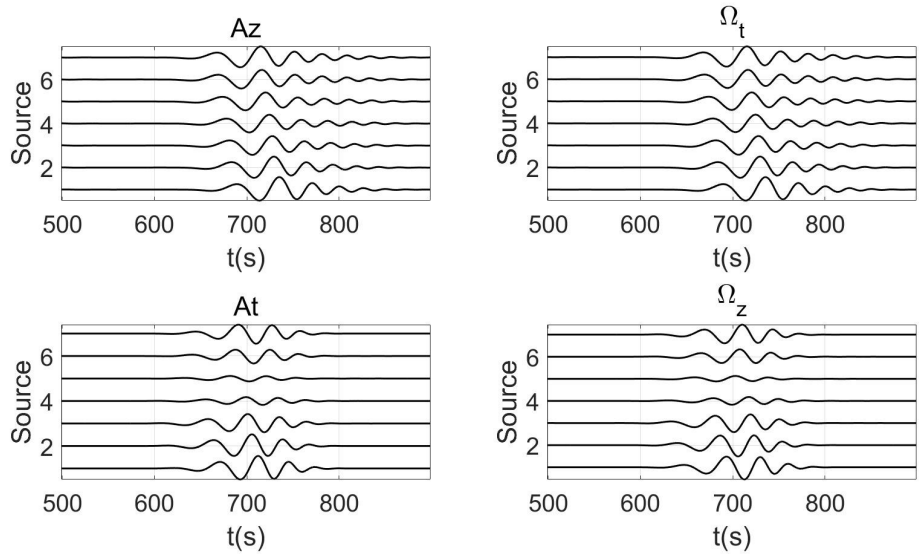

Figure 2.11: Normalized Seismograms of different azimuths with a 0.015Hz (Period=66.7s) central frequency of HTI Model 2 using the focal mechanism of eq. 2.39. A_z: translational acceleration in the vertical direction; A_t: translational acceleration in the transverse direction; Ω_t: rotational velocity in the transverse direction; Ω_z: rotational velocity in the vertical direction.

estimate the dispersion value. To reduce the influence of the coupled wavefield, the data with small radiation amplitude should be removed, which is demonstrated in the analysis of Model 2. A simple criterion is defined that the data points that are less than 10% of the maximum amplitude in each periodic signal will be removed, and only more than 10% of the energy is retained. This criterion is not fixed and can be adjusted according to the strength of actual anisotropy and noise level. Consequently, the weight function in Appendix B, which can also be called the filter function, can be expressed as:

$$wf(\omega, t_i) = \begin{cases} 0; |\frac{A(\omega,t_i)}{max[A(\omega,t_i)]}| < 10\% \\ 1; otherwise \end{cases} \tag{2.41}$$

Fig. 2.18 shows the time-period spectra of the first five seismograms (S1 direction) and the time-period spectra filtered by the weight eq. 2.41. It can be seen that after the processing of the weight function, the energy below 10% in each period is directly removed. And the time-period spectra of seismograms associated with other directions (sources) can also be obtained in the same way, although we don't show these spectra. This filtering is also suitable for the suppression of random noise. We will discuss this effect of random noise in the next section. Fig. 2.19 shows the calculated dispersion results using the filtered spectra in Figs. 2.18 combined with the dispersion eqs 2.24a and 2.25a, indicating that the results are consistent with the theoretical solution, whether it is a quasi-Rayleigh wave (red points) or a quasi-Love wave (blue points). At the same time, the results

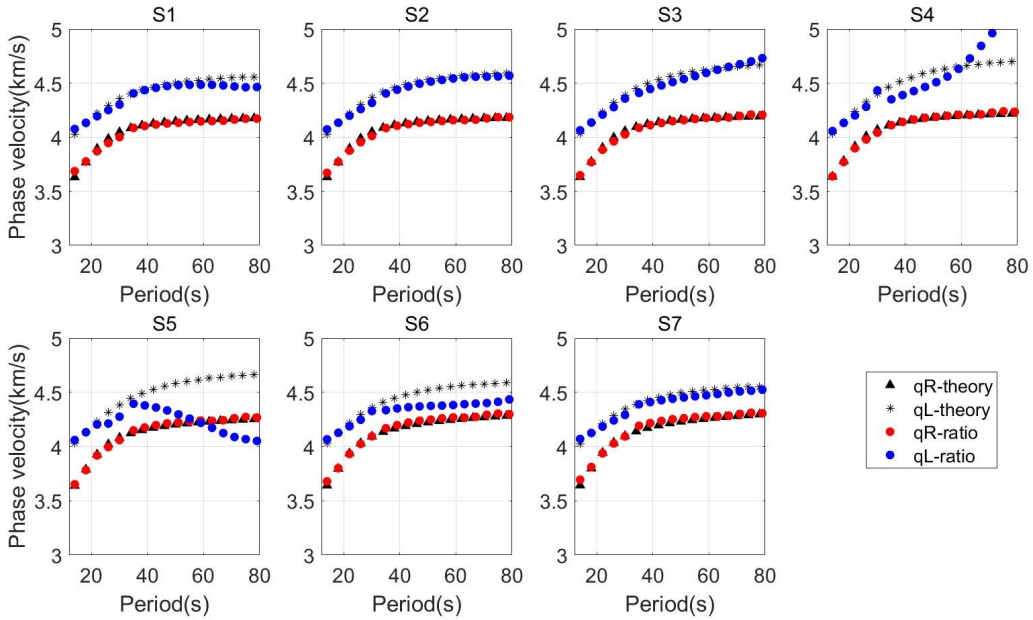

Figure 2.12: Comparisons of dispersion curves calculated using translation-rotation dispersion eqs 2.24a and 2.25a with seismograms in Figs 2.10 and 2.11, and analytical solution of the fundamental mode of HTI Model 2.

(green points) in Fig. 2.19 obtained by the translation-strain dispersion eq 2.25a also match well the theoretical values. It demonstrates that by using multiple seismograms, the unfavorable influence of the coupled wavefield can be eliminated, resulting in a stable and reliable dispersion curve. These simulation results from Model 1-3 demonstrate the correctness and applicability of the derived dispersion formulas which also means that the ratio of translational displacement to rotation or strain can identify the azimuthal anisotropy from a single station 6C (three displacement components and three rotation components) measurement.

2.4.5 The effect of random noise

From the perspective of seismological observations, the influence of noise or the uncertainties of amplitude measurements cannot be ignored. In particular, this paper uses frequency-dependent amplitude information to obtain the dispersion curves, and small amplitudes perturbations may have a strong impact on the results (Kurrle et al., 2010). Therefore, the least-square solution based on linear regression in Appendix B to fit the data helps to get a stable solution. The multiple seismograms of quasi-Rayleigh waves in the direction of azimuth $\psi = 0$ (S1) in Model 3 are used as input data for our noise analysis. Fig. 2.20 shows the first five seismograms (A_z) of Model 3 perturbed with random Gaussian noise with varying signal-to-noise ratio (SNR). It can be seen that when the SNR is equal to

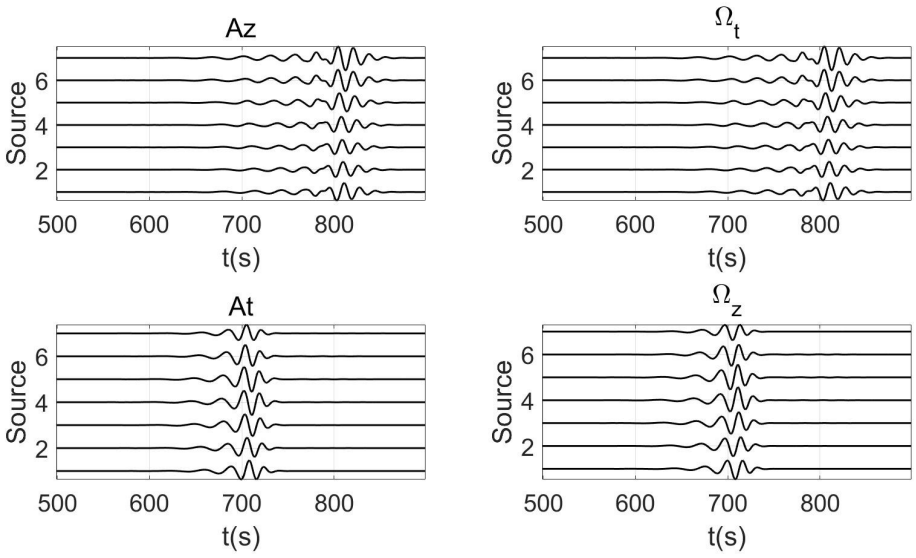

Figure 2.13: Normalized Seismograms of different azimuths with a 0.034Hz (Period=29.4s) central frequency of HTI Model 2 using the focal mechanism of eq. 2.40. A_z: translational acceleration in the vertical direction; A_t: translational acceleration in the transverse direction; Ω_t: rotational velocity in the transverse direction; Ω_z: rotational velocity in the vertical direction.

2, the noise covers the whole time window, and the amplitude of each waveform will be greatly changed.

We add Gaussian random noise with different signal-to-noise ratios to A_z and Ω_t at the same time. To simulate the influence of noise when processing multiple seismograms for one azimuth , each signal-to-noise ratio is generated 100 times and we calculate the kernel density function (Botev et al., 2010) of the phase velocity distribution, which represents its probability density distribution. When calculating the phase velocity using the approach described in Appendix B, we still use the weight function in eq. 2.41 to exclude amplitudes less than 10% in each period. Fig. 2.21 shows the kernel density function under different signal-to-noise ratios, and the black solid line is its theoretical dispersion curve. When the SNR is equal to 2, it can be seen that most of the energy is confined to the range within the 1% error bar, especially between 40-60s, benefitting from its large amplitude energy. For this period range 70-80s with small amplitude energy, its density function energy distribution is more dispersed than that of other periods. With an improvement of the signal-to-noise ratio, the energy of its kernel density function becomes closer to the theoretical dispersion curve. When the SNR is greater than 10, about 90% of the energy is distributed between a 1% error bar, showing that the dispersion curve obtained from this signal-to-noise ratio lets us resolve anisotropy of 3%-4% in the medium.

Consequently, for real data processing, the seismic data with a high signal-to-noise ratio and large radiation amplitude should be selected as much as possible to derive the dis-

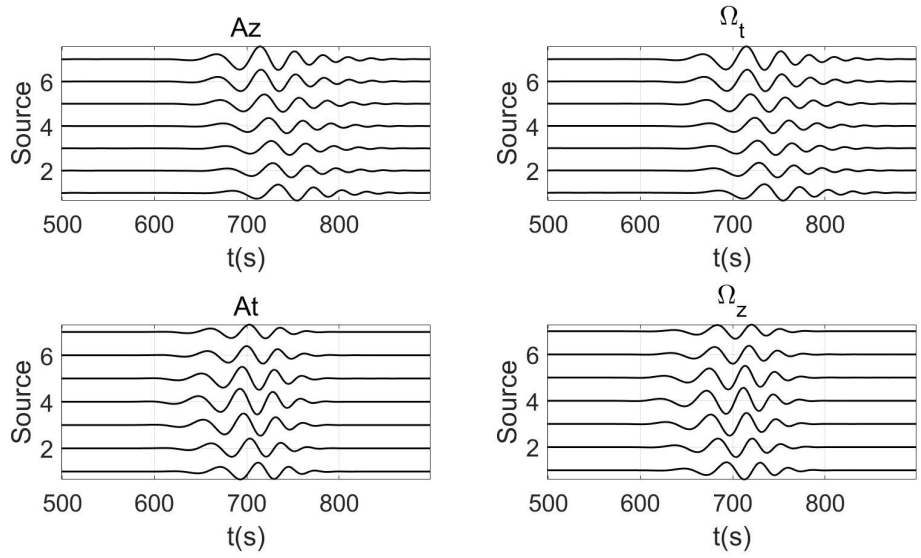

Figure 2.14: Normalized Seismograms of different azimuths with a 0.015Hz (Period=66.7s) central frequency of HTI Model 2 using the focal mechanism of eq. 2.40. A_z: translational acceleration in the vertical direction; A_t: translational acceleration in the transverse direction; Ω_t: rotational velocity in the transverse direction; Ω_z: rotational velocity in the vertical direction.

persion value, and the solution obtained by using the linear regression method is more reliable.

2.4.6 Estimating local dispersion characteristics

The commonly used method to study anisotropy based on phase difference measurement dispersion is to extract the average velocity between the source and the station (earthquake data), or the average velocity between stations (seismic ambient noise data). Therefore, if the measured dispersion curve shows angular anisotropy, it is difficult to judge whether it is caused by heterogeneity or anisotropy.
Model 4 is used to demonstrate the advantage of the ratio method on lateral resolution compared with the traditional phase difference method in analyzing azimuthal anisotropy. As shown in Fig. 2.22, the medium in the outer circle where the source is located in an isotropic medium, with parameters shown in Table 2.1. The inner cylinder with a radius of 500km below the station is an HTI medium with 3% anisotropy of the first layer of body waves, and the second layer is also a half-space HTI medium model with 4% anisotropy whose parameters are shown in Table 2.3. The seismograms for Model 4, which are associated with quasi-Rayleigh waves, are generated using the moment tensor source of eq. 2.40 whose central frequencies are 0.034Hz (period=29.4s) and 0.015Hz (period=66.7s), respectively. We still use the least-square method in Appendix B to calculate the disper-

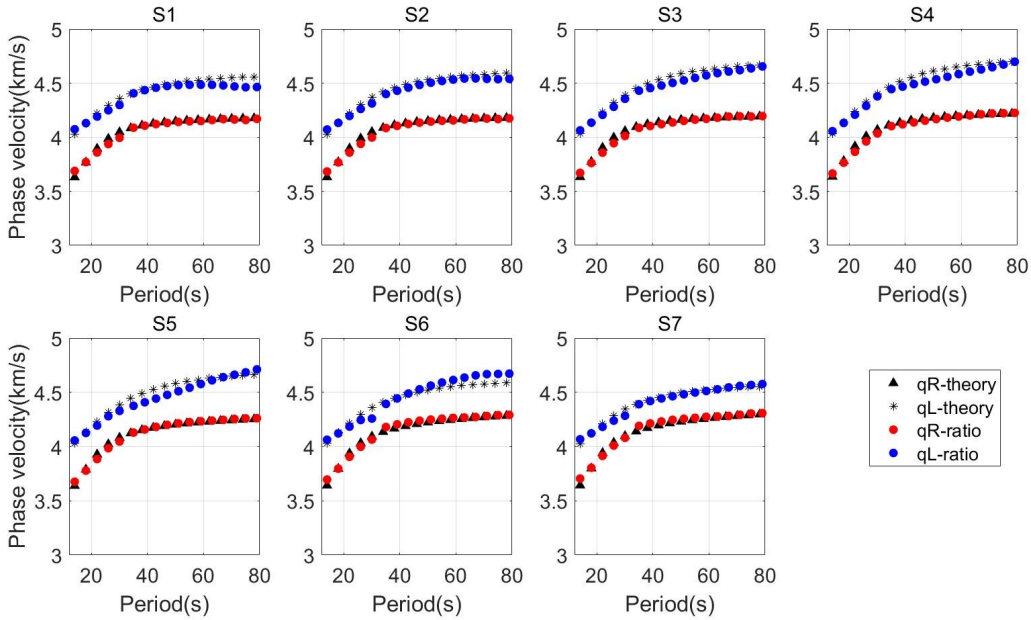

Figure 2.15: Comparisons of dispersion curves calculated using translation-rotation dispersion eqs 2.24a and 2.25a with seismograms in Figs 2.13 and 2.14, and analytical solution of the fundamental mode of HTI Model 2.

Table 2.3: Layer properties of the inner cylinder of Model 4.

Layer	Depth(km)	ρ(kg/m^3)	α_V(km/s)	$\frac{\alpha_H-\alpha_V}{\alpha_H}$	β_V(km/s)	$\frac{\beta_H-\beta_V}{\beta_H}$	η
1	0-30(HTI)	3000	6.6	3%	3.8	3%	0.8489
2	30-∞ (HTI)	3300	8.0	4%	4.6	4%	0.8090

sion points, where the weight function is equal to 1 for all data points. As illustrated in Fig. 2.23, the estimated dispersion is consistent with the theoretical dispersion curve of the inner cylindrical medium, reflecting the surface wave dispersion characteristics of the medium directly below the station. The derived ratio dispersion equation gives the localized azimuthal-dependent dispersion relations of the formation right beneath a receiver. This suggests that the smaller the wavelength, the smaller the influence of heterogeneity. Therefore, we expect that the ratio dispersion method will provide a higher lateral resolution imaging result on azimuthal anisotropy analysis, where the lateral resolution can be smaller than one wavelength (Tang & Fang, 2023).

2.4.7 Estimation of the azimuth using horizontal rotation

Accurate calculation of the azimuth of the wavefield incident on the station is crucial in the study of azimuthal anisotropy. It is the most basic parameter in the subsequent

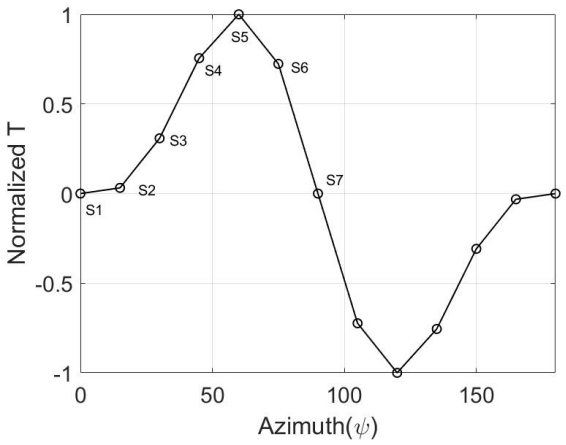

Figure 2.16: Azimuth-dependent Coupling term T value with wavenumber $\kappa = 5 * 10^{-5}$ in HTI Model 2. The coupling strength is the largest at the azimuths of S4 and S5, and is decoupled in the directions of S1 and S7.

correct inversion of the anisotropy and the evaluation of the azimuth of mantle flow or fracture orientation. The error of the angle will directly lead to errors of the anisotropy parameters. As illustrated in Fig. 2.2 and Fig. 2.3, the polarization characteristics of the rotation allow us to use the rotation component to calculate the incident azimuth of the phase velocity without distinguishing the properties of the medium and considering the effect of the coupled wavefield. The expression for calculating the azimuth can be given as

$$tan(\psi) = -\frac{\Omega_x}{\Omega_y} \tag{2.42}$$

The rotational seismograms of Model 2 and 3 with different focal mechanisms are used to verify the feasibility of using only the rotational component in eq. 2.42. Fig. 2.24 shows that the azimuth calculated from the rotational components is consistent with the theoretical azimuth and is not affected by the coupled wavefield despite the weak radiation amplitude S4-S6 in Figs 2.9-2.10 and contamination by coupling. The results, which are calculated with multiple seismograms in Model 3, are in good agreement with the theoretical values, indicating the applicability of eq. 2.42.

2.4.8 Anisotropy study based on the rotation angle

The polarization characteristics of rotations in Fig. 2.3 show that there is an additional angle between the propagation direction of the quasi-Rayleigh wave and the horizontal translation polarization direction in anisotropic media (see Fig. 2.25), which is called the rotation angle here. Similarly, there is also an additional angle between the quasi- Love wave and T-axis. This rotation angle is also a function of the propagation direction, so it can also be used to study azimuthal anisotropy. Taking the quasi-Rayleigh wave as an

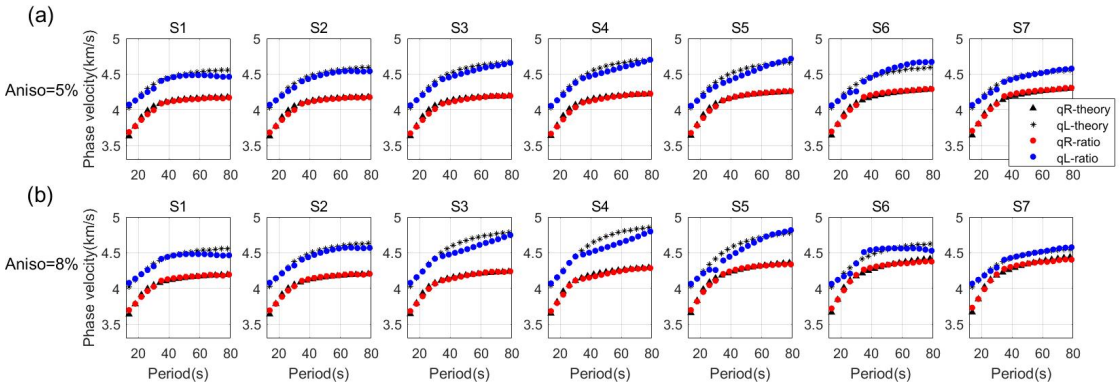

Figure 2.17: Comparisons of dispersion curves calculated using different anisotropic parameters and analytical solutions of the fundamental mode of HTI Model 2.

example, it can be seen from eq. 2.22 that the formula for calculating the rotation angle of the quasi-Rayleigh wave is

$$tan(\psi_0) = \frac{u_t}{u_r} = -\frac{W}{V}T \tag{2.43}$$

where the calculation of u_t and u_r from u_x and u_y requires the azimuth which can be calculated using rotation components in eq 2.42. The tangent function of this angle is represented by the coupling term T, which is an azimuth-dependent function. Its calculation is similar to eq. (20) in Tanimoto (2004) who used the ratio of the vertical translation component of the coupled quasi-Love wave to the horizontal translation component of the quasi-Love wave to analyze anisotropy, except that the amplitude is different.
Eqs 2.42 and 2.43 provide an alternative method for studying anisotropy. The advantage is that the azimuth estimation based on the rotation component will not be affected by the coupled wavefield, while the variables estimated based on the translation component will be affected by the coupled wavefield.

2.5 Discussion

We derived concise polarization form of rotation and strain based on the first-order perturbation. This form allows us to clearly describe the particle motion and the dominant surface waves can be verified by comparing with the numerical results. However, it is very hard to verify the dispersion relation (eqs 2.24b and 2.25b) of the coupled waves whose amplitude is generally pretty small in a weakly anisotropic medium.

This first-order perturbation theory shows that the rotational vector is orthogonal to the wavenumber vector, so the radial rotational component Ω_r is always equal to zero. From the observational point of view, the recorded seismogram will contain scattering waves

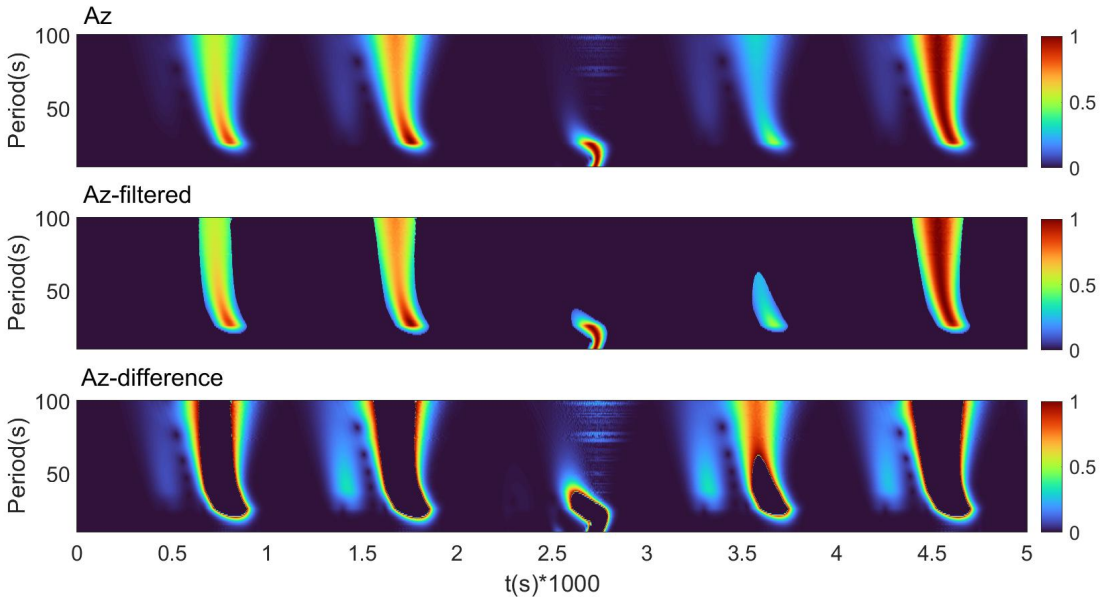

Figure 2.18: Period-normalized time-period spectra of the first five seismograms (S1 direction). From top to bottom: time-period spectra of A_z; filtered time-period spectra of A_z using weight function of eq. 2.41; removed time-period spectra of A_z.

from all directions due to the heterogeneity in the Earth, especially in the short period range. Therefore, the signal in the radial rotational component of an earthquake comes from the scattering waves rather than from the effects of anisotropy. As the frequency decreases, the earth structure generally will become more homogeneous, the amplitude of the radial rotational component will tend to be zero. This amplitude-dependent dispersion measurement approach requires very high accuracy for amplitude measurements. Even a very small amplitude perturbation can results in larger deviation (Kurrle et al., 2010). Consequently, it is very necessary to use multiple seismogram to obtain a reliable velocity. For a general anisotropic medium, as illustrated by eqs 2.30a and 2.30b, there is no available rotational component that can be used to calculate the Rayleigh wave velocity because the retrieval of phase velocity from eq. 2.30b which is from coupled waves is extremely difficult from real data. Considering the fact that the earth structure is a general anisotropic medium, and that the amplitude recorded by a rotational seismometer is more accurate than those of DAS at a single point observation, and the amplitude of fundamental Rayleigh waves is less affected by coupled waves than Love waves. So, is it possible to combine the rotational component to calculate the velocity of quasi-Rayleigh wave for a general anisotropic medium? Let us consider the assumption that κ_{r0} is close to κ_r, it means that the degree of anisotropy is very weak. Then, $V' \approx \kappa_r U$ in eq. 2.28 because in isotropic media, $V' = \kappa_{r0} U$ (see eq. 2.12). Combining eqs 2.28 and 2.22, we can also obtain the same dispersion relation in eq 2.25a for a general anisotropic medium. But there will be some

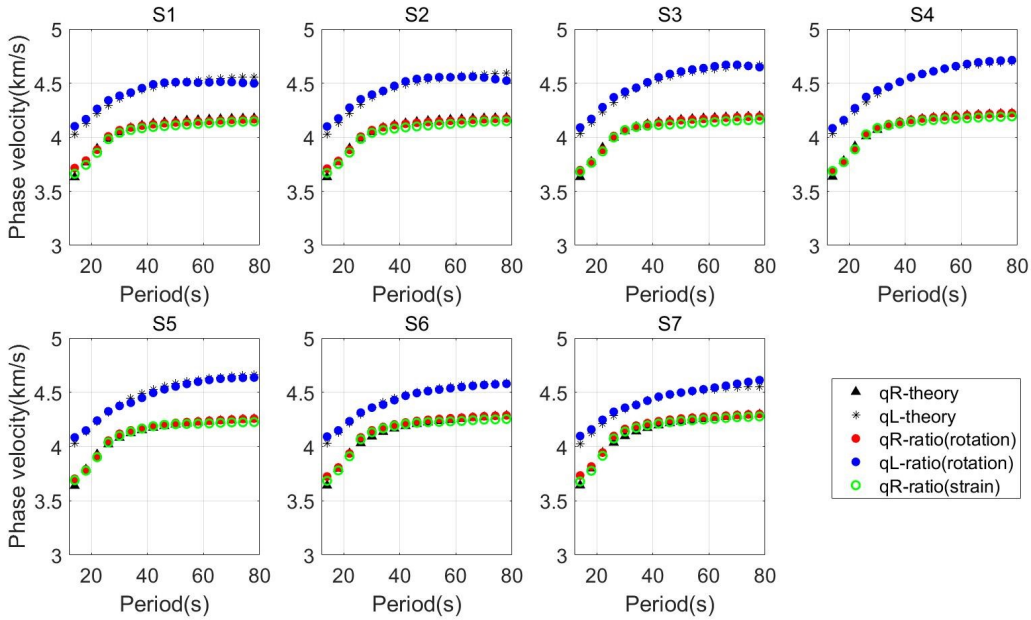

Figure 2.19: Comparisons of dispersion curves calculated using translation-rotation and translation-strain dispersion eqs 2.24a and 2.25a and analytical solution of the fundamental mode of Model 3.

errors when using the rotational waveform directly measured by the sensor. An alternative method is to use the ADR (Array Derived Rotation) (Spudich et al., 1995; Spudich & Fletcher, 2008) approach to retrieve the rotational waveform. However, it requires that the stations should be distributed as uniformly as possible in different azimuths and its frequency range is also limited by the aperture of a seismic array. It does not need to calculate the vertical partial derivative ∂_z, which means the V' in eq. 2.28 is equal to zero. Then we can also obtain the same dispersion eqs 2.25a for accurately calculating the velocity of quasi-Rayleigh wave by combining eqs 2.28 and 2.22. This method has been verified in our recent real data case (Tang et al., 2023b).

In this paper, we only study the fundamental mode due to the following two reasons: (1) The perturbation theory used to derive the dispersion formulas is valid only for the fundamental mode at short periods, and for fundamental modes and lowest overtones at longer periods (Maupin, 1989). The Rayleigh wave fundamental mode has a dispersion curve isolated enough from those of the other modes not to suffer from strong coupling with neighboring modes, while the Love wave fundamental mode will be affected by fundamental and higher modes of the Rayleigh wave, and the higher modes of Rayleigh wave and Love wave will suffer from coupling with neighboring modes seriously; (2) Another point to be considered is that the dispersion curve can be accurately obtained by using our approach only when there is the energy of single-mode (fundamental mode) in the seismogram. When the higher mode energy of the surface wave is relatively strong, it is necessary to separate

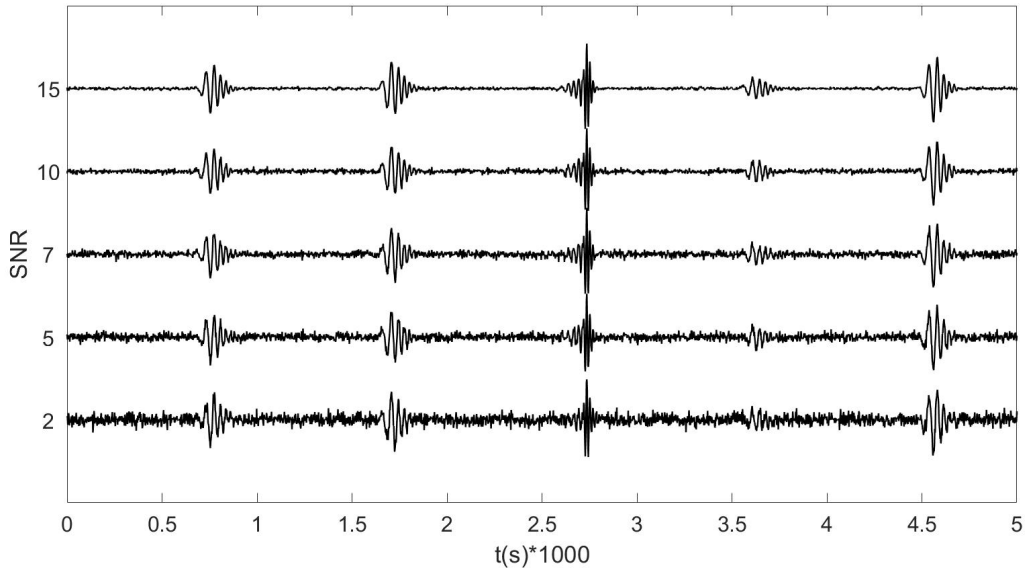

Figure 2.20: The first five seismograms (A_z, S1 direction) of Model 3 with different SNR.

the modes before calculating the dispersion, which is described in detail by Tang & Fang (2023) and Kurrle et al. (2010), but it is currently difficult to use a single station to achieve the mode separation. This is the reason why this method is more suitable for long periods and teleseismic records of shallow seismic sources, when the higher modes are much weaker than the fundamental mode that can be neglected. In the future, with enough rotation sensors, we can use the array method (Tang & Fang, 2023) to separate and calculate the local dispersion of higher modes.

2.6 Conclusion

We derived the expressions for calculating the dispersion curves in weakly anisotropic media, using a single observation point which consists of translational displacement and rotation or strain. We analyzed the influence of surface wave coupling, with effects depending on the anisotropic strength. When the radiation amplitude of the wavefield is very small, the coupled wave will seriously affect the measurements of dispersion curves. Therefore, it is necessary to select a waveform with strong radiation amplitude or use multiple seismograms to fit a stable dispersion value. Even in general anisotropic media, the polarization plane of rotation is perpendicular to the propagation direction, which provides a new method to extract the azimuth of wave propagation. We numerically demonstrate the effectiveness and applicability of the frequency-dependent amplitude ratio method for deriving anisotropy in the Earth.

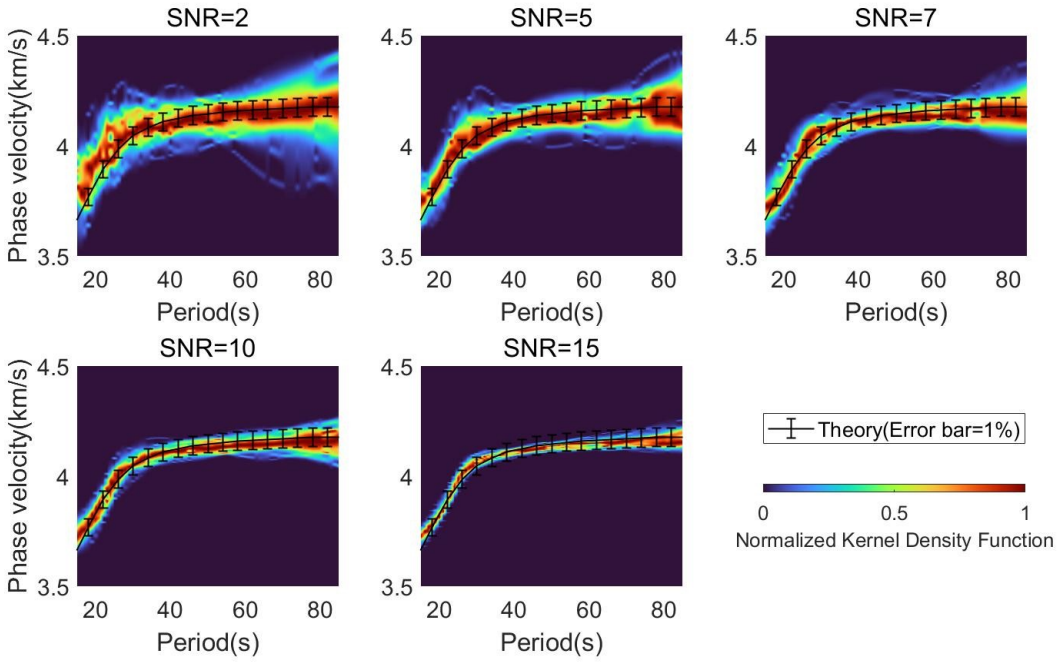

Figure 2.21: Comparisons of dispersion probability energy distribution with different SNR, while each SNR is simulated for 100 times, and analytical solutions of the fundamental mode of HTI Model 3.

2.7 Acknowledgments

This work is funded by the European Union's Horizon 2020 research and innovation program under the Marie Skłodowska-Curie grant agreement No 955515. We thank Prof. Xinding Fang for providing the numerical simulation 3D FD anisotropic code. We thank Prof. Valerie Maupin, Prof. Toshiro Tanimoto, Prof. Huajian Yao and one anonymous reviewer for their constructive comments that help us improve the manuscript.

2.8 Data availability statement

The data underlying this article will be shared on reasonable request to the corresponding author.

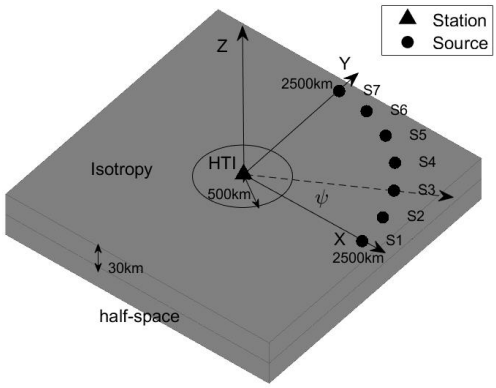

Figure 2.22: Distributions of sources and receiver of Model 4.

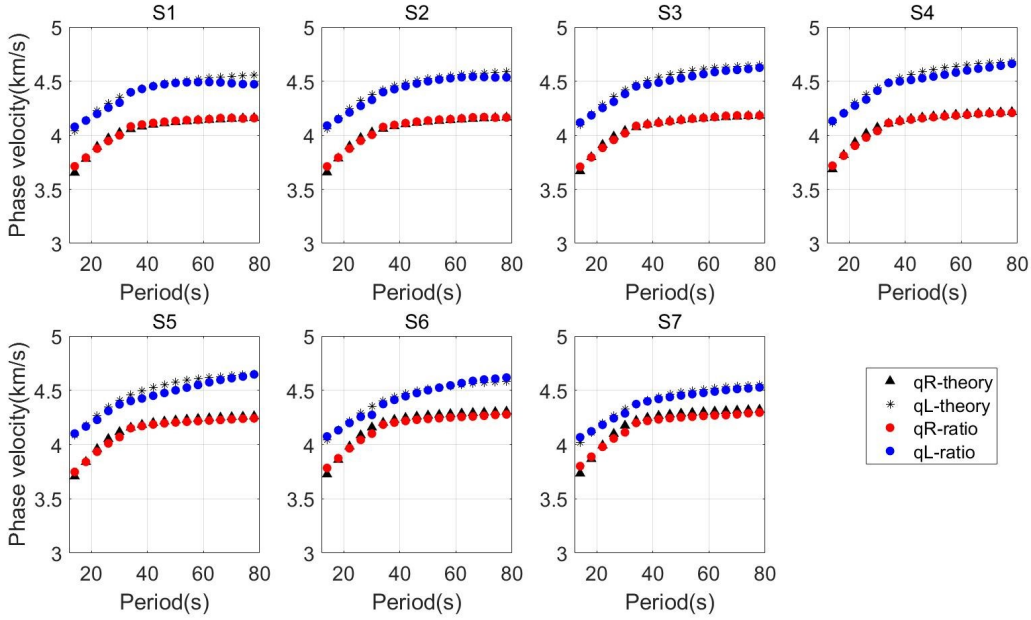

Figure 2.23: Comparisons of dispersion curves calculated using translation-rotation ratio eqs 2.24a and 2.25a and analytical solution of the fundamental mode of the inner cylinder in Model 4.

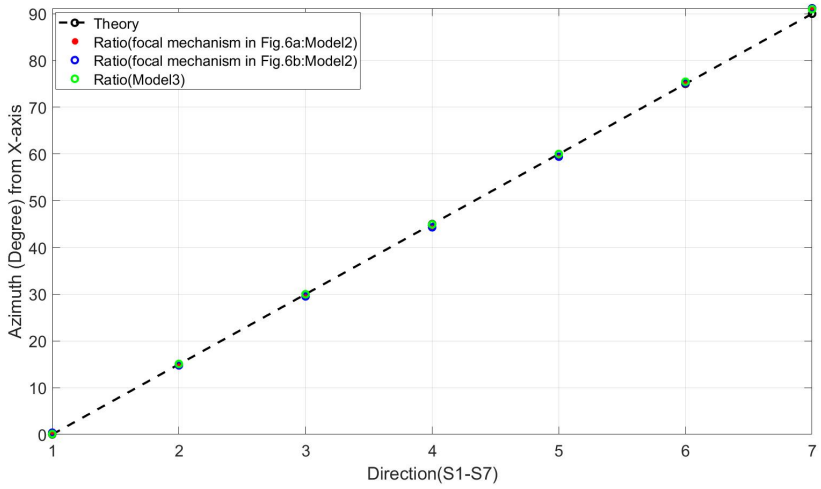

Figure 2.24: Comparisons of azimuth calculated using ratio in eq. 2.42 and analytical solutions with seismograms of Model 2 and Model 3.

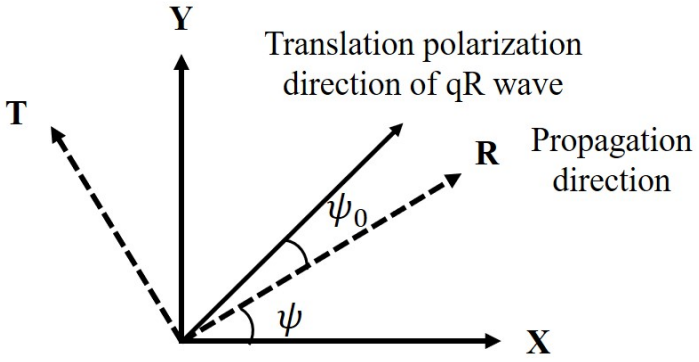

Figure 2.25: Diagram of rotation angle ψ_0

Chapter 3

Anisotropy and deformation processes in Southern California from rotational observations

by Le Tang, Heiner Igel and Jean-Paul Montagner
Published in Geophysical Research Letters (2023), 50(23), e2023GL105970.
https://doi.org/10.1029/2023GL105970

3.1 Key Points

• Local seismic anisotropy revealed for the first time from rotational amplitude observations.
• Azimuthal anisotropy in the local upper mantle of Southern California region is well resolved in lateral and vertical directions.
• The asthenospheric fast axis matches absolute plate motions, providing new insights on geodynamic processes in Southern California.

3.2 Abstract

Seismic anisotropy in the upper mantle reveals geodynamic processes and the tectonic evolution of the Earth. The two most powerful methods, surface wave tomography, and shear-wave splitting observations, cannot investigate the deep local anisotropy with good vertical and lateral resolution, resulting in poor constraints on plate deformation processes of the complex plate boundary beneath the Southern California region. Here, we show that the amplitude ratio of translational displacement and rotation makes it possible to retrieve the local anisotropy in the upper mantle. Azimuthal anisotropy in the asthenosphere is well determined and resolved in lateral and vertical directions. The fast axis retrieved from amplitude observations indicates the local rapid changes in plate deformation and complex

pattern of mantle flow, which is compatible with the distributions of horizontal mantle flow illuminated by geodetic measurements, providing new insights on geodynamic processes of the Southern California region.

3.3 Plain Language Summary

Rotational motion is the angle of ground rotation observed during Earth's deformation, and the ratio of amplitude to translational motion is sensitive to local structure. In the past few decades, study on the mantle structure inside the Earth has mainly relied on the time difference of seismic waves to calculate azimuth-dependent velocity changes, namely azimuthal anisotropy. Due to the correlation between the direction of maximum velocity propagation and the direction of mantle flow and plate deformation, the study of mantle anisotropy can provide evidence for the evolution of the Earth. However, studying anisotropy based on seismic wave travel time is often affected by heterogeneity, especially in extremely complex structures such as Southern California. The splitting of shear waves can effectively constrain the anisotropy of the mantle in the lateral direction, but its depth resolution is poor. Additional rotational amplitude observations with local sensitivity and depth resolution can provide better constraints on the study of mantle anisotropy, providing new evidence for the direction of mantle flow and plate motion.

3.4 Introduction

Seismic anisotropy is a powerful diagnostic tool providing access to information on the orientation of small scale heterogeneities (e.g., cracked, porous media, crystals, bedding (Anderson et al., 1974; Crampin, 1978)) that - in many cases - are aligned according to the local stress or strain field. In turn, principal stress/strain directions can be associated with the direction of mantle flow (Tanimoto & Anderson, 1984; Ribe, 1989; Ghosh & Holt, 2012; Montagner, 1994). Thus, extracting anisotropic properties plays a significant role in understanding subsurface processes such as tectonic motions, reservoir behavior, or stress evolution.

On regional scales, there are two key methodologies to estimate anisotropic parameters. First, the phenomenon of shear-wave splitting (Crampin et al., 1980) of near-vertically propagating waves (e.g., SKS phase (Vinnik et al., 1984; Silver & Chan, 1988)) can be used to estimate the polarization of the fast quasi-shear wave. It is assumed that this polarization is associated with the dominant horizontal stress/strain direction (Crampin & Lovell, 1991). This method has the advantage that a single three-component seismic station can provide the required information. The disadvantage is the lack of resolution with depth (Savage, 1999). Secondly, surface wave observations from many azimuths observed on a sufficiently scaled seismic array can be used to determine azimuthal anisotropy from Love or Rayleigh waves (Forsyth, 1975). This approach - while having some depth resolution through the frequency-dependence of surface wave phase velocities (Montagner & Nataf,

1986) - has a poor lateral resolution. Regional full-waveform inversion approaches (Zhu & Tromp, 2013) intrinsically also provide access to anisotropic parameters by exploiting surface wave phase information across a broad frequency range, but still with a limited lateral resolution.

The local deformation can be divided into a symmetric part (the strain tensor) and an antisymmetric part (three components of rotation). Both are sensitive to seismic anisotropy (Tang et al., 2023c). In the past few years - through the emergence of multi-component rotational ground motion instruments such as ring lasers (Schreiber et al., 2014; Igel et al., 2005, 2021) or fibre-optic gyros (Schreiber et al., 2009) - techniques were developed to exploit the resulting 6-degrees-of-freedom observations (6 dof, three components of rotations and three components of translations) opening a new range of opportunities in particular for single-station observations. Most notably, 6 dof observations provide direct access to local surface wave phase velocities and propagation directions through the analysis of amplitude ratios (Igel et al., 2007), which is capable of extracting the dispersion of different modes of surface waves (Tang & Fang, 2023). By applying adjoint techniques (Fichtner & Igel, 2009) to such joint observations, it could be shown that 6 dof point measurements are sensitive to near-receiver structure, eliminating the path effects of wave propagation.

Here, we apply for the first time the emerging 6 dof technology to the estimation of local anisotropic parameters in the upper mantle from surface wave observations. As currently no (portable) rotation sensing system exists that allows the analysis of multi-azimuth observations, we resort to so-called array-derived rotation (ADR) (Spudich et al., 1995; Spudich & Fletcher, 2008) that makes use of wavefield gradient estimations from surface seismic arrays in appropriate frequency bands.

Southern California - characterized by a complex tectonic and geodynamic environment - is the best location to apply our new approach. The dense broadband seismic networks in California that have operated for decades allow us to use station subsets as arrays and use ADR techniques to estimate rotations and subsequently apply single-station techniques to the resulting 6 dof data. We investigate how the frequency-dependent anisotropic parameters are consistent with other geophysical or geodetic observations and how it provides new information at depth on the layering and change of orientation of azimuthal anisotropy, as the 6 dof approach has a substantially higher lateral resolution for upper mantle anisotropy study than other techniques. Our study motivates the development of high-sensitivity rotation sensors to further extend the potential of 6 dof observations toward the inversion for anisotropy parameters from point measurements.

3.5 Methods

3.5.1 Azimuthal anisotropy from rotational observations

Our recent theory paper (Tang et al., 2023c) demonstrates that the amplitude ratio of acceleration to rotational velocity or strain velocity is equal to the analytical azimuth-dependent phase velocity of the corresponding surface wave (Smith & Dahlen, 1973). Since

the fundamental Rayleigh wave is generally far away from Love wave modes, the coupled wavefield has small effects on the Rayleigh wave amplitude. In this paper, we only consider the fundamental mode of the quasi-Rayleigh wave. The dispersion equation of the dominant quasi-Rayleigh wave from the amplitude ratio can be expressed as (Tang et al., 2023c):

$$\begin{cases} |\frac{A_z(\omega,\psi)}{\Omega_t(\omega,\psi)}| = c_{R0}(\omega) + \frac{1}{2c_{R0(\omega)}}[R_1(\omega) + R_2(\omega)cos(2\psi) + R_3(\omega)sin(2\psi) \\ \qquad\qquad +R_4(\omega)cos(4\psi) + R_5(\omega)sin(4\psi)] \end{cases} \tag{3.1}$$

where $A_z(\omega,\psi)$ is the vertical acceleration and $\Omega_t(\omega,\psi)$ is the transverse rotational velocity. ψ is the backazimuth of the wavenumber vector measured clockwise from the north direction. $c_{R0}(\omega)$ is the phase velocity of the Rayleigh wave for the isotropic medium considered as a reference model. $R_i(\omega)$ $(i = 1, 2, 3, 4, 5)$ are respectively depth integration functions that involve some elastic parameters and eigenfunctions, where we used a simple integration expression derived by (Montagner & Nataf, 1986), whose explicit expressions can be found in Equations (2), (4), and (5) of (Montagner & Nataf, 1986).

Equation 3.1 provides a new method for estimating phase velocities in anisotropic media which only depends on amplitude information. Its sensitivity kernel attains large absolute values only in the vicinity of the receiver but not in the vicinity of the source (Fichtner & Igel, 2009) which means that the phase velocity is only sensitive to the local structure. Its lateral resolution can be several times smaller than one wavelength (Tang & Fang, 2023).

3.5.2 Phase velocity smoothing and variance

To investigate the azimuth-dependent variation in phase velocity, we set up a simple function to smooth the phase velocity points in each period, where the smoothed phase velocity and the standard deviation σ can be expressed as

$$\overline{c_R}(\omega,\psi) = \frac{\sum_{\psi_1=\psi'-\psi_0}^{\psi_1=\psi'+\psi_0} c_R(\omega,\psi_1)}{N}, \psi = \frac{\sum_{\psi_1=\psi'-\psi_0}^{\psi_1=\psi'+\psi_0} \psi_1}{N}, \psi' \in [0, 2\pi] \tag{3.2}$$

$$\sigma(\omega,\psi) = \sqrt{\frac{\sum_{\psi_1=\psi'-\psi_0}^{\psi_1=\psi'+\psi_0}[c_R(\omega,\psi_1) - \overline{c_R}(\omega,\psi)]^2}{N}} \tag{3.3}$$

where ψ_0 is the selected azimuth window width and N represents the number of dispersion points from $\psi' - \psi_0$ to $\psi' + \psi_0$. In the following data analysis, the azimuth window ψ_0 is equal to 60 degrees and ψ' is from 0 to 360 degrees in one degree interval. The selection of the azimuth window is a trade-off when considering the large waveform error of ADR and the best fit between the data and the theoretical anisotropy curve.

3.6 Data

The earthquake data comes from the CI station network (see support information file for station names), and SCEDC (southern California Seismic Network) data center. Considering that broadband rotational seismometers have not been permanently deployed widely,

we selected high-quality permanent broadband seismographs in Southern California region as an array for retrieving rotational motions by using the ADR approach (Spudich et al., 1995; Spudich & Fletcher, 2008). We select 110 teleseismic earthquakes with a magnitude larger than 7.0 (only a few events are between 6.5 and 7.0, see Figure 3.S1) from the global earthquake catalog from November 2014 to November 2022.

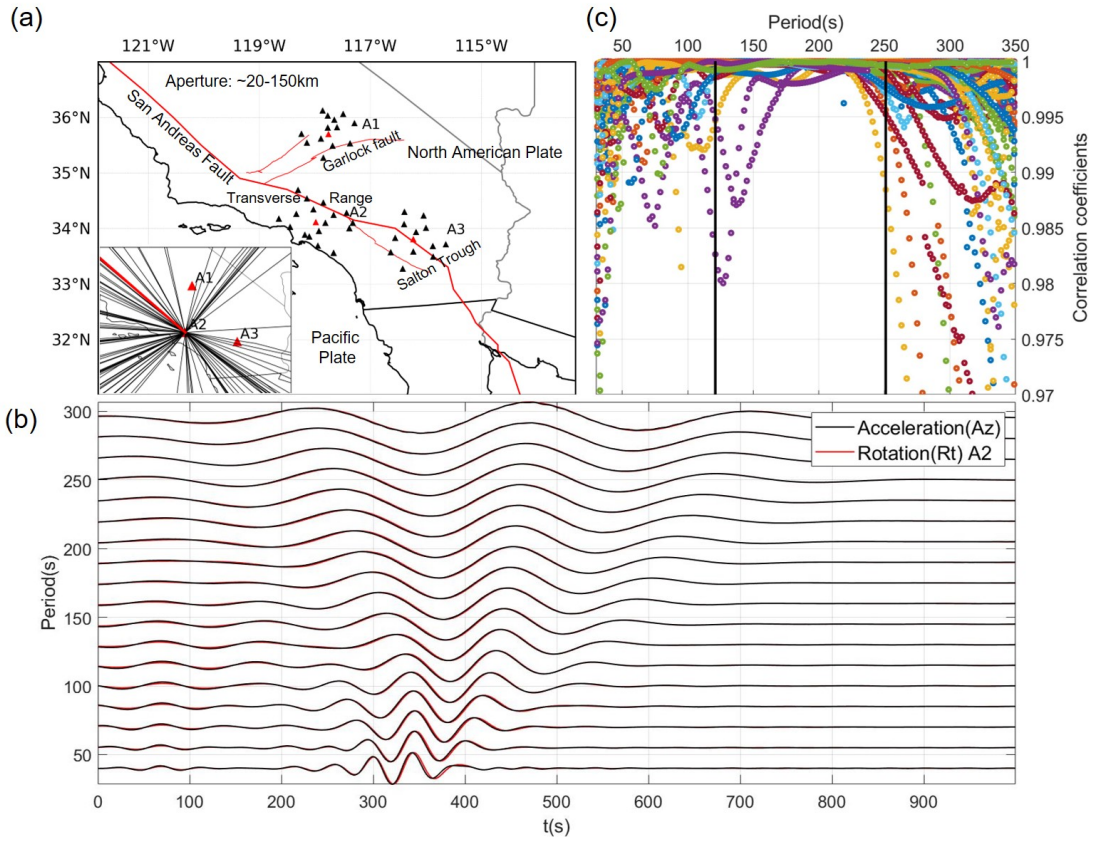

Figure 3.1: (a) Distributions of selected three seismic arrays A1, A2 and A3 and great circle paths from 110 events. The aperture of the three arrays ranges from 20km to 150km. (b) Normalized waveform comparison between translational acceleration (m/s^2) and retrieved rotational velocity (rad/s) using the A2 array from the earthquake: M 8.2 - 99 km SE of Perryville in 2021, Alaska (the red line path in the lower left corner of a). (c) Correlation coefficients of all events between translation and retrieved rotation of the A2 array.

Due to the uneven distribution of permanent stations in Southern California, it is necessary to choose a station array with high waveform quality and evenly spaced distribution at all azimuths as much as possible when using the ADR method. To have sufficient available stations, the minimum distance of the stations we selected is around 20km (see Figure 3.S2), as the spacing between these permanent stations in Southern California is mostly larger than 20km. The minimum aperture limits the high-frequency threshold, while the maximum aperture constraints the low-frequency threshold. Here, we choose a maximum

aperture of around 120km-150km (see Figure 3.S2). After waveform testing, we found that it is sufficient to calculate the waveform of 300s. For longer periods, its amplitude energy is too weak, and we will not consider it in this study. We make use of three broadband seismic arrays (CI network, see Figure 3.S2 for station information) (Figure 3.1a) distributed on three different tectonic regions (Garlock Fault A1, Transverse Range A2, Salton Trough A3) near the plate boundary (the San Andreas fault) between the North American plate and the Pacific plate to understand its local asthenospheric anisotropy. Figure 1a shows the geometry of the stations. The red triangles in Figure 1a are defined to be the central station that outputs the translational displacement. The collection of great circle paths (Figure 3.1a) with enough large events provide a good azimuth coverage for the study of azimuthal anisotropy in the upper mantle.

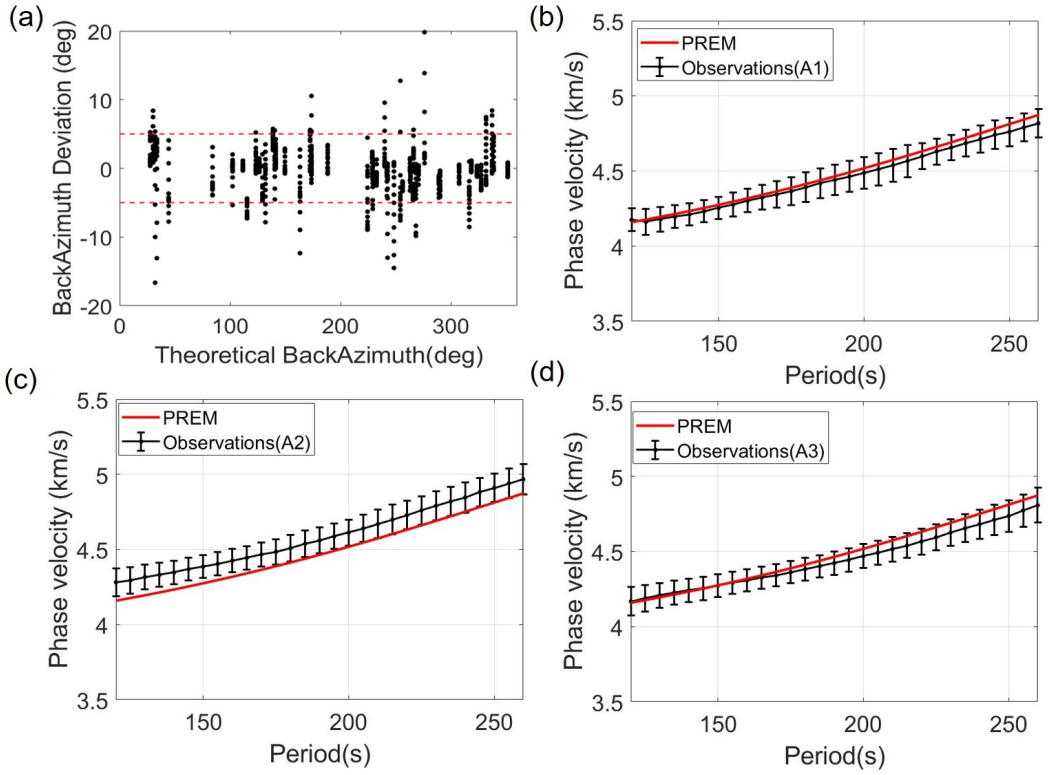

Figure 3.2: Backazimuth deviation and calculated dispersion points. Solid red line is the theoretical phase velocity from isotropic PREM model. (a) Deviations between the great circle path direction and the azimuths calculated by the horizontal rotation components (Tang et al., 2023c) of the A2 array in the period range of 120s to 250s. (b), (c) and (d) are the observed velocity (black lines) of the three arrays calculated using only the data of the azimuth deviations (red dotted line) within 5 degrees in (a). The 1σ uncertainty is about 0.1km/s.

3.7 Results

3.7.1 Rotational motion retrieval and velocity estimation

The red lines in Figure 3.1b show examples of derived rotational waveforms of Rayleigh waves using the A2 (Figure 3.1a) seismic array (see Figure 3.S3 for A1 and A3 waveforms) from the earthquake M8.2 at 99 km SE of Perryville, Alaska, in 2021 (red great circle path in Figure 3.1a). Figure 3.1c shows the correlation coefficient between translation and derived rotation of the A2 array for these 110 events. The high correlation coefficient close to 1 in the period range of 120s to 250s (Figure 3.1c) motivates us to choose this period range for our data analysis. Other period ranges are stronger affected by aperture size and noise. As illustrated in Equation 1 (see Methods section), the local phase velocity can be calculated from amplitude ratios. However, the estimated azimuth can be slightly different from the theoretical great circle path direction due to the effect of heterogeneity along the propagation path. Therefore, it is necessary to correct the azimuths before velocity estimations. From a theoretical point of view, the orthogonality between rotational vector and wavenumber vector allows us to calculate the azimuth using the horizontal rotation components in a general anisotropic medium as proposed by our recent theoretical work (Tang et al., 2023c). The backazimuth deviation of the A2 array compared to the theoretical great circle path direction of all events calculated using horizontal rotation (120s-250s waveform) is shown in Figure 3.2a, which indicates that the deviation of the angle is generally smaller than 10 degrees, and most of them is within 5 degrees. For the period range of 120s-250s, a 5 degree azimuth deviation is reasonable while larger deviations may be due to the error from incorrect amplitude observations and the interference with other wave types. Therefore, we only retain data with azimuth deviation within 5 degrees (within the range of the red dashed line in Figure 3.2a). We use the weighted least-squares method (Tang et al., 2023c) to estimate the phase velocity of the Rayleigh wave based on the amplitude ratio which is shown in Figure 3.2(b-d). The calculated average phase velocity which is marked by a black solid line is close to the theoretical value of the isotropic PREM (Preliminary Reference Earth Model) (Dziewonski & Anderson, 1981), especially for the A1 array. However, the average dispersion curve of the A2 array is slightly larger than that of PREM. In the depth range of the upper mantle corresponding to 120s to 250s (150km-450km), there are two uppermost mantle Transverse Ranges high-velocity anomalies beneath A2, one down to a depth of 175 km, and a second one at depths between 340km and 500 km (Schmandt & Humphreys, 2010). The relatively low velocity beneath A3, west of the Salton Trough, is attributed to partial melt in the asthenosphere as a result of lithospheric thinning (Schmandt & Humphreys, 2010).

3.7.2 Local azimuthal anisotropy in the upper mantle

Figure 3.3 shows the azimuth-dependent phase velocity variation (black dots) for two periods, where the isotropic term $c_{R0}(\omega) + \frac{1}{2c_{R0}(\omega)} R_1(\omega)$ is subtracted (see Figures 3.S4-3.S6 for

other periods). Because the data coverage of some azimuth range is poor (see Figure 3.2a), and some data are not available due to large amplitude errors, we average the velocity estimates in large 120-degree azimuth bins (see Methods section). This leads to the relatively large uncertainties of phase velocity of around 0.1km/s (Figures 3.3 and 3.S4-3.S6). The red and blue curves in Figure 3.3 are the best-fit curves for 2ψ and $2\psi + 4\psi$ terms in Equation (1), respectively. It can be seen that the estimated phase velocity and 2ψ curve fit well. The curve difference between 2ψ and $2\psi + 4\psi$ is very small (see Figure 3.S7) as the 4ψ term for Rayleigh waves is negligible (Montagner & Nataf, 1986). Considering the heterogeneous character of the Southern California region (Schmandt & Humphreys, 2010), the azimuthal velocity variation in the upper mantle can be the result of a mixture of heterogeneity and anisotropy. Although our method measures the local anisotropy, the influence of heterogeneity in the wavelength range cannot be ignored. To quantitatively evaluate the influence of these factors, we calculated the 1ψ best-fit curve (green curve in Figure 3.3, 3.S7) and the isotropic curve misfit (black curve in Figure 3.S7) to investigate the effect of a dipping formation (1ψ) and seismic anisotropy. For most periods, the misfit of 2ψ and $2\psi + 4\psi$ is significantly smaller than the misfit of the 1ψ term (Figure 3.S7), indicating that the effect of anisotropy dominates. However, at the period of 130s-170s for the A1 array, 180s-220s for the A2 array, and 140s-150s for the A3 array (Figure 3.S7), the misfit of 1ψ is very close to that of 2ψ implying that the velocity also contains the effect of local strong heterogeneity (Schmandt & Humphreys, 2010). Even though the distance between the three arrays (about 200km, see Figure 3.S2) is much smaller than the wavelength (120s-250s: 500km-1200km), the fast wave directions of the three arrays indicate significant differences in anisotropy pattern, especially between arrays A1 and A2 or A3. Because our approach has a local sensitivity kernel (Fichtner & Igel, 2009), mainly revealing the properties of the medium beneath the station, the lateral resolution can be several times smaller than the wavelength (see Figures 3.S9-3.S12 for synthetic tests of lateral resolution). The peak-to-peak anisotropy strength fluctuates in a large range due to the error in extracting the rotation amplitude from the incomplete regular seismic array, and its strength between 0.5% and 1% (Figure 3.S8) is compatible with previous studies (Yang & Forsyth, 2006; Alvizuri & Tanimoto, 2011; Marone & Romanowicz, 2007). The uncertainty in the orientation of the azimuthal anisotropy is within 15 degrees for most periods, allowing us to analyze the local plate deformation of Southern California region.

3.8 Discussion

3.8.1 Mantle flow and plate deformation by local anisotropy observations

We estimate the corresponding depth range of anisotropic properties based on Rayleigh waves sensitivity kernels of the PREM model (Dziewonski & Anderson, 1981) and compare them with joint inversion results using SKS and surface wave data (Marone & Romanowicz, 2007), SKS results (Becker et al., 2012) and geodetic results (Barbot, 2020). At a depth

of 200km, the most sensitive periods of Rayleigh waves are in the range of 140s-170s. The fast directions (Figure 3.4) of the three arrays obtained by our method (blue solid lines) are in good agreement with the direction of the APM (absolute plate motion, black arrows) (Gripp & Gordon, 2002).

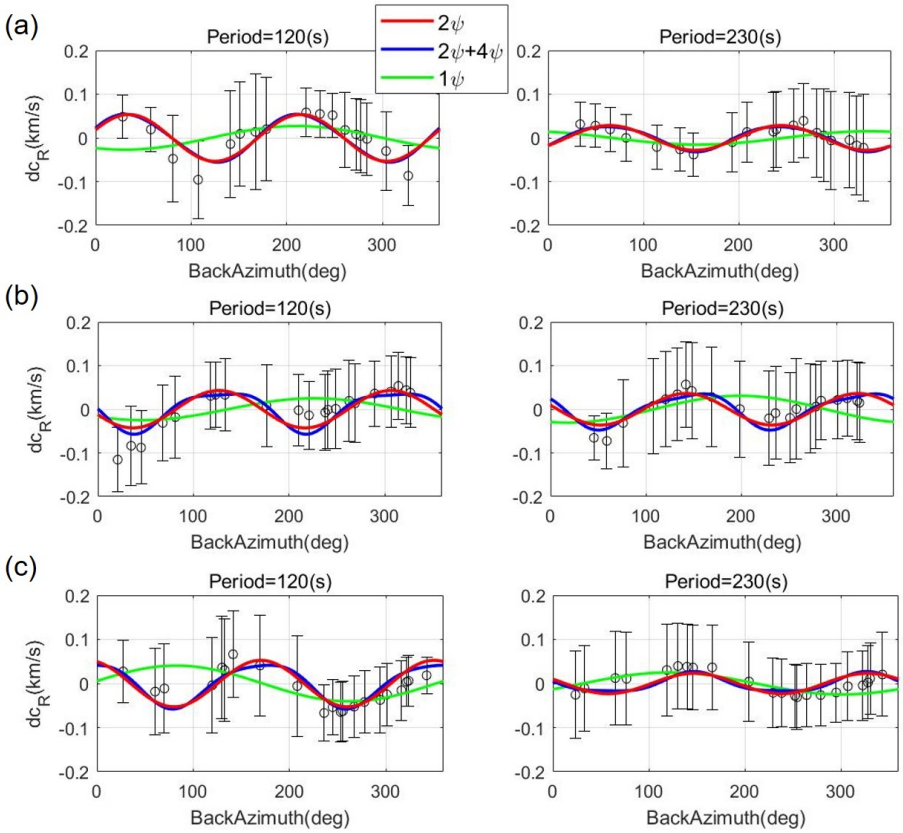

Figure 3.3: Variation of azimuth-dependent phase velocity. Red lines are the best-fit 2ψ curves. Blue lines are the best-fit curves when 2ψ and 4ψ terms are included. Green lines are the best-fit 1ψ curves. (a), (b) and (c) are the smoothed phase velocity (black points) at three different periods from the A1, A2 and A3 array, respectively. The 1σ uncertainty (about 0.1km/s) is estimated in an azimuth bin based on Equations (7) and (8).

However, the lateral resolution of tomography methods (black solid lines) is limited by the long period wavelength, making it difficult to distinguish the difference of local anisotropy between the three observation points. Even though the SKS results (green lines) display some differences in the anisotropy directions of the three arrays, the derived fast axis directions deviate substantially from the direction of the APM, especially at A2 and A3 arrays. Because the SKS results represent the integral effects of the whole upper mantle, making it difficult to specifically study anisotropy in the asthenosphere depth range, and to discriminate it from the strong anisotropy observed in the lithosphere of Southern California region (Yang & Forsyth, 2006; Alvizuri & Tanimoto, 2011) due

to the collision of plates. The distribution of horizontal mantle flow (black dashed lines with arrows in Figure 3.4) below the lithosphere obtained from geodetic data is in good agreement with the results of our amplitude-based observations, especially at A2 and A3. The fast direction of the Rayleigh wave above the lithosphere near the A2 array (yellow lines in Figure 3.4) is parallel to the direction of relative motion along the San Andreas fault (Alvizuri & Tanimoto, 2011), and this anisotropy is interpreted as shear deformation from the collision of the two plates. In the asthenosphere, the fast wave direction is northwest-southeast (blue lines in Figure 3.4), and there is about 20 degrees angle with respect to the fault orientation, which indicates that the anisotropy mechanism of the mantle here is different from that of the lithosphere, possibly controlled by the horizontal mantle flow (Barbot, 2020). The obvious anisotropy drop in the period range of 140s to 170s (about 200km depth, Figures 3.S4-3.S6 and Figure 3.S8) in three arrays provides a new evidence of layering of anisotropy probably indicating the lower boundary of the low-velocity zone (LVZ) and the significant anisotropy in the middle of LVZ (Karato, 2012). The fast direction of the asthenosphere (blue lines in Figure 3.4) near the A3 array is basically parallel to the plate boundary. However, its anisotropy originates from complex mantle dynamics which is not only affected by an upwelling beneath the Salton Trough (Humphreys et al., 1984; Kohler, 1999; Yang & Forsyth, 2006) (Salton Buttes, a group of volcanoes), but also a nearby return flow (Barbot, 2020), where the direction of the mantle flow is rapidly changing. In contrast, the fast direction of the lithosphere (Alvizuri & Tanimoto, 2011) near A1 (yellow lines in Figure 3.4) is consistent with the results of SKS, parallel to the direction of the White Wolf and Garlock faults, while the direction of the mantle flow here (Barbot, 2020) is also parallel to the fault direction. Combining geodetic measurements and the evidence from our local anisotropy observations, the horizontal mantle flow in Southern California indeed has a sharp bend along the San Andreas fault (plate boundary), while vertical mantle flow may exist, which results in extremely complex plate deformation (wide blue shaded arrows), faulting distribution and strong heterogeneity (Tape et al., 2009), revealing its complex tectonic evolution history (Atwater, 1998). So far, we have only three points of local anisotropy measurements in Southern California. In the future, additional observations of rotation could be employed to better constrain the complex geodynamics of upper mantle regions.

3.8.2 Limitations of the ADR approach

In our theoretical study (Tang et al., 2023c), the local seismic anisotropy can be revealed by the amplitude ratio between acceleration and rotation rate. At present, there are no broadband rotational seismometers with sufficient sensitivity in the Southern California region (or elsewhere). To demonstrate the potential of our approach, we selected three high-quality seismic arrays to retrieve rotational waveforms based on the ADR approach (see supporting material) in the Southern California region. The ADR is our only choice to retrieve the rotational waveform even though it has some limitations. The period range is limited by the aperture of the seismic array, the noise level, the amplitude errors of instruments (Spudich et al., 1995; Spudich & Fletcher, 2008; Donner et al., 2017). To estimate a

reliable phase velocity of Rayleigh waves, we set two key thresholds to evaluate and select available rotational waveforms. One is to quantify the similarity between translation and rotation (Figure 3.1). The other is to quantify the azimuth deviation between theoretical and estimated azimuths from horizontal rotation components (Figure 3.2).
Strong wavelength-scale heterogeneity underneath the array will undermine the assumption of homogeneity on which ADR methods are based. In addition, the non-uniformity of the geometric distribution of stations affects the phase and amplitude of the retrieved rotational waveform. Small errors in the waveform can lead to considerable deviations in the estimated velocity, which indicates that waveform quality control based on correlation coefficients (Figure 3.1c) is extremely important.

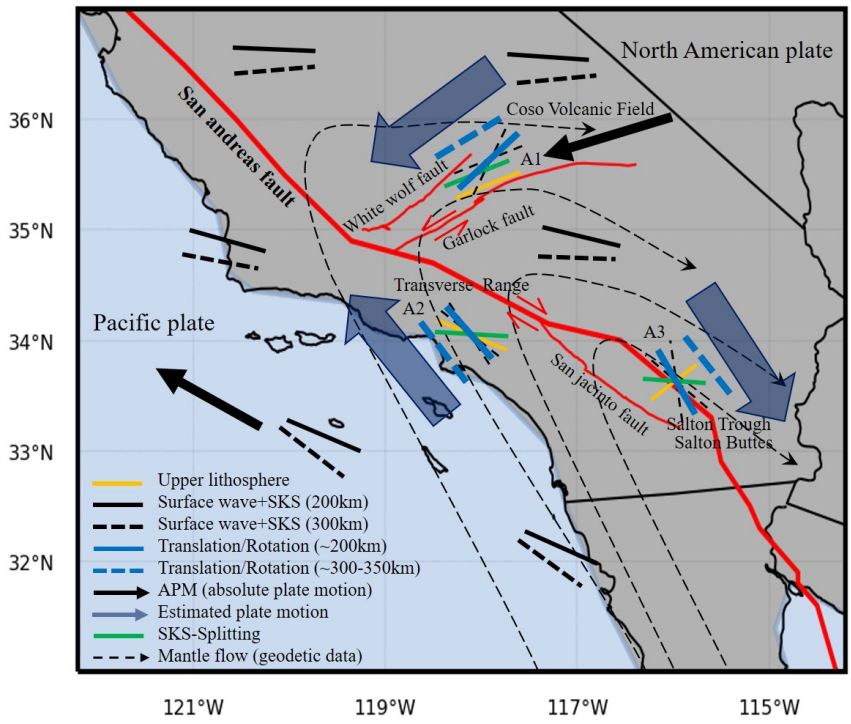

Figure 3.4: Comparison of fast wave directions from different methods. The solid black line and dashed black line represent the S-wave fast wave directions jointly retrieved by SKS and surface waves (Marone & Romanowicz, 2007) at depth of 200km and 300km, respectively. The solid blue line and dashed blue line represent the Rayleigh wave fast directions retrieved by the amplitude ratio between translation and rotation at depth of about 200km and 300km, respectively. The black arrow represents the APM directions (Gripp & Gordon, 2002). The green lines represent the fast directions of SKS splitting (Becker et al., 2012). The dashed black lines with arrows are the horizontal mantle flow streamlines retrieved by geodetic data (Barbot, 2020). Yellow lines represent the fast direction of Rayleigh wave in the upper lithosphere estimated from the beamforming method (Alvizuri & Tanimoto, 2011) and blue shaded arrows are estimated plate motion directions from the amplitude ratio method.

Consequently, there is an urgent need to develop and deploy portable broadband rotational seismometers with a low noise level (Igel et al., 2021), since direct observations of rotation can eliminate the period limitation of the ADR method and errors caused by irregular deployment of stations.
A key point in the study of azimuthal anisotropy is to extract accurate backazimuths. For the surface wave with a period of 120s to 250s in this paper, we assume that the deviation of its azimuth comes from waveform errors, rather than the influence of heterogeneity on the propagation path. However, strong heterogeneity, such as in the Southern California region, can lead to significant deviation in the azimuths (Alvizuri & Tanimoto, 2011), especially at the lithospheric scale. Therefore, azimuth correction is generally necessary, and Tang et al. (2023c) also provides a method of estimating the backazimuth using the horizontal rotation waveform.

3.9 Conclusion

Based on the amplitude ratio between translational displacement and rotation, local structure and anisotropy can be extracted with a good lateral and vertical resolution at the same time. It allows us to recover the azimuthal anisotropy of the upper mantle and to study the plate deformation and local mantle flow with orientation changes at depth, providing new insights on geodynamic processes and tectonic evolution for the complex Southern California region. It provides strong constraints for the layering of the upper mantle anisotropy that remains poorly constrained from current seismological observations methods, SKS splitting, or surface wave tomography. While the array aperture limits the frequency range, the analysis presented should provide motivation to further improve the sensitivity of rotation sensors below the Earth's low noise level such that in the future the proposed technique could be applied to single stations. It is expected that the approach would be particularly useful whenever seismic arrays are not affordable or difficult to implement (e.g., planetary or ocean bottom observations, volcanology, urban seismology, or structural engineering).

3.10 Acknowledgments

This work is funded by the European Union's Horizon 2020 research and innovation program under the Marie Skłodowska-Curie grant agreement No 955515. HI gratefully acknowledges the support from the Cecil and Ida Green Foundation for visits to the Institute of Geophysics and Planetary Physics at the University of Southern California San Diego in 2022 and 2023. We are also grateful for comments from Frank Vernon and Gabi Laske.

3.11 Open Research

All waveforms are from CI network of Southern California which are publicly available and accessed from (SCEDC, 2013): Southern California Earthquake Center. The SKS splitting database are available from Barruol et al. (2009). The shear-wave splitting database are available from Alvizuri & Tanimoto (2011). The fast wave directions from joint inversion of surface wave data and SKS are available from Marone & Romanowicz (2007). The horizontal mantle flow directions are available from Barbot (2020). Codes and station names used in the paper are available from tangle0129 (2023).

3.12 Appendix: Supplementary materials

Contents of this file
Text 3.S1 to 3.S2
Figures 3.S1 to 3.S12

3.12.1 Supplementary text

Lateral resolution
To demonstrate the lateral resolution of our method can be several times smaller than the wavelength. We setup a half-space checkerboard HTI (Horizontal transversely isotropic) model with 2% anisotropy for P wave=8.0km/s and S wave=4.0km/s. As illustrated in Figure 3.S9, each sub-model (100km*100m) and its surrounding sub-models have orthogonal fast directions. There are 13 sources are distributed on a surface circle 3450km away from the center of checkerboard at every 30 degrees, and the outside of the checkerboard is anisotropic medium. Synthetic results at three periods 150s, 200s, and 250s in Figures 3.S10-3.S12 indicate that the local fast directions can be distinguished clearly and are in agreement with analytical solutions even though the wavelength is many times larger than the sub-models.
Array Derived Rotation (ADR)
We briefly summarize the ADR method as introduced by Spudich et al. (1995). Let $\mathbf{r}^i(i = 0, 1, ..., N)$ be the coordinate of the i-th seismic station and $\mathbf{R}^i = \mathbf{r}^i - \mathbf{r}^0$ is the coordinate difference from the station $\mathbf{r}^i$ to the central station $\mathbf{r}^0$. The rotation and strain can be together characterized by a 3*3 displacement gradient matrix $\mathbf{G}(G_{xy} = u_{x,y})$, where $u_{x,y}$ is the derivative of x-component of displacement with respect to the y direction. At the free surface, the rotation can be expressed as:

$$\begin{cases} \Omega_x = u_{z,y} \\ \Omega_y = -u_{z,x} \\ \Omega_z = \frac{1}{2}(u_{y,x} - u_{x,y}) \end{cases} \tag{3.S1}$$

Under the assumption of spatially uniform displacement, the gradient can be expressed

as:

$$\mathbf{d}^i = \mathbf{G}\mathbf{R}^i \tag{3.S2}$$

where $\mathbf{d}^i = \mathbf{u}^i - \mathbf{u}^0$ The rotation can be retrieved by solving $\mathbf{G}$ in Equation 3.S2.

The solution $\mathbf{P} = (u_{x,x}, u_{x,y}, -u_{z,x}, u_{y,x}, u_{y,y}, -u_{z,y})$ (Because of the free-surface boundary condition, $\mathbf{G}$ has only six nonzero elements) of Equation 3.S2 can be expressed as (Spudich et al., 1995):

$$\mathbf{P} = (\mathbf{A}^T\mathbf{C}_d^{-1}\mathbf{A})^{-1}\mathbf{A}^T\mathbf{C}_d^{-1}\mathbf{d} \tag{3.S3}$$

where $\mathbf{C}_d = \mathbf{D}\mathbf{C}_u\mathbf{D}^T$ is the covariance matrix of $\mathbf{d}$, $\mathbf{C}_u$ is assumed to be $\sigma_u^2\mathbf{I}_{3(N+1)}$. $\mathbf{I}_3$ is the 3*3 identity matrix and $\mathbf{0}_3$ is a 3*3 matrix zeros. $\eta = \frac{\lambda}{\lambda+2\mu}$, η and μ are the Lame's parameters. where

$$\mathbf{A}^i = \begin{pmatrix} R_x^i & R_y^i & R_z^i & 0 & 0 & 0 \\ 0 & 0 & 0 & R_x^i & R_y^i & R_z^i \\ -\eta R_z^i & 0 & -R_x^i & 0 & -\eta R_z^i & -R_y^i \end{pmatrix} \tag{3.S4}$$

$$\mathbf{D} = \begin{pmatrix} -\mathbf{I_3} & \mathbf{I_3} & \mathbf{0_3} & \dots & \mathbf{0_3} \\ -\mathbf{I_3} & \mathbf{0_3} & \mathbf{I_3} & \dots & \dots \\ \dots & \dots & \dots & \dots & \mathbf{0_3} \\ -\mathbf{I_3} & \mathbf{0_3} & \dots & \mathbf{0_3} & \mathbf{I_3} \end{pmatrix} \tag{3.S5}$$

where rotational components in Equation 3.S1 can be derived from elements of $\mathbf{P}$.

3.12.2 Supplementary figures

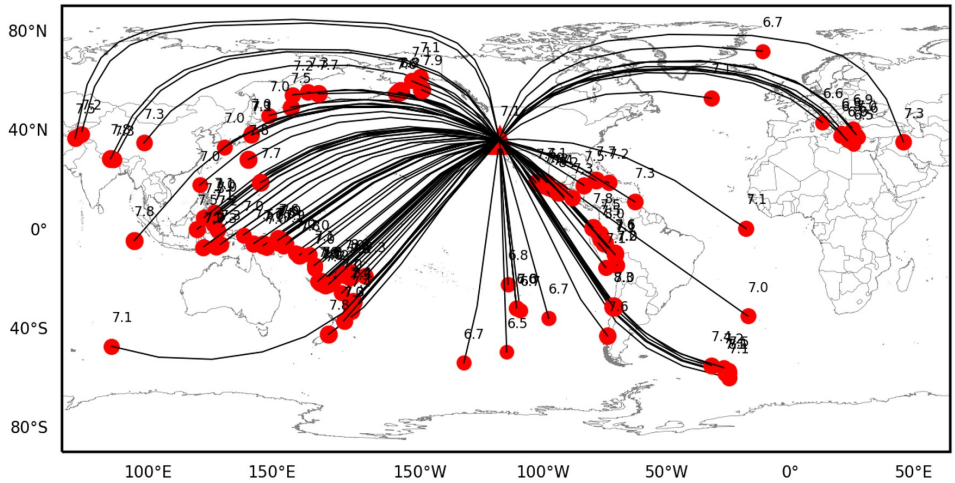

Figure 3.S1: (a) Distributions of 110 events with magnitude larger than 7.0 (only a few events are between 6.5 and 7.0) from the global earthquakes catalog from November 2014 to November 2022.

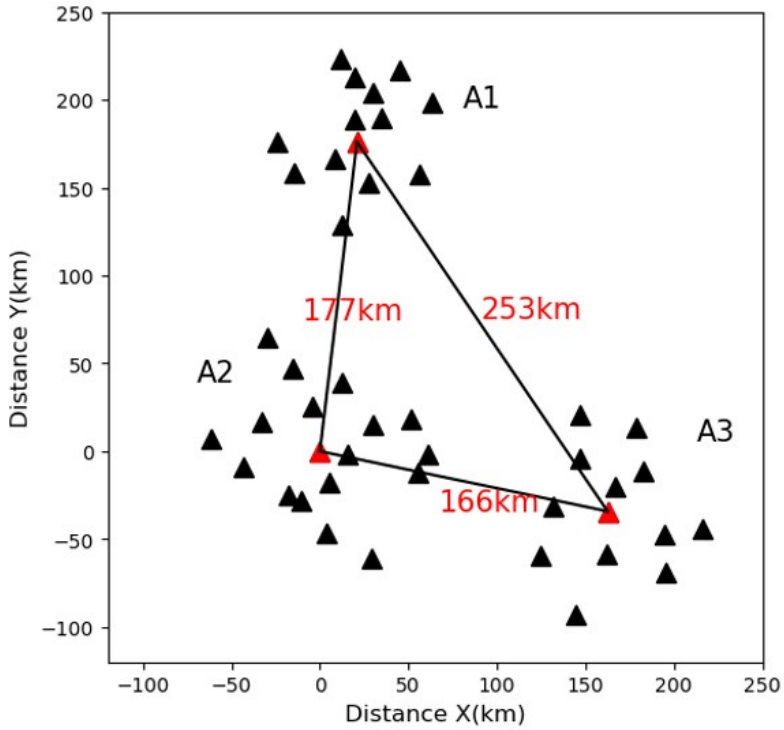

Figure 3.S2: Relative locations of three Broadband seismic arrays. A1 has 14 stations (CI.SRT, CI.WBM, CI.TOW2, CI.LRL, CI.CLC, CI.CCC, CI.WRC2, CI.WCS2, CI.WMF, CI.MPM, CI.SLA, CI.WBS, CI.WOR, CI.DTP), A2 has 18 stations (CI.RIO, CI.LTP, CI.DLA, CI.OLI, CI.PSR, CI.SMF2, CI.LLS, CI.DEC, CI.CJV2, CI.CHF, CI.SDD, CI.WSS, CI.BFS, CI.CLT, CI.CJM, CI.RVR, CI.ALP, CI.HOL) and A3 has 13 stations (CI.IDO, CI.KYV, CI.PSD, CI.CTW, CI.BEL, CI.MCT, CI.HAY, CI.GMA, CI.SLB, CI.DNR, CI.BOR, CI.TOR, CI.BLA2). The red stations are used to output the translation. All stations are from CI network of Southern California. The seismometers contain STS2, CMG3, Trillium and PBB.

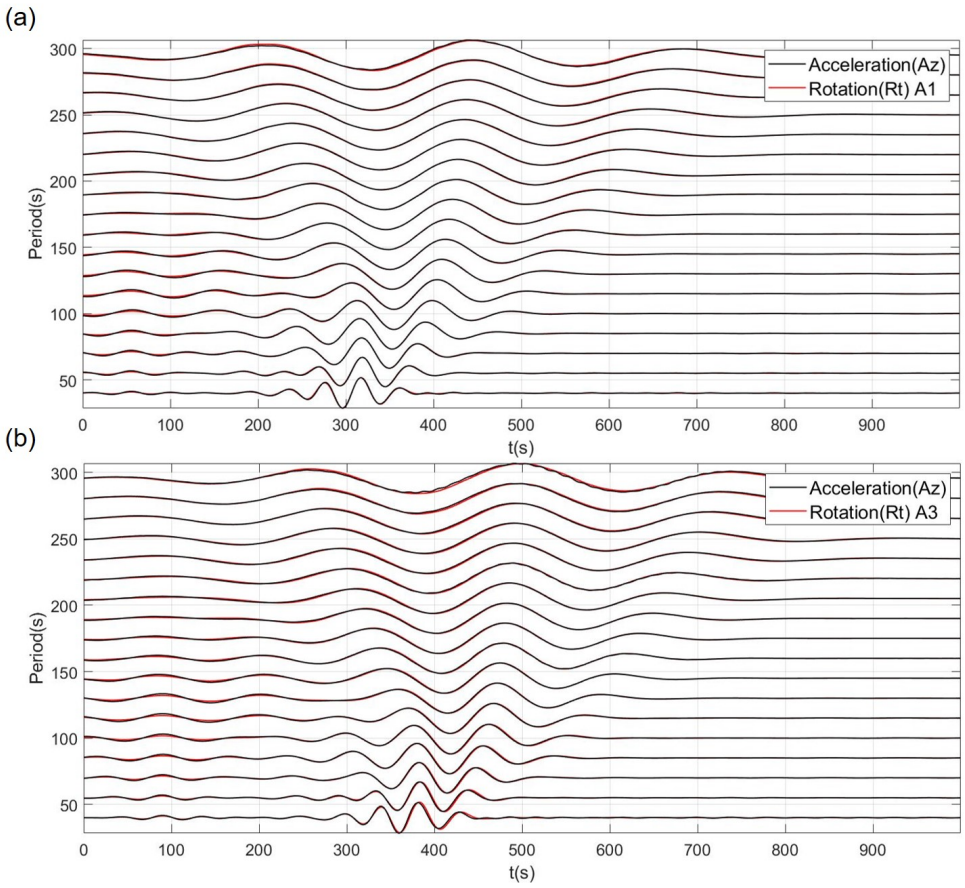

Figure 3.S3: Normalized waveform comparison between translational acceleration (m/s^2) and retrieved rotational velocity (rad/s) using the A1 and A3 arrays from the earthquake: M 8.2 - 99 km SE of Perryville in 2021, Alaska.

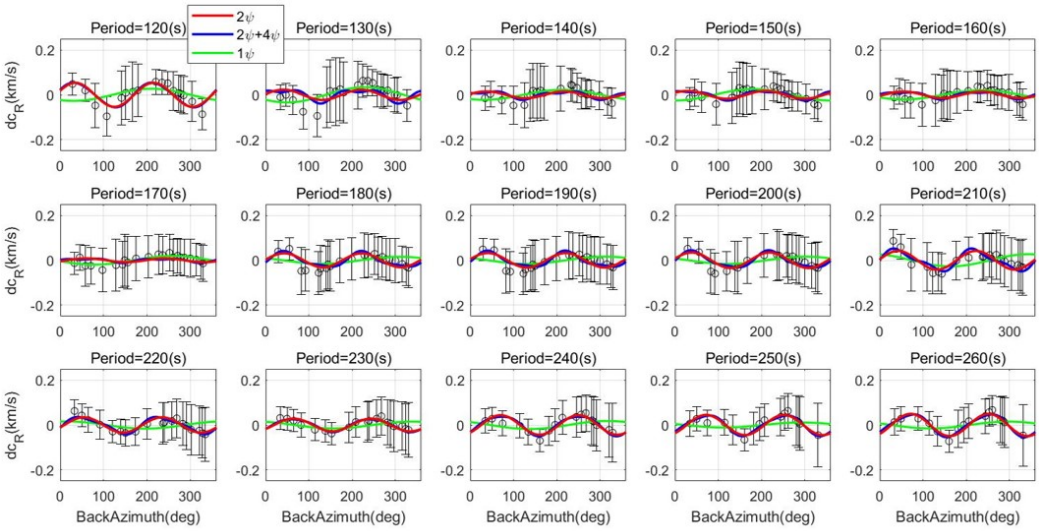

Figure 3.S4: Velocity variation of A1 array from 120s to 260s. Red lines are the best-fit 2ψ curves. Blue lines are the best-fit curves when 2ψ and 4ψ terms are included. Green lines are the best-fit 1ψ curves.

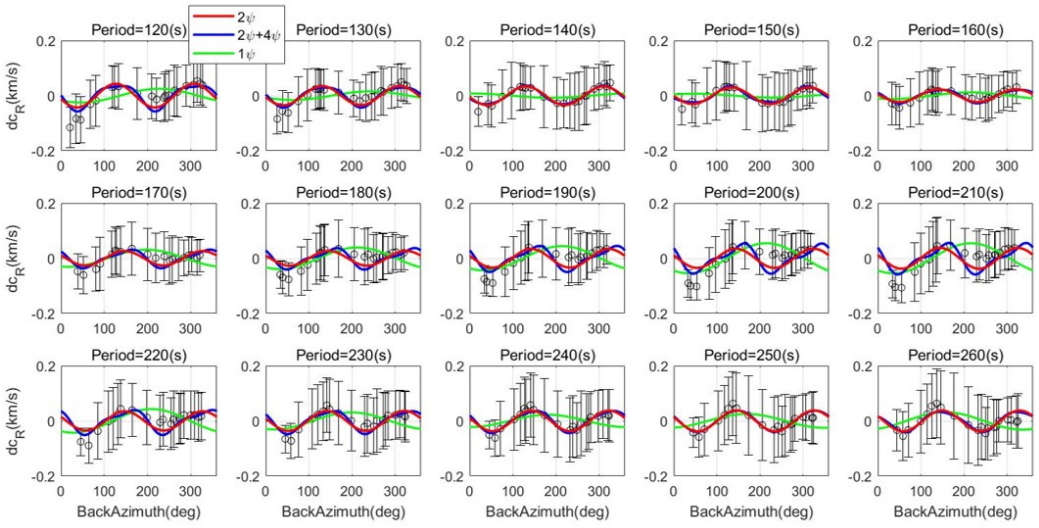

Figure 3.S5: Velocity variation of A2 array from 120s to 260s.

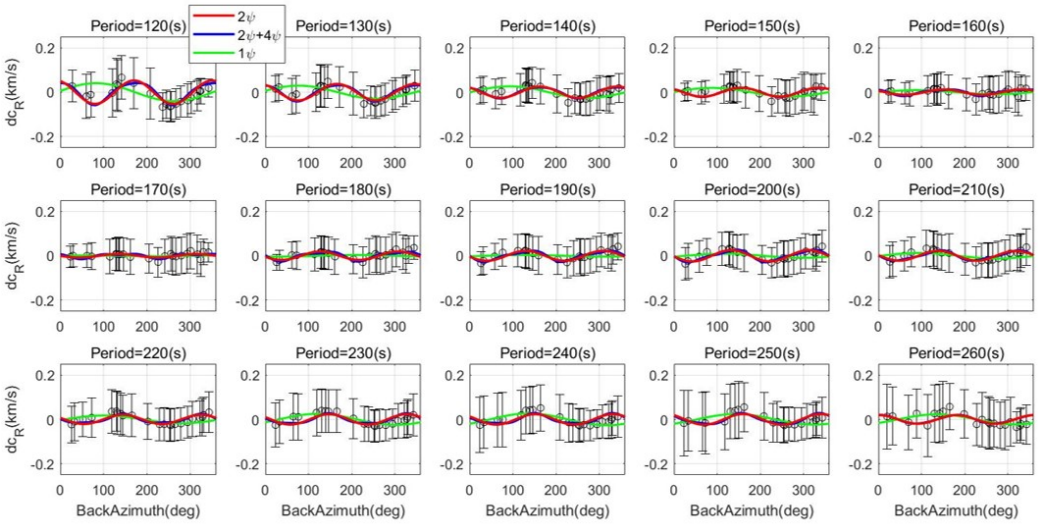

Figure 3.S6: Velocity variation of A3 array from 120s to 260s.

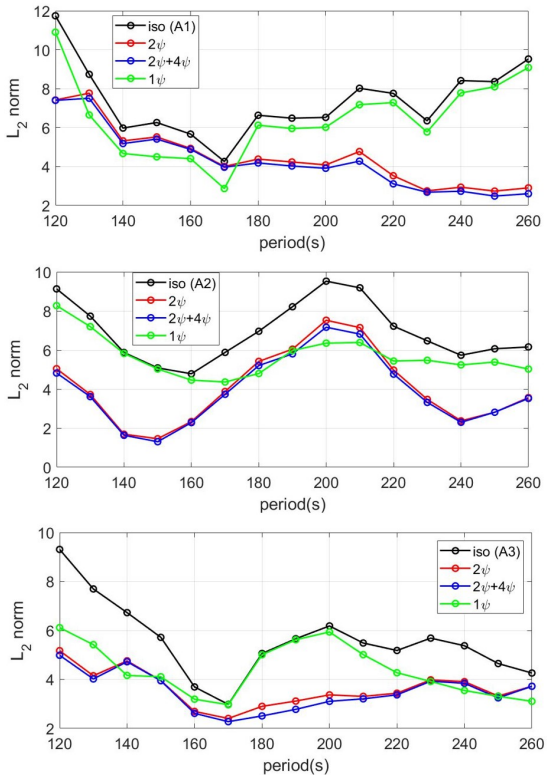

Figure 3.S7: The L2 norm of three arrays between observed phase velocity and estimated phase velocity (best-fit curve). Black curve: the isotropic best fit curve. Red curve: the 2ψ best fit curve. Blue curve: the $2\psi + 4\psi$ best fit curve. Green curve: the 1ψ best fit curve.

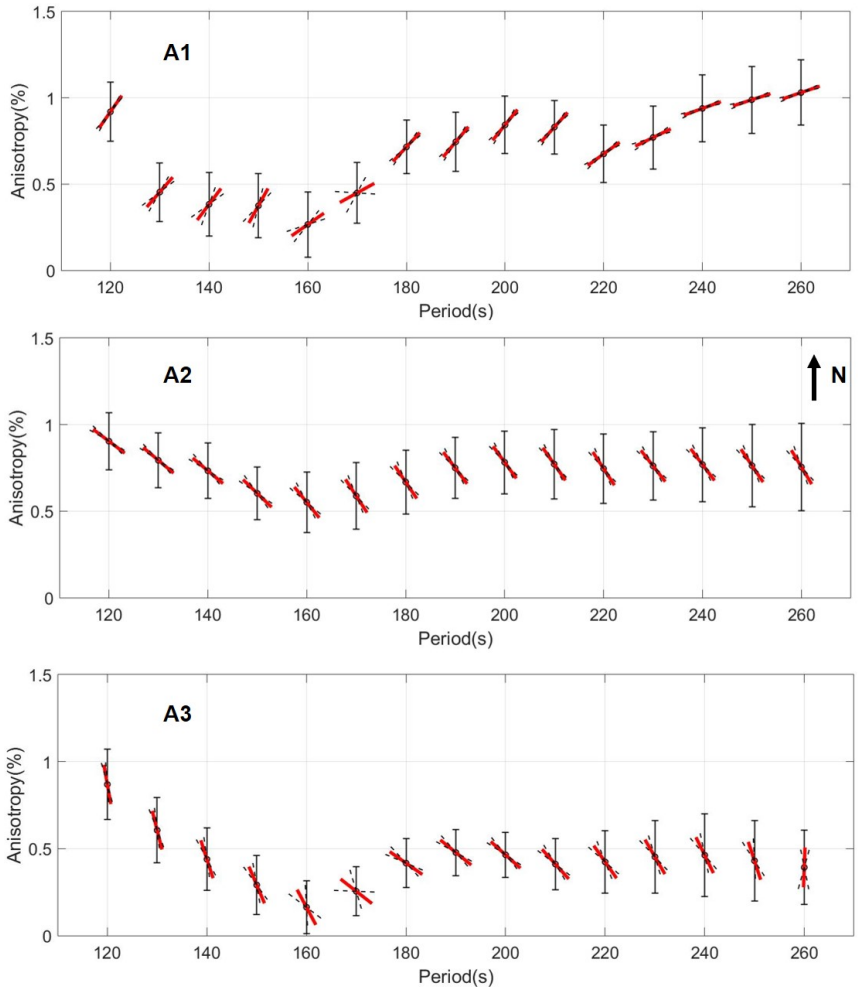

Figure 3.S8: Fast-axis directions and peak-to-peak anisotropy of A1, A2, and A3 arrays.

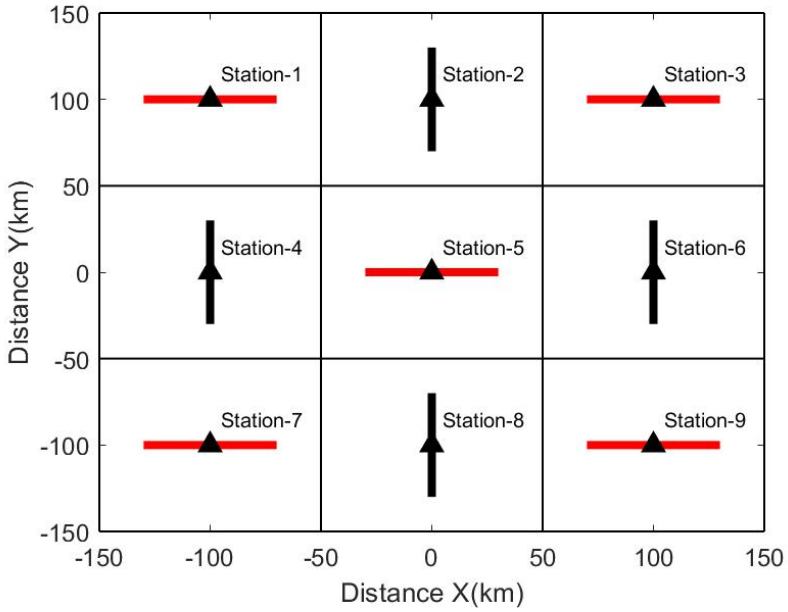

Figure 3.S9: Half-space checkerboard HTI (horizontal transversely isotropic) model with 2% anisotropy for $P = 8.0km/s$ and $S = 4.0km/s$ velocity. The black triangles represent the 9 stations located in a 100km*100km anisotropic sub-model. The red lines indicate that the fast wave axis along the X-axis (azimuth is 0 or 180 degrees). The black lines indicate that the fast wave axis along Y-axis (azimuth is 90 or 270 degrees).

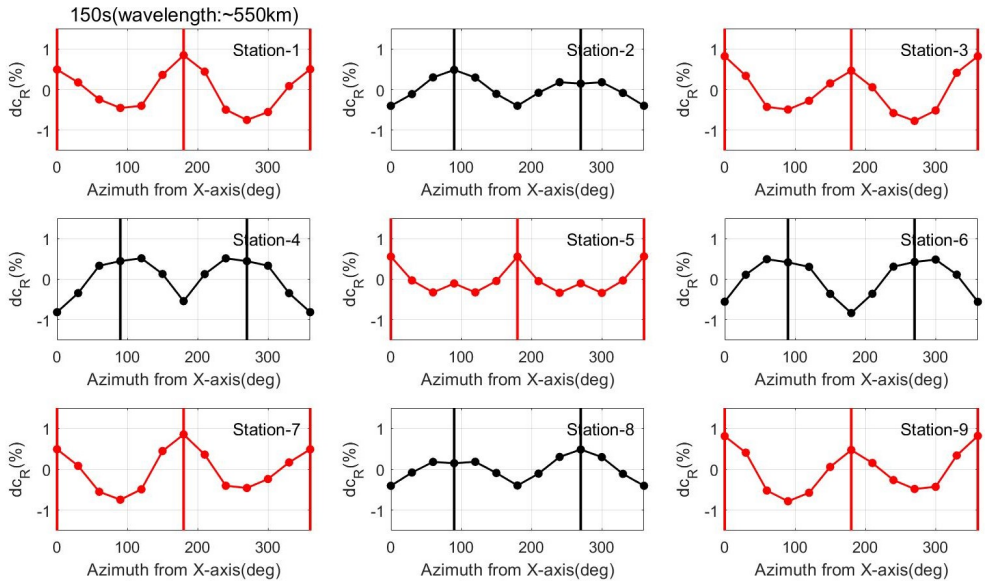

Figure 3.S10: Azimuthal anisotropy of Rayleigh wave of checkerboard model at 150s (wavelength is about 550km, anisotropic sub-model is 100km*100km in Figure S9) using the amplitude ratio Equation (1). The vertical solid lines (red and black) represent the theoretical fast directions. The fast directions are in agreement with the theoretical model (red curves: 0 or 180 degrees and black curves: 90 or 270 degrees).

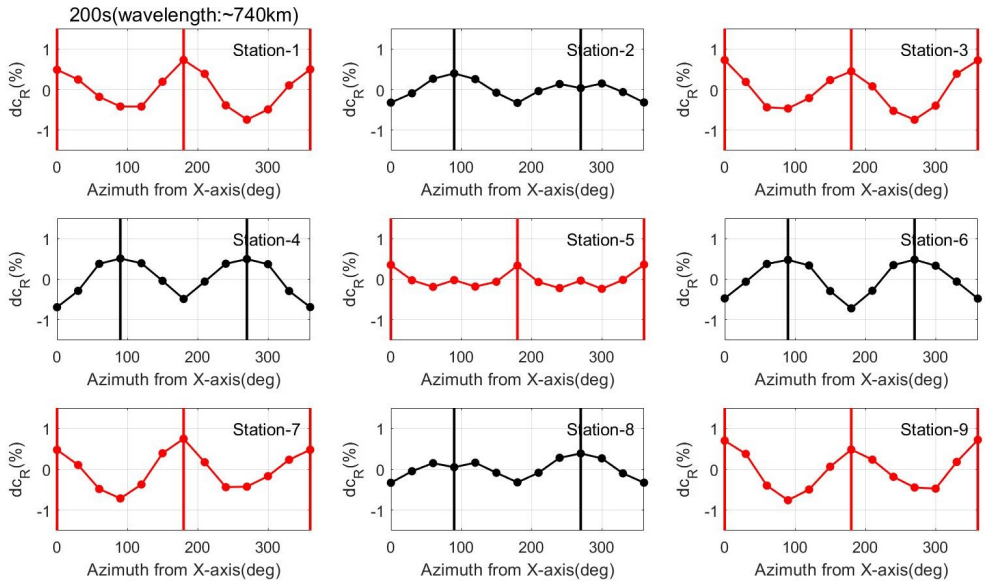

Figure 3.S11: Azimuthal anisotropy of Rayleigh wave of checkerboard model at 200s (wavelength is about 740km, anisotropic sub-model is 100km*100km in Figure S9) using the amplitude ratio Equation (1). The vertical solid lines (red and black) represent the theoretical fast directions. The fast directions are in agreement with the theoretical model.

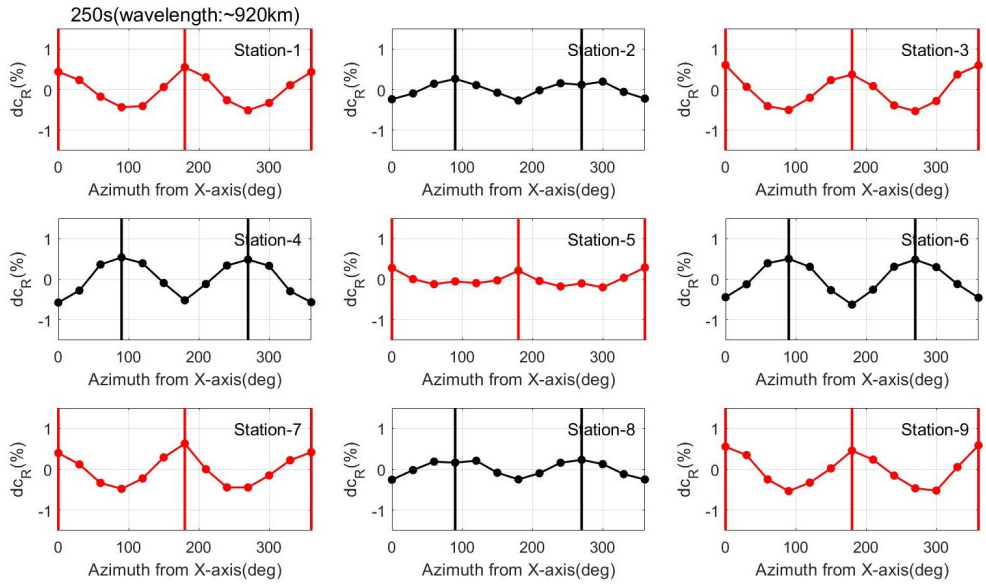

Figure 3.S12: Azimuthal anisotropy of Rayleigh wave of checkerboard model at 250s (wavelength is about 920km, anisotropic sub-model is 100km*100km in Figure S9) using the amplitude ratio Equation (1). The vertical solid lines (red and black) represent the theoretical fast directions. The fast directions are in agreement with the theoretical model.

Chapter 4

Seismic anisotropy from 6C ground motions of ambient seismic noise

by Le Tang, Heiner Igel, Jean-Paul Montagner and Frank Vernon
Published in Journal of Geophysical Research: Solid Earth (2024), 129(6), e2024JB028959.
https://doi.org/10.1029/2024JB028959

4.1 Key Points

• We show a new approach enabling the extraction of local phase velocity from 6C cross-correlation functions of ambient noise data.
• Azimuth-dependent 6C cross-correlation functions allow us to study local seismic anisotropy and its depth dependence.
• Local anisotropy at Piñon Flat Observatory is compatible with compression stress, providing constraints on stress-induced anisotropy.

4.2 Abstract

We propose a new approach capable of measuring local seismic anisotropy from 6C (three-component translation and three-component rotation) amplitude observations of ambient seismic noise data. Our recent theory demonstrates that the amplitude ratio of 6C cross-correlation functions (CCFs) enables retrieving the local phase velocity. This differs from conventional velocity extraction methods based on the travel time. Its local sensitivity kernel beneath the 6C seismometer allows us to study anisotropy from azimuth-dependent CCFs, avoiding path effects. Such point measurements have great potential in planetary exploration, ocean bottom observations, or volcanology. We apply this approach to a small seismic array at Piñon Flat Observatory (PFO) in southern California, array-deriving retrieves rotational ground motions from microseismic noise data. The

stress-induced anisotropy is well resolved and compatible with other tomography results, providing constraints on the origin of depth-dependent seismic anisotropy.

4.3 Plain Language Summary

In contrast to the well-known translational displacement of seismic waves, rotation measures the angle of rotation of a point in a medium as it deforms. Traditionally, the travel time of cross-correlation functions of translational displacement of ambient seismic noise and its corresponding propagation distance is used to calculate the velocity of the subsurface medium. However, our recent theory shows that the amplitude ratio of translational displacement and rotation allows us to reveal the local velocity of the medium beneath the receiver from ambient seismic noise data and to study anisotropy from earthquake events. This paper points out for the first time that the amplitude observations of 6C cross-correlation functions of ambient seismic noise provide a new approach to measure the azimuth-dependent velocity in anisotropic media.

4.4 Introduction

Rotational motion, as part of the wavefield gradient, can be measured directly by rotational seismometers at high frequencies (Lefevre, 2014; Bernauer et al., 2021; Zembaty et al., 2021) and in broadband ranges (Igel et al., 2007, 2021). Combining three-component translation and three-component rotation, a single 6C seismometer shows great potential in seismological observations, which can investigate the propagation direction of seismic waves (Yuan et al., 2021; Sollberger et al., 2018) and constrain the local Earth's velocity structure (Igel et al., 2007; Wassermann et al., 2016; Keil et al., 2021; Tang & Fang, 2021b; Fang & Tang, 2021; Tang & Fang, 2023; Tang et al., 2023a,c; Tang & Fang, 2023). The ambient seismic noise, as continuous sources on the Earth, has shown its powerful potential in studying Earth's structure based on conventional translation observations (Aki, 1957; Lobkis & Weaver, 2001; Shapiro et al., 2005; Haney et al., 2012). However, it has been an open scientific challenge whether rotational observations of ambient seismic noise can provide additional constraints for the Earth's interior. To investigate the potential of rotational observations of ambient seismic noise, only a few studies have conducted theoretical derivations and some preliminary observations. Hadziioannou et al. (2012) made the first attempt to extract the phase velocity of surface waves from ambient noise data by combining the translation and rotation observations. However, the overlap of ambient seismic noise destroys the assumption that the phase velocity extracted by the amplitude ratio is based on a single plane wave, resulting in larger uncertainty (Wassermann et al., 2016) in the phase velocity, making it difficult to monitoring small changes in velocities. Paitz et al. (2019) and Nakahara et al. (2021) carried out theoretical experiments of ambient noise interferometry to investigate the connections between Green's functions and cross-correlation functions or spatial auto-correlation (SPAC) coefficients of rotational ground

motions, but ignored the potential of the amplitude. Our recent theory paper focuses on the amplitude of SPAC coefficients of rotational ambient noise data (Tang & Fang, 2023), which indicates the feasibility of measuring the local phase velocity from amplitude ratios of 6C cross-correlation functions. This approach has a local sensitivity that differs from conventional velocity extraction methods based on travel time or phase difference whose sensitivity mainly distributes along the propagation path.

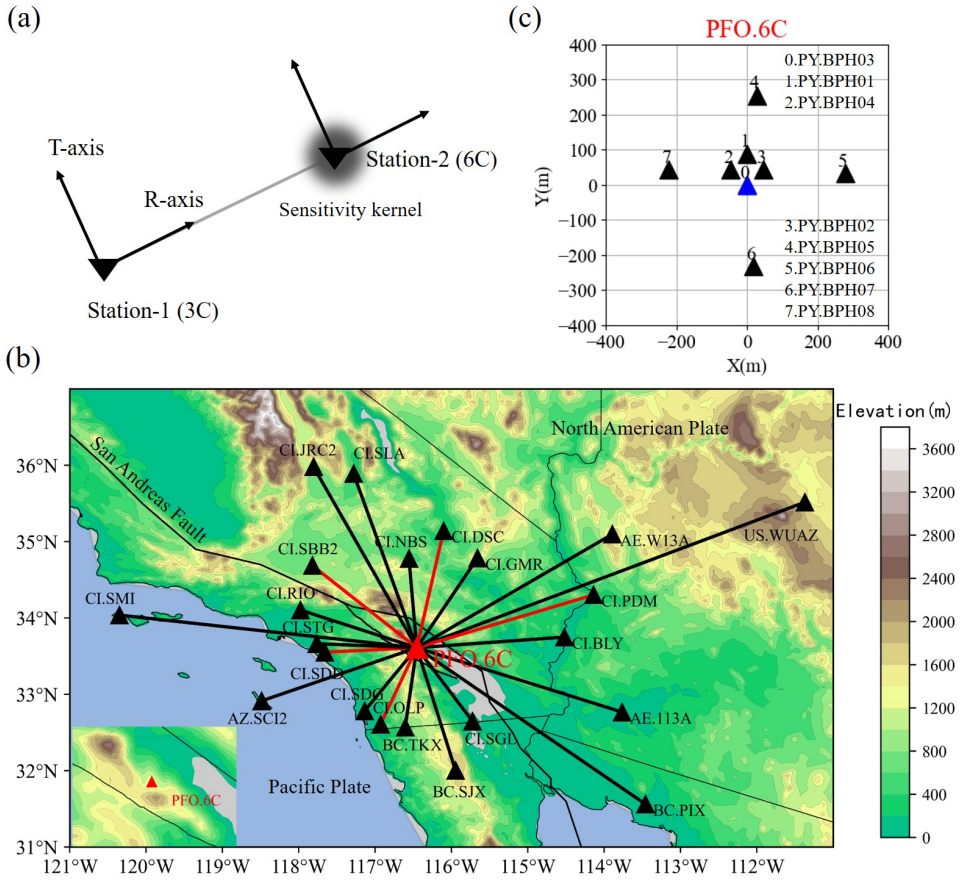

Figure 4.1: (a) Schematic diagram of a sensitivity kernel of the amplitude ratio method in Equations (4.1-4.3) from 6C CCFs of a pair of stations. Station-1 has three-component (3C) translational displacement. Station-2 has three-component translational displacement and three-component rotation (6C). (b) Distributions of broadband seismic stations. The black triangles represent 3C stations. The red triangle represents the 6C station of Piñon Flat Observatory (PFO) while the rotational waveform is retrieved from the ADR approach using a small seismic array of (c). (c) Reference PFO.6C array which is used to retrieve rotational motions from ambient noise data. At the blue station, the translational and rotational components are compared.

The local sensitivity allows us to monitor the velocity variation of the local structure without considering the path effects of the wave propagation (Tang & Fang, 2023). Study-

ing local seismic anisotropy (Pham et al., 2010; Tang & Fang, 2021a; Noe et al., 2022) from rotational ground motions can provide additional constraints on the tectonic evolution of the Earth (Tang et al., 2023a). The characteristics of rotational ground motions of surface waves in an anisotropic medium are well resolved in the recent study (Tang et al., 2023c) based on the first-order perturbation theory. It indicates that the azimuth-dependent surface wave dispersion curve can be directly obtained by using the amplitude ratio of translation to rotation or strain, which allows us to investigate the mantle flow and plate deformations (Tang et al., 2023a). Combining our recently proposed rotational ambient noise theory (Tang & Fang, 2023) and rotational anisotropy theory (Tang et al., 2023c), we can study local seismic anisotropy from azimuth-dependent 6C cross-correlation functions. Since permanent high-sensitivity broadband rotation seismometers do not yet exist, the array-derived rotation (ADR) method is well suited (Spudich et al., 1995; Spudich & Fletcher, 2008; Donner et al., 2017; Tang et al., 2023a) to retrieve the rotational waveform. However, the available period range is generally limited by the aperture of a seismic array, the uncertainty of instruments, and noise level. We select a small seismic array at the Piñon Flat Observatory in southern California to retrieve rotational ground motions and study local seismic anisotropy based on our new method for the first time. Ultimately, such 6C ambient noise data processing would be possible, if sufficiently sensitive sensors for all motion components would exist. This remains a technical challenge (Brotzer et al., 2023).

4.5 Methods

4.5.1 Velocity measurement from 6C CCFs

In isotropic media, the phase velocity of surface waves can be extracted from the amplitude ratio of 6C CCFs (Tang & Fang, 2023).

$$|\frac{C\dot{C}F_{(V_{z1},V_{z2})}}{CCF_{(V_{z1},\Omega_{t2})}}| = c_R \tag{4.1}$$

$$|\frac{C\dot{C}F_{(V_{r1},V_{z2})}}{CCF_{(V_{r1},\Omega_{t2})}}| = c_R \tag{4.2}$$

$$|\frac{C\dot{C}F_{(V_{t1},V_{t2})}}{2CCF_{(V_{t1},\Omega_{z2})}}| = c_L \tag{4.3}$$

where V_{z1}, V_{r1} and V_{t1} represent the three-component translational velocity of station-1 (see Figure 4.1a). V_{z2}, V_{t2}, Ω_{t2} and Ω_{z2} represent the two-component translational velocity and two-component rotational rate of station-2, respectively. CCF represents cross-correlation functions of a pair of stations and the $C\dot{C}F$ is the time derivative. c_R and c_L represent the phase velocity of the Rayleigh wave and Love wave, respectively. Equations (4.1-4.3) provide a new approach to measure the phase velocity from 6C CCFs of ambient seismic noise data, whose sensitivity kernel (gray zone in Figure 1a) is located beneath the 6C station (Tang & Fang, 2023; Fichtner & Igel, 2009; Tang et al., 2023a).

4.5.2 Azimuthal anisotropy from 6C observations

Our recent theory (Tang et al., 2023c) demonstrates that the amplitude ratio of acceleration to rotation rate or strain rate is equal to the theoretical azimuth-dependent phase velocity derived by Smith & Dahlen (1973). In this paper, we only consider the fundamental mode of Rayleigh waves. The dispersion equation of the Rayleigh wave from amplitude observations can be expressed as (Tang et al., 2023c):

$$|\frac{\dot{V}_z(\omega,\psi)}{\Omega_t(\omega,\psi)}| = c_0(\omega) + R_2(\omega)cos(2\psi) + R_3(\omega)sin(2\psi) + R_4(\omega)cos(4\psi) + R_5(\omega)sin(4\psi) \quad (4.4)$$

where $c_0(\omega) = c_{R0}(\omega) + R_1(\omega)$. $c_{R0}(\omega)$ is the phase velocity of the Rayleigh wave for the isotropic medium considered as a reference model. $\dot{V}_z(\omega,\psi)$ is the first-order time derivative of vertical translational velocity and $\Omega_t(\omega,\psi)$ is the transverse rotational velocity. ψ is the backazimuth of the wavenumber vector measured clockwise from the north direction. $R_i(\omega)$ $(i = 1, 2, 3, 4, 5)$ are respectively depth integration functions that involve some elastic parameters and eigenfunctions, where we used a simple integration expression derived by Montagner & Nataf (1986), whose explicit expressions can be found in Equations (2), (4), and (5) of Montagner & Nataf (1986). Equation 4.4 provides a new approach for estimating phase velocities in anisotropic media which only depends on amplitude information. Its local sensitivity kernel allows us to monitor the local velocity with high lateral resolution that can be several times smaller than one wavelength (Fichtner & Igel, 2009; Tang & Fang, 2023; Tang et al., 2023c,a). We replace the vertical velocity and transverse rotation velocity in Equation 4.4 with the corresponding CCFs in Equation 4.1, which allows us to study azimuthal anisotropy from ambient seismic noise data.

4.6 Data

The ambient noise data comes from the CI, AE, AZ, PY, BC, and US station networks, SCEDC (Southern California Seismic Network), and IRIS data center. We select 22 three-component stations distributed as evenly as possible around the 6C station (see Figure 4.1b) and use one-year ambient noise data from February 2015 to February 2016 to calculate cross-correlation functions and investigate the local azimuthal anisotropy. Figure 4.1b shows the geometry of seismic stations and the red triangle represents the 6C station where black triangles are the distributions of 3C stations. The distance between the PFO.6C station and the 3C station can be found in Figure 4.S1, which is from 112km to 512km. Considering that broadband rotational seismometers have not been permanently deployed widely, we select three-component broadband seismometers at Piñon Flat Observatory in southern California as the reference 6C array (see Figure 4.1c) to retrieve rotational ground motions using the ADR approach (Spudich et al., 1995; Spudich & Fletcher, 2008; Tang et al., 2023a) from ambient seismic noise data. The period range of wavefield gradients from the PFO.6C array (the aperture is about 500m) in Figure 4.1c is about 3-50s (Donner

et al., 2017) allowing the retrieval of rotational motions from two dominant microseismic noise data (5-10s: Secondary microseismic noise. 10-20s: Primary microseismic noise).

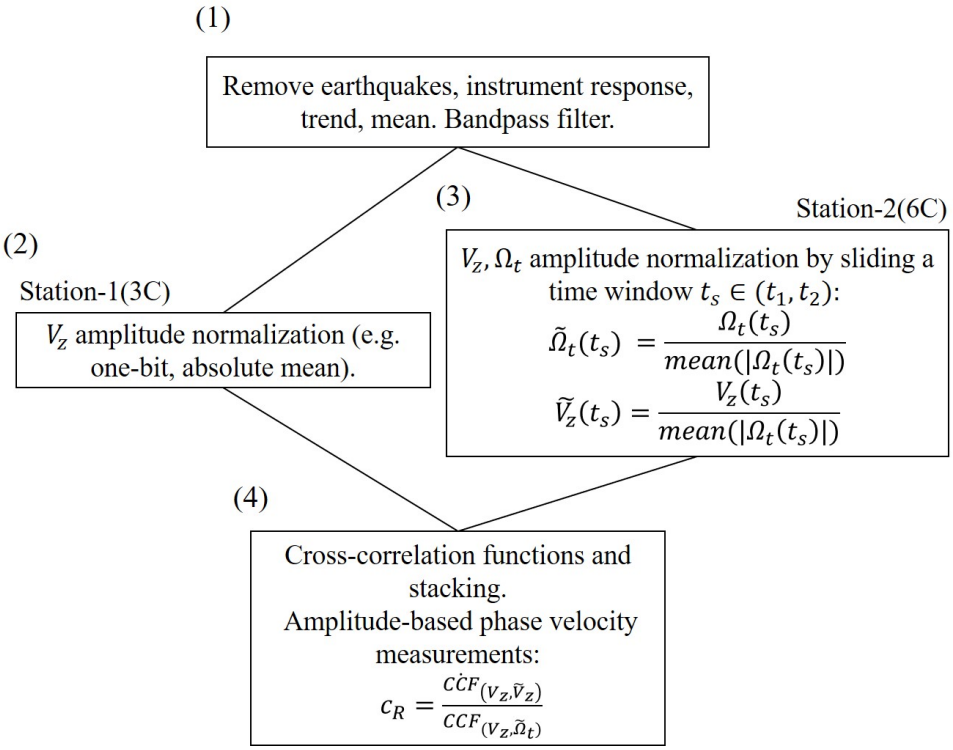

Figure 4.2: Schematic representation of the 6C ambient noise data processing scheme. (1): single-station preprocessing. (2): 3C station time-domain normalization. (3): 6C station time-domain normalization. (4): Calculate CCFs and phase velocity estimation.

The ambient noise data processing workflow of the 3C station and the 6C station are different. The 3C station can completely follow the processing steps summarized by Bensen et al. (2007). For simplicity, we perform one-bit normalization on the 3C stations. In contrast, the 6C station requires different amplitude normalization, whose processing workflow (see Figure 4.2) generally includes: (1) Remove instrument response, remove trend, remove mean, cut the data to a certain length (e.g. 1 hour or 1 day). We estimate the power-spectral-density (PSD) of the vertical acceleration at the PFO array using one-year data (see Figure 4.S2) which indicates that the corner period between secondary microseisms and primary microseisms is about 11.5s. We rounded and chose the 12s. At the period of 5-6s, this scattered signal is stronger at some azimuths (e.g. 120-180 degrees). Therefore, we filter the two dominant microseismic noise data of the PFO.6C station into two frequency ranges: 7-12s and 12-20s. (2) Amplitude normalization in the time domain: we perform absolute mean normalization to all components by running a time window (width: 5s). It must be emphasized that all components should be normalized by the same absolute mean (see Figure 4.2), where we calculate the absolute mean using rotational

components (e.g. Rayleigh wave: Ω_t and Love wave: Ω_z). (3) Calculate the CCFs and stacking. (4) Extract the phase velocity based on Equations (4.1-4.3). Among them, step (2) is to preserve the amplitude ratio information during data processing, because the phase velocity only comes from the contribution of the 6C station (Tang & Fang, 2023).

4.7 Results

4.7.1 Retrieval of 6C CCFs

Due to the high-quality waveform requirement of our approach, it is better to choose Equation 4.1 instead of Equation 4.2 to calculate the CCFs of Rayleigh waves, because V_z and Ω_t are only associated with Rayleigh waves in isotropic media and the coupling effect is very small and can be neglected for the fundamental mode in weakly anisotropic media (Tang et al., 2023c). In contrast, V_r also records ambient Love waves that will contaminate the waveform of Rayleigh waves and affect the signal-to-noise ratio (Tang et al., 2023c).

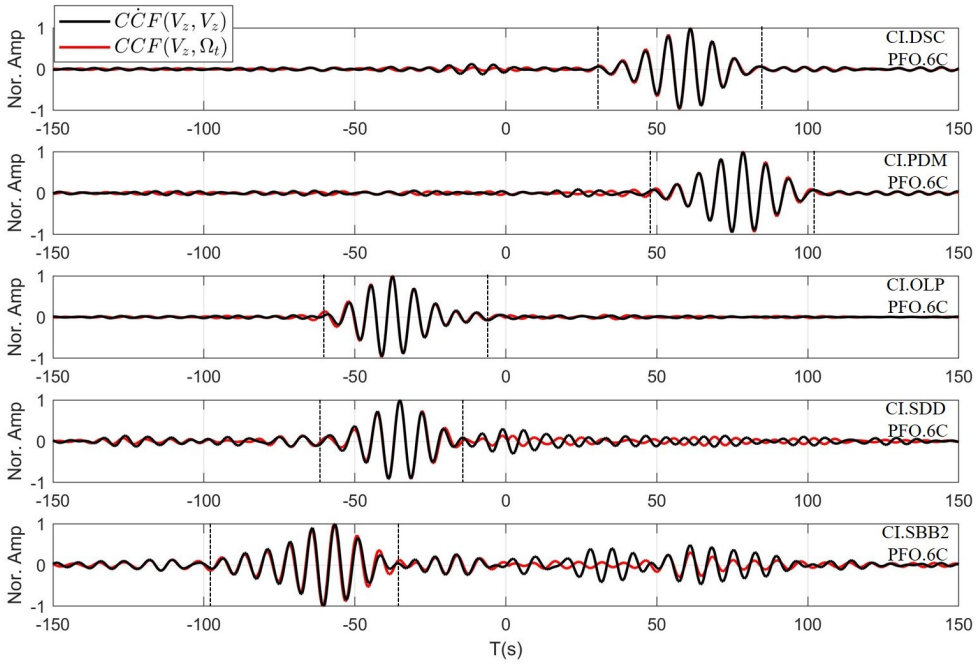

Figure 4.3: Rayleigh wave waveform (marked by black dashed lines) comparison (7s-12s) of CCFs calculated using one-year ambient noise data from five pairs of stations (CI.DSC, CI.PDM, CI.OLP, CI.SDD, CI.SBB2 and PFO.6C). The red lines represent CCFs between vertical translation of 3C station and transverse rotation of 6C station. The black lines represent CCFs between vertical translation of 3C station and vertical translation of 6C station. Red lines in Figure 4.1b represent their great circle paths.

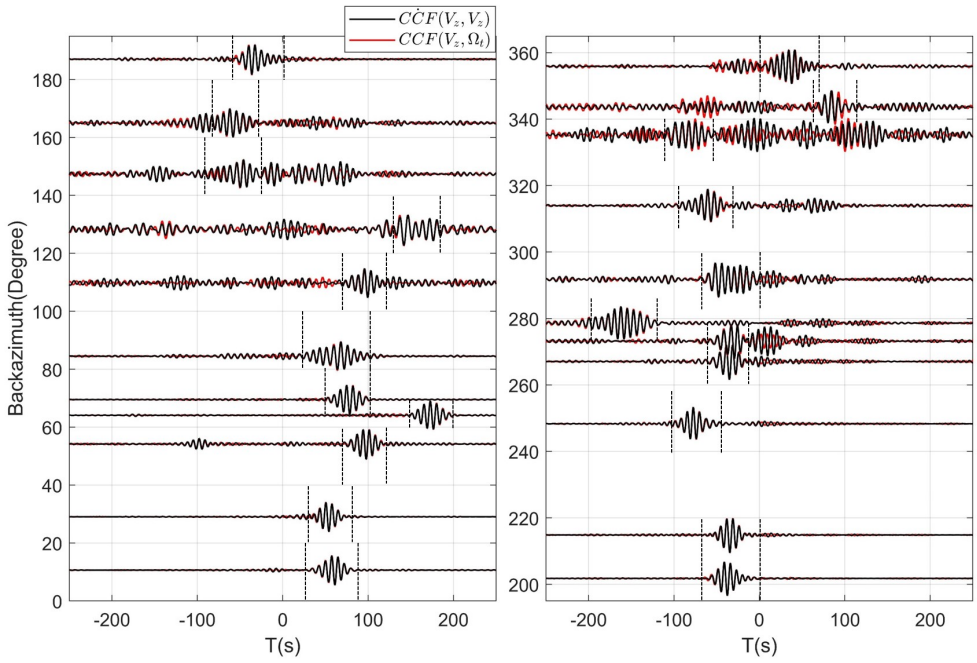

Figure 4.4: Normalized CCFs (marked by black dashed lines) of 7-12s in the azimuth domain based on Equation 4.1. The red lines represent CCFs between vertical translation of 3C station and transverse rotation of 6C station. The black lines represent CCFs between vertical translation of 3C station and vertical translation of 6C station.

Figure 4.3 shows the retrieved CCFs of Rayleigh waves of 7-12s using five pairs of stations (CI.DSC, CI.PDM, CI.OLP, CI.SDD, CI.SBB2, and PFO.6C station) at different azimuths based on Equation 4.1, in which red lines in Figure 4.1b represent their great circle paths. The 22 pairs of CCFs (see Figure 4.1b) in azimuth domains for two different frequency ranges are shown in Figure 4.4 (7-12s) and Figure 4.5 (12-20s). The very high correlation in the period range of 7-12s between translation-based CCFs and rotation-based CCFs (see Figure 4.3 and Figure 4.4) indicates the applicability of retrieved rotational waveform from the ADR approach, making it possible to extract the velocity from the amplitude ratio. However, in some azimuths, such as around 130-150 degrees and 340 degrees (see Figure 4.4), the noise interference of the cross-correlation function is strong, which is related to the distribution of secondary microseismic noise at 7-10s mainly coming from 180-270 degrees backazimuths (Schulte-Pelkum et al., 2004; Stehly et al., 2006). The distribution of primary microseismic noise at 12-20s is relatively complex, accompanied by strong seasonal variations (Stehly et al., 2006), resulting in low signal-to-noise ratios of CCFs and low correlation between translation-based CCFs and rotation-based CCFs (see Figure 4.5). The asymmetric CCFs of 7-12s in Figure 4.3 and Figure 4.4 indicate the inhomogeneity of the secondary microseismic noise, mainly originating in the direction of the Pacific Ocean (Stehly et al., 2006).

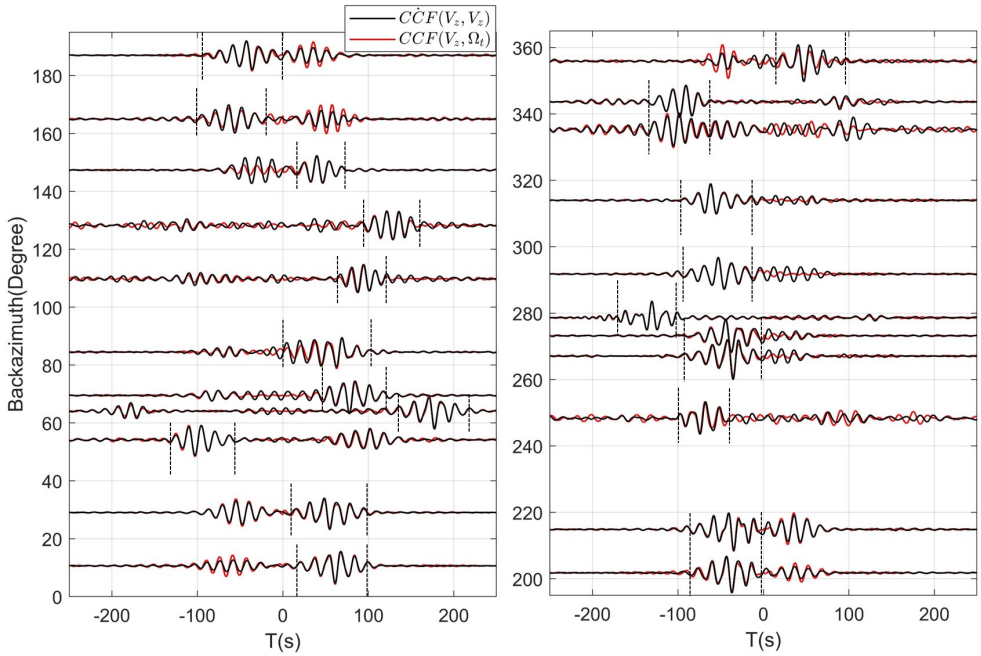

Figure 4.5: Normalized CCFs (marked by black dashed lines) of 12-20s in the azimuth domain based on Equation 4.1. The red lines represent CCFs between vertical translation of 3C station and transverse rotation of 6C station. The black lines represent CCFs between vertical translation of 3C station and vertical translation of 6C station.

From a theoretical point of view, the choice of positive or negative part of the cross-correlation function is necessary for estimating azimuth-dependent velocity, since the noise sources corresponding to these two parts come from the symmetry direction and the seismic velocity by the two parts should have symmetrical azimuths. For example, one is ψ degrees and the other is $\psi + \pi$ degrees. As illustrated in Figure 4.3 and Figure 4.4, the ambient noise of 7-12s mainly comes from one direction of the station pair. To have better azimuth coverage and to apply to most cases where the cross-correlation function of ambient seismic noise is asymmetric. Here, we simply use the azimuth of the station pair as the azimuth of extracted phase velocity. In principle, this operation will not affect the estimation of seismic anisotropic parameters from surface waves and this point is further elaborated in the Discussion section.

4.7.2 Velocity estimation and azimuthal anisotropy

As illustrated in Equations (4.1-4.3) and 4.4, amplitude ratios of CCFs enable extracting local phase velocity and allow us to study the local seismic anisotropy utilizing CCFs at different azimuths. We use the least-square method introduced by Tang et al. (2023c) to estimate the phase velocity of the Rayleigh wave using the waveform in Figure 4.4 and Figure 4.5 based on Equation 4.1. As shown in Figure 4.6, the calculated average phase velocity from 22 pairs of CCFs marked by a black solid line is compatible with the local

earth model (Shaw et al., 2015), but slightly faster especially at the primary microseisms frequency range (12-20s). Compared with the uncertainty (1σ) of 0.2km/s-0.3km/s at the period range of 7-12s, the period range of 13-20s shows a large uncertainty around 0.3km/s-0.6km/s, which not only indicates the velocity anisotropy but is also mainly contaminated by waveform errors related to complex ambient noise distributions (see the Discussion section), leading to the low waveform correlation and low signal-to-noise ratio (see Figure 4.5). Therefore, we only focus on the period range of 7-12s for our anisotropy study.

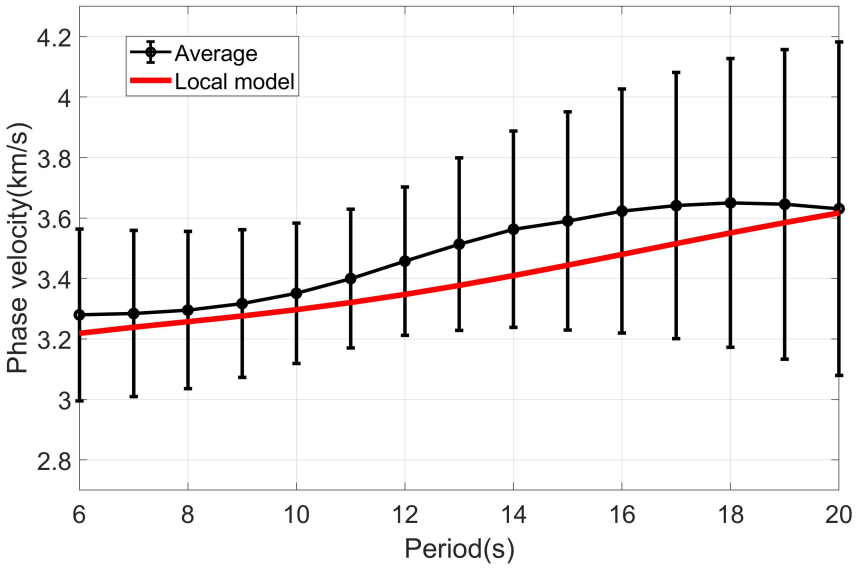

Figure 4.6: Velocity comparison between estimated phase velocity of Rayleigh waves at 6-20s from 22 pairs of CCFs and local velocity model (red line) near the PFO region (Shaw et al., 2015)

.

Because the ADR method is a gradient calculation based on differential methods (Spudich et al., 1995; Spudich & Fletcher, 2008; Donner et al., 2017), which indicates that the period range is limited by the aperture of the seismic array and the noise level of instruments. In addition, the strong wavelength-scale heterogeneity beneath the array will destroy the homogeneity assumption on which the ADR method is based, and the inhomogeneity of the station geometric distribution will also affect the phase and amplitude of the retrieved rotational waveform. Therefore, quantifying the uncertainty in wavefield gradients while taking these factors into account has been a great challenge. Currently we do not know how to consider these factors simultaneously because the effect of real subsurface heterogeneous structures on waveform gradients is not known. Alternatively, we average the velocity estimates in 60-degree azimuth bins and calculate the uncertainty within the selected azimuth bins. The method to calculate uncertainty is detailed in the supporting material (see supporting materials for uncertainty estimation). The error for

the anisotropy strength and fast directions can be obtained using an error propagation technique (Cliford, 1973).

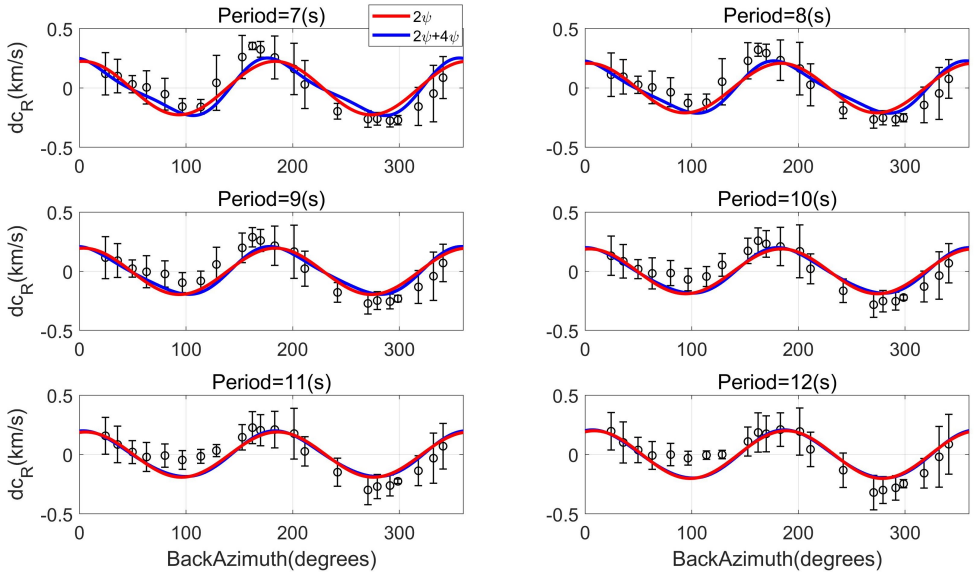

Figure 4.7: Velocity variation of 7-12s of Rayleigh waves in the azimuth domain. Red lines are the best-fit 2ψ curves and blue lines are the best-fit curves when 2ψ and 4ψ terms are included in Equation 4.4.

Figure 4.7 shows the measured phase velocity variation using one-year (2015.02-2016.02) ambient noise data at 6 periods where the isotropic term $c_0(\omega)$ in Equation 4.4 is subtracted. The red and blue curves in Figure 4.7 are the best-fit curves for 2ψ and $2\psi + 4\psi$ terms of Equation 4.4, respectively. It can be seen that the estimated phase velocity matches with the 2ψ and $2\psi+4\psi$ anisotropy term and the difference between the two curves is very small. From a theoretical point of view, the 4ψ anisotropy term for Rayleigh waves is quite small as demonstrated by Montagner & Nataf (1986) and can be neglected in many anisotropy observations. In our study, we only analyze the 2ψ term because the non-homogeneity of noise sources (Stehly et al., 2006) makes it difficult to resolve the 4ψ term.

Even though the secondary microseismic noise (5-10s) in southern California does not show seasonal variations (Stehly et al., 2006) in the phase, it is still necessary to investigate the effect of seasonal noise distributions on velocity measurements, as the amplitude change is visible (Stehly et al., 2006) with a different signal-to-noise ratio probably leading to considerable velocity errors. As indicated in Figure 4.8a, the peak-to-peak anisotropy fluctuates between around 4%-7% over one year, whose difference in anisotropy between spring-summer and autumn-winter (see Figure 4.S3 for seasonal velocity variations in the backazimuth domain) is probably due to slight changes in the distribution of noise sources. However, the estimated fast axis direction of 2ψ term in Figure 4.8b is relatively stable within a year. The fast axis direction of 7s mainly points to the north-south direction (0-10 degrees), the 10s fluctuate in the backazimuth of 5-15 degrees, and the 12s fluctuate in the

backazimuth of 10-20 degrees. As indicated in Figure 4.8b, the fast axis seems to show a transition from north-south to northeast-southwest direction throughout the year.

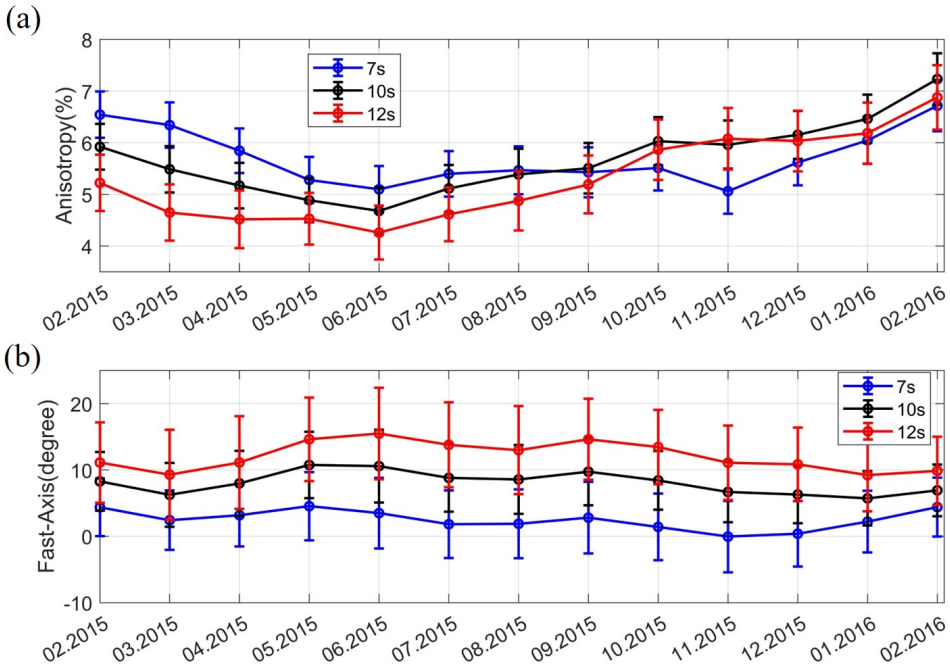

Figure 4.8: Seasonal variation of anisotropy and fast axis with sliding window of two months. (a) Seasonal variation of peak-to-peak anisotropy of the 2ψ term at 7s (blue lines), 10s (black lines) and 12s (red lines). (b) Seasonal variation of fast-axis of the 2ψ term at 7s (blue lines), 10s (black lines) and 12s (red lines).

4.8 Discussion

4.8.1 Stability of velocity measurement based on 6C CCFs

It is very dangerous to use the waveforms of a single earthquake event to estimate the velocity from 6C amplitude ratios, since a small disturbance, probably from the uncertainty of instruments or random noise, on the waveform will have a considerable impact on the amplitude ratio (Kurrle et al., 2010). Therefore, waveform stacking of a large number of events is required to obtain a reliable result (Tang et al., 2023c,a). The interaction between ocean waves and the Earth produces a continuous source of seismic noise, providing the feasibility of using amplitude ratios to obtain reliable velocity solutions. To investigate the robustness of the proposed approach based on amplitude observations, we calculate three variables (see Figure 4.9): (1) signal-to-noise ratio (SNR) (see Figure 4.S4 for the SNR estimation), (2) correlation coefficients between translation-based CCFs and rotation-based CCFs, and (3) relative velocity variation of one pair of stations (CI.PDM and PFO.6C

in Figure 4.1b with 69.4 degrees backazimth) to evaluate how they change during one-year ambient noise data.

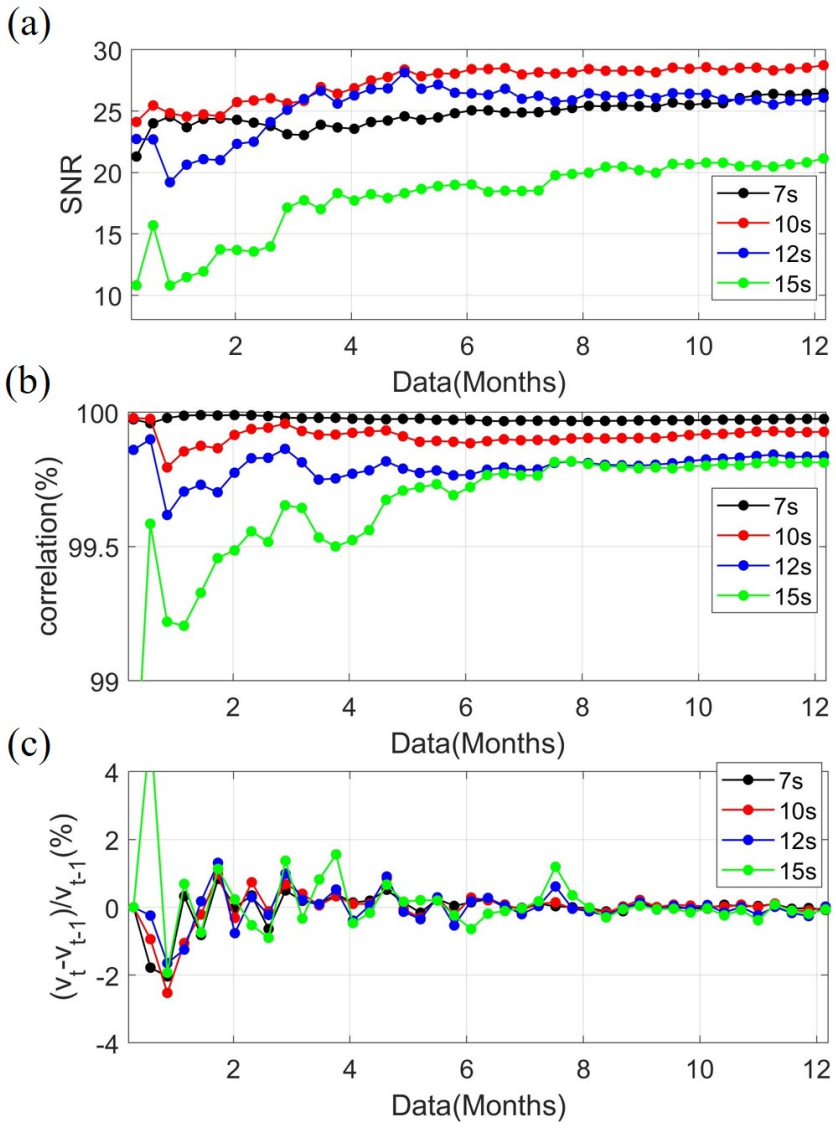

Figure 4.9: Stability of CCFs between CI.PDM station and PFO.6C station. (a) Signal-to-noise ratio (SNR) of $C\dot{C}F_{(V_{z1},V_{z2})}$ at four periods (7s, 10s, 12s, and 15s) using different data volume. (b) Correlation coefficients between $C\dot{C}F_{(V_{z1},V_{z2})}$ and $CCF_{(V_{z1},\Omega_{t2})}$ at four periods (7s, 10s, 12s, and 15s) using different data volume. (c) Relative velocity variation $(c_T - c_{T-1})/c_{T-1}$ at four periods (7s, 10s, 12s, and 15s) using different data volume.

With the continuous stacking of ambient noise data, the SNR of CCFs increases to about 20-30 in one year (see Figure 4.9a) while the SNR of 7s, 10s, and 12s is higher than that of 15s because of the higher energy of the secondary microseism noise compared with the primary microseism noise. However, it can be seen that even if the correlation between

the rotation-based CCFs and the translation-based CCFs has reached more than 99% (see Figure 4.9b), the extracted phase velocity of the first month by the amplitude ratio still fluctuates in a large range as shown in Figure 4.9c. It indicates that the cross-correlation coefficient can not be completely relied on as the only criterion for judging and selecting high-quality waveform, which is only one important indicator for evaluating waveform. The obvious improvement of the SNR and the gradual convergence of the corresponding phase velocity after more data stacking (see Figures 4.9a and 4.9c) imply the necessity of higher SNR for amplitude-based velocity measurements. After about three months of data stacking, the relative change in velocity gradually decreases (see Figure 4.9c), and the phase velocity converges to a stable value, especially for 7-12s, indicating the feasibility of obtaining a stable and reliable phase velocity through the amplitude ratio of CCFs after several months ambient noise stacking.

It should be noted that the stable solution of the analyzed station pair only indicates that a stable solution can be obtained on the premise of obtaining CCFs with a high SNR, and it is also applicable to long periods (such as 15s in Figure 4.9). Due to the uneven distribution of ambient noise and seasonal changes, especially the primary microseismic noise in southern California (Stehly et al., 2006), the observation of velocity at 13-20s is not stable at all azimuths, which is not conducive to the study of anisotropy.

4.8.2 Effect of noise distribution and coupled waves

The effect of ambient noise distribution on the velocity extraction using the amplitude ratio of CCFs can be divided into two cases. In the first case, noise sources are mainly distributed in the stationary zone on one side of the pair of stations (see Figure 4.10b). The phase velocity in the symmetrical azimuth of the noise source can not be obtained. For example, in Figure 4.10b, we can only calculate the phase velocity in the 270 degree direction. The 90 degree direction is unknown unless the noise source is distributed this direction (see Figures 4.10a). This is the key difference from travel time-based tomography methods. Considering the particularity of the non-uniform distribution of noise sources in southern California region (Figures 4.3 and 4.4) and the limitations of single point observation, it is difficult to resolve the relatively complex anisotropic media such as the 4ψ anisotropic term, while the consideration of the 2ψ term is reasonable. To obtain better azimuthal coverage, we simply take the azimuth of the station pair as the azimuth of the extracted phase velocity in Figure 4.7 (see Figures 4.S5 and 4.S6 for velocity anisotropy after considering the real noise source direction). Because under the assumption of the first-order perturbation, the Rayleigh wave is only sensitive to monoclinic media (Montagner & Nataf, 1986; Tang et al., 2023c) (in general anisotropic media, the 21 elastic parameters of anisotropic media will degenerate to 13 elastic parameters), the phase velocities at the azimuths of ψ and $\psi+\pi$ are equal (see Figure 4.10a). Consequently, there is no need to distinguish the CCFs on both sides when estimating the Rayleigh wave velocity, and theoretically it will not affect the measurement of anisotropy parameters. In another case, the noise source is not distributed in the stationary zone (Campillo et al., 2011), which implies that the calculated CCFs are biased in terms of travel time between the two stations. In contrast, the amplitude can

be corrected to calculate the local phase velocity, and $CCF_{(V_z,\Omega_t)}$ in Equation 4.1 can be replaced by $\sqrt{CCF^2_{(V_z,\Omega_t))} + CCF^2_{(V_z,\Omega_r))}}$ after rotating the two components $CCF_{(V_z,\Omega_t)}$ and $CCF_{(V_z,\Omega_r)}$ into the direction of the maximum amplitude which is similar to the ORA (optimal rotation algorithm) (Roux, 2009). Where the horizontal rotational components Ω_t and Ω_r are dominated by Rayleigh waves (Tang et al., 2023c).

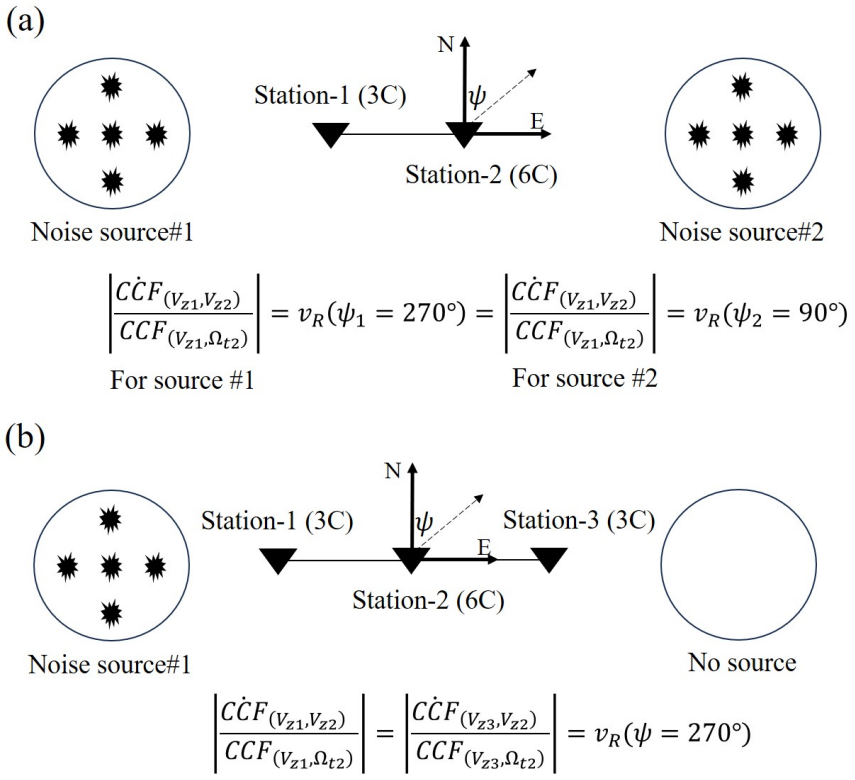

Figure 4.10: (a) The estimated velocity using the negative and positive parts (sources 1 and 2 respectively) of CCFs of one pair of stations will have opposite backazimuth (ψ and $\psi + \pi$), but the Rayleigh wave has the same velocity. (b) The estimated velocity from the CCFs of two pairs of stations in parallel from the same noise source will show the same phase velocity.

Figure 4.11 shows the synthetic verification of correcting the source azimuth deviation. As indicated in Figure 4.11a, the noise source is evenly distributed in azimuth and is approximately 1000km away from two stations (black triangle), with a distance of 100km between the two stations. Due to the deviation of the noise source, there is a significant difference in the travel time of CCFs (see Figure 4.11b), making it impossible to extract the velocity between the two stations based on travel time. Similarly, the estimated velocity using Equation 4.1 is not reliable (black line in Figure 4.11c). However, azimuth correction using horizontal rotation components $\sqrt{CCF^2_{(V_z,\Omega_t))} + CCF^2_{(V_z,\Omega_r))}}$ allows us to obtain the accurate velocity (blue line in Figure 4.11c).

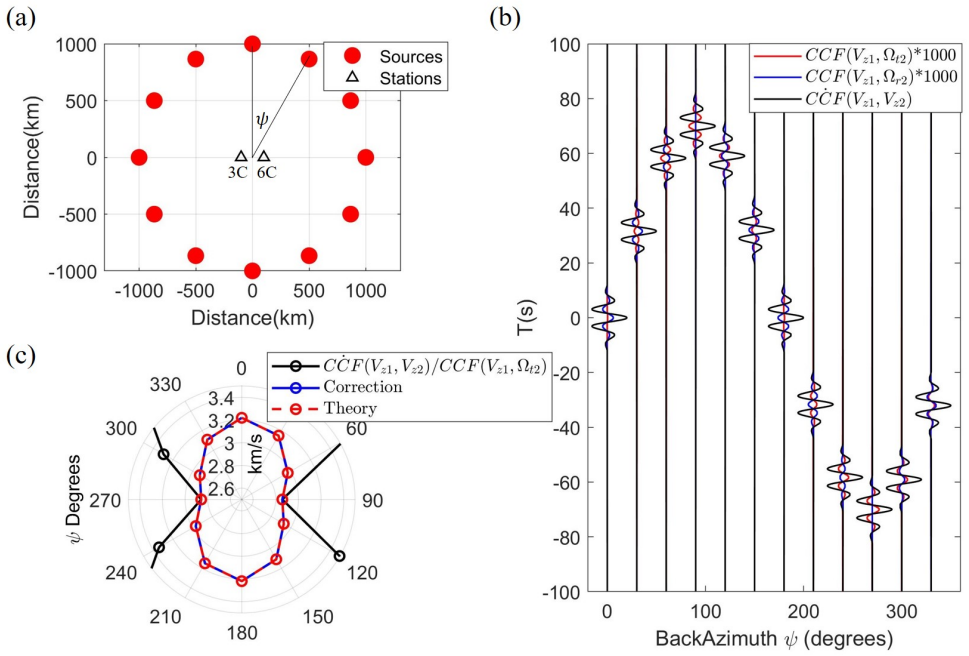

Figure 4.11: (a) Distributions of seismic sources (vertical force source) and a pair of stations for investigating the effect of noise source in the non-stationary zone. The analytical phase velocity of Rayleigh waves is $V_R = 3.258 + 0.194 * cos(2\psi) + 0.025 * sin(2\psi)$. (b) Synthetic CCFs in (a) after normalizing the amplitude of $C\dot{C}F_{(V_{z1},V_{z2})}$. (c) Velocity estimation using CCFs of (b). The black line represents the results from Equation (1) which show large error compared with the analytical solution marked by red points. The blue line represents the corrected results of replacing $CCF_{(V_{z1},\Omega_{t2})}$ with $\sqrt{CCF^2_{(V_z1,\Omega_t2))} + CCF^2_{(V_z1,\Omega_r2))}}$.

Considering the coupling effect of Rayleigh waves and Love waves in anisotropic media, coupled waves with small amplitudes will be generated on other components of CCFs (Saade et al., 2015). As illustrated in Figure 4.12, the small amplitude on the $CCF_{(V_z,\Omega_z)}$ probably indicates the coupled wave if the influence of 3D heterogeneous scattering is excluded, since V_z and Ω_z only correspond to Rayleigh waves and Love waves in isotropic media, respectively. Consequently, the small amplitude on $CCF_{(V_z,\Omega_r)}$ (see Figure 4.12) is the result of a combination of noise source deviation and coupling effects, which indicates that one should be careful to do the noise source correction especially when the azimuth deviation is quite small. Because it is difficult to quantitatively separate the magnitude of the two small amplitudes, further study is needed in the future. As indicated in Figure 4.S7, in most azimuths (0-100 degrees, 180-260 degrees), the angle deviation ($tan\psi = CCF_{(V_z,\Omega_r)}/CCF_{(V_z,\Omega_t)}$) of the noise source is about 10 degrees, which is quite small. Therefore, the estimated phase velocities in Figure 4.6 and Figure 4.7 are obtained without the small azimuth correction. However, the velocity extracted at these azimuths of 130-180 degrees and 270-360 degrees has been corrected because it shows a larger angle deviation (see Figure 4.S7), but its low signal-to-noise and scattered waves lead to larger

uncertainty (see Figure 4.7). Although the azimuth of the noise source at 7-12s can be corrected using the method, the strong seasonal noise variation makes it difficult to obtain a stable solution in the long period range. Therefore, further study is needed for the localization and correction of ambient noise sources, such that the 6C-based cross-correlation technology can be extended to longer period ranges in the future.

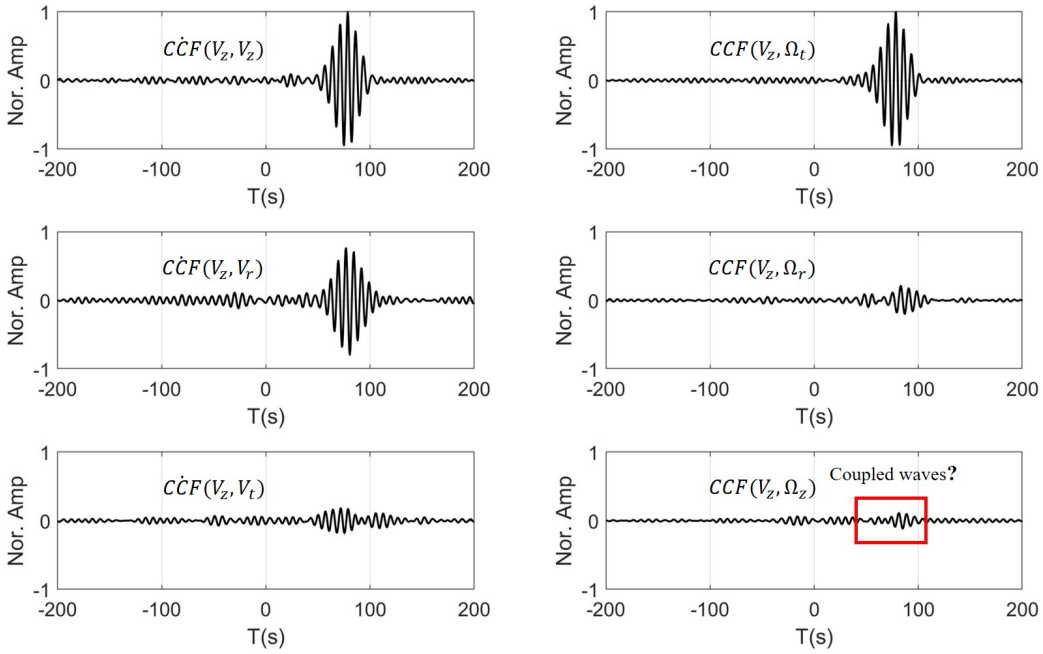

Figure 4.12: CCFs (7-12s) between vertical translation of the CI.PDM station and six-components of the PFO.6C station using one-year ambient noise data. The left three components $C\dot{C}F_{(V_z,V_z)}$, $C\dot{C}F_{(V_z,V_r)}$ and $C\dot{C}F_{(V_z,V_t)}$ are normalized by $C\dot{C}F_{(V_z,V_z)}$ which are only associated with translation. The right three components $CCF_{(V_z,\Omega_t)}$, $CCF_{(V_z,\Omega_r)}$ and $CCF_{(V_z,\Omega_z)}$ are normalized by $CCF_{(V_z,\Omega_t)}$ which are associated with rotation.

4.8.3 Stress-induced anisotropy from 6C measurements

The lateral resolution of the conventional methods of anisotropy study in southern California is limited by the aperture of stations, wavelength, and strong heterogeneity. In contrast, the unique local sensitivity kernel of our approach allows us to image the local structure and to study local anisotropy (Tang et al., 2023c,a). Here, we estimate the corresponding depth range based on Rayleigh's sensitivity kernel of the local velocity model (Shaw et al., 2015) at 7s, 10s, 12s, and 15s (see Figure 4.S8), indicating that the anisotropy at periods of 7-12s in Figure 4.7 are most sensitive to the upper 5-15km of the crust. We compare it with other anisotropy results estimated from different methods that have a lateral local sensitivity kernel. The anisotropy strengths measured near the San Andreas Fault indicate that borehole measurements show around 10% anisotropy in the near surface (Aster & Shearer, 1991; Boness & Zoback, 2004), and shear-wave splitting results indicate that

the crustal anisotropy is between 8% and 15% (Boness & Zoback, 2006), demonstrating the considerable 4%-7% anisotropy shown in Figure 4.8. The derived direction of the fast axis (red line in Figure 4.13) at 7s sensitive to the upper 5-15km of the crust (see Figure S8) is consistent with the maximum horizontal compression stress (orange lines in Figure 4.13) (Heidbach et al., 2010) and in agreement with the results of shear-wave splitting in the upper 20km of the crust (yellow line in Figure 4.13) (Yang et al., 2011) at the PFO station. Its anisotropy is generally interpreted by preferentially aligned cracks or SPO (shape-preferred orientation) that are associated with the stress field (Aster & Shearer, 1991; Boness & Zoback, 2004, 2006; Yang et al., 2011; Wu et al., 2022).

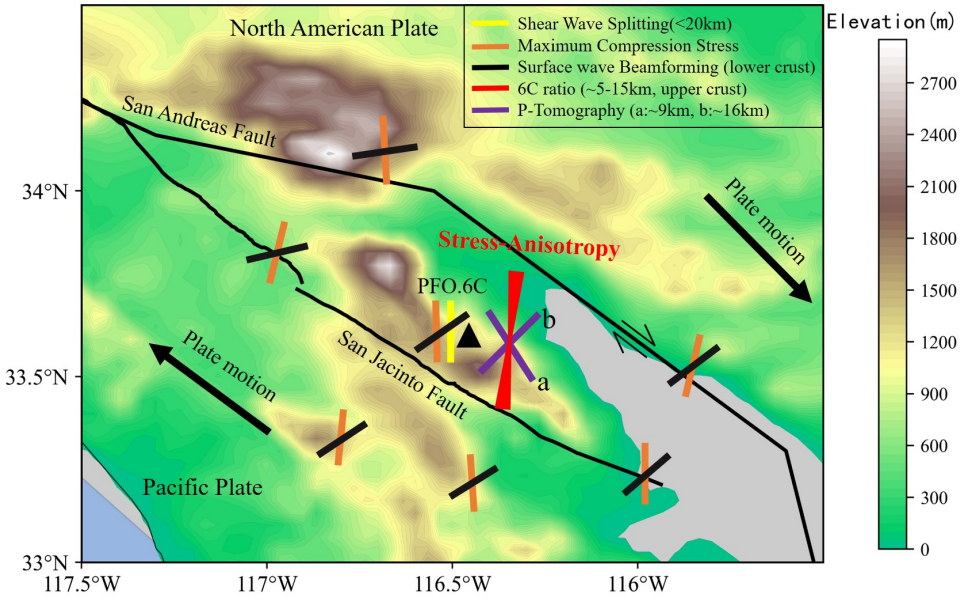

Figure 4.13: Stress-induced anisotropy revealed from 6C observations. The red line shows the fast-axis of Rayleigh waves in the upper crust associated with the stress-induced anisotropy. The orange lines represent the maximum compression stress directions near the PFO array, which are determined from borehole breakouts, hydraulic fracturing experiments, and earthquake focal mechaism inversions (Heidbach et al., 2010). The yellow line represents the fast-axis direction of shear-wave splitting at PFO using local events, which is sensitive to upper crustal structure (<20km) (Yang et al., 2011). The black lines represent the fast-axis directions of surface waves using the beamforming tomography method (Tanimoto & Prindle, 2007). The purple line-a and line-b represent the fast-axis directions of P waves at around 9km and 16km, respectively, using the P wave tomography method (Wu et al., 2022). The black arrows show the plate motion directions (Tang et al., 2023a).

In the depth direction, the fast axis shifts from the north-south direction of the upper crust (7s in Figure 4.8) to the northeast-southwest direction of the middle crust (12s in Figure 4.8), which is probably due to the onset of the transition from stress-induced anisotropy to structure-induced anisotropy if we can exclude the uncertainty effect in the

future. Because the fast axis in the lower crust by the beamforming tomography result of Rayleigh waves mainly points towards the northeast-southwest direction (Tanimoto & Prindle, 2007), approximately between 40 and 60 degrees (black lines in Figure 4.13). This anisotropy is generally caused by the crystallographic preferred orientation (CPO) of anisotropic minerals formed during rock formation and subsequent deformation (e.g. (Alvizuri & Tanimoto, 2011; Tanimoto & Prindle, 2007; Wu et al., 2022) for southern California).

4.9 Conclusion

We propose a new method based on the 6C ambient noise data for investigating the local seismic anisotropy. The local seismic anisotropy at Piñon Flat Observatory in southern California in the period range of secondary microseismic noise is resolved, showing stress-induced seismic anisotropy with small azimuth variations at different depths, providing new insight into the origin of depth-dependent anisotropy. Sufficient ambient seismic noise data and the effective ADR technique enable wide and quick applicability in various seismological studies. We expect the rapid development of high-quality broadband 6C rotational seismometers, which are capable of retrieving rotational waveform based on a single 6C station. Our approach would be particularly useful whenever large seismic arrays are not affordable or difficult to implement (e.g. planetary exploration, ocean bottom observations, volcanology, or urban seismology).

4.10 Acknowledgments

We are grateful to Michel Campillo (ISTerre, Grenoble) and Eleonore Stutzmann (IPGP, Paris) for constructive discussions. This work is funded by the European Union's Horizon 2020 research and innovation program under the Marie Skłodowska-Curie grant agreement No 955515 (ITN SPIN). HI is grateful for a scholarship by the Cecil and Ida Green Foundation funding his visits to the Institute of Geophysics and Planetary Physics in La Jolla, California in 2022 and 2023.

4.11 Open Research

The ambient noise data is publicly available and accessed from CI network (California Institute of Technology and United States Geological Survey Pasadena, 1926), AE network (Arizona Geological Survey, 2007), AZ network (Frank Vernon, 1982), PY network (Frank Vernon, 2014), BC network (Centro de Investigación Científica y de Educación Superior de Ensenada (CICESE), Ensenada, 1980), and US station network (Albuquerque Seismological Laboratory (ASL)/USGS, 1990). The shear-wave splitting direction is available from Yang et al. (2011). Maximum compression stress data is available from Heidbach et al. (2010). Fast-axis directions using the surface wave beamforming method are available from

Tanimoto & Prindle (2007). Fast-axis directions of P wave tomography are available from Wu et al. (2022). The plate motion directions are available from **?**. The local velocity model at the PFO array can available from Shaw et al. (2015). The array-derived rotation (ADR) code is available from tangle0129 (2023).

4.12 Appendix: Supplementary materials

Contents of this file
Text 4.S1
Figures 4.S1 to 4.S8

4.12.1 Supplementary text

Uncertainty estimation
We average the velocity estimates in 60-degree azimuth bins and calculate the uncertainty within the selected azimuth bins.

$$\sigma_d = \sqrt{\frac{\sum_{i=1}^{N}(d_i - \overline{d})^2}{N}} \tag{4.S1}$$

where σ_d is the estimated standard error of the phase velocity, N is the number of observations in the 60-degree azimuth bins. Writing the five unknowns (c_0, R_2, R_3, R_4, R_5 in Equation 4.4) in a vector X, we can write the original equation to be satisfied as $D = AX$, where A is formed from the azimuth of the i-th data and D is comprised by measured phase velocity for the i-th datum. The well-known least squares solution to this problem is $X = (A_T A)^{-1} A^T D$. Then we can obtain the uncertainty of other parameters using the following equations.

$$C_p = (A^T A)^{-1} A^T C_d A (A^T A)^{-1} \tag{4.S2}$$

Where C_d is the data covariance matrix. The peak-to-peak anisotropy is $\sqrt{R_2^2 + R_3^2}/c_0$ and the fast direction is $\arctan(R_3/R_2)/2$ and standard errors for the strength and fast direction can be calculated from the variation of c_0, R_2 and R_3 using an error propagation technique (Cliford, 1973).

4.12.2 Supplementary figures

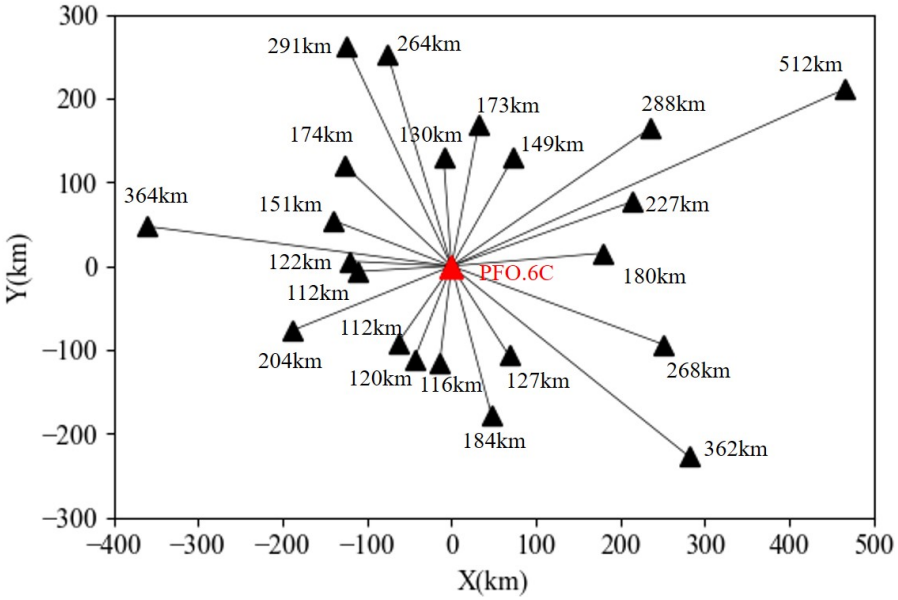

Figure 4.S1: Distributions of selected broadband seismic stations. The red triangle represents the 6C station and the black triangles represent the 3C stations.

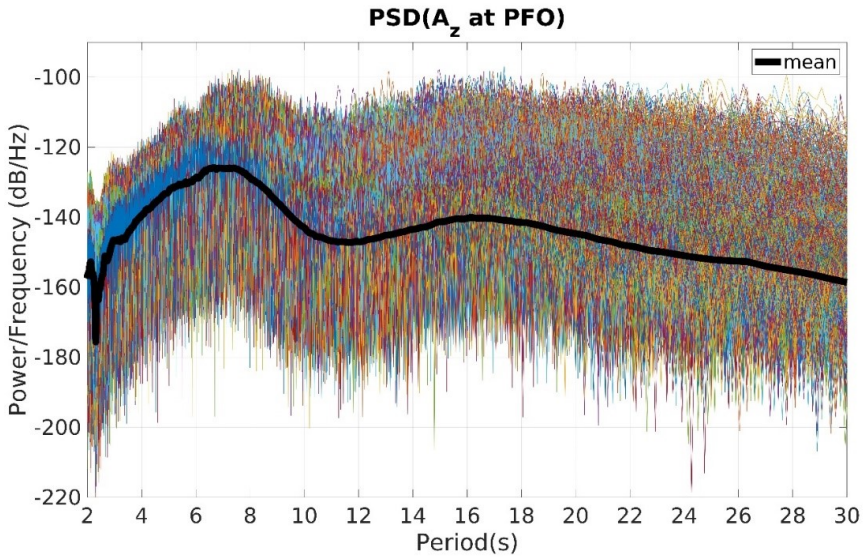

Figure 4.S2: Power spectral density of vertical acceleration A_z (PY.BPH03.BHZ) at PFO array in 2015.

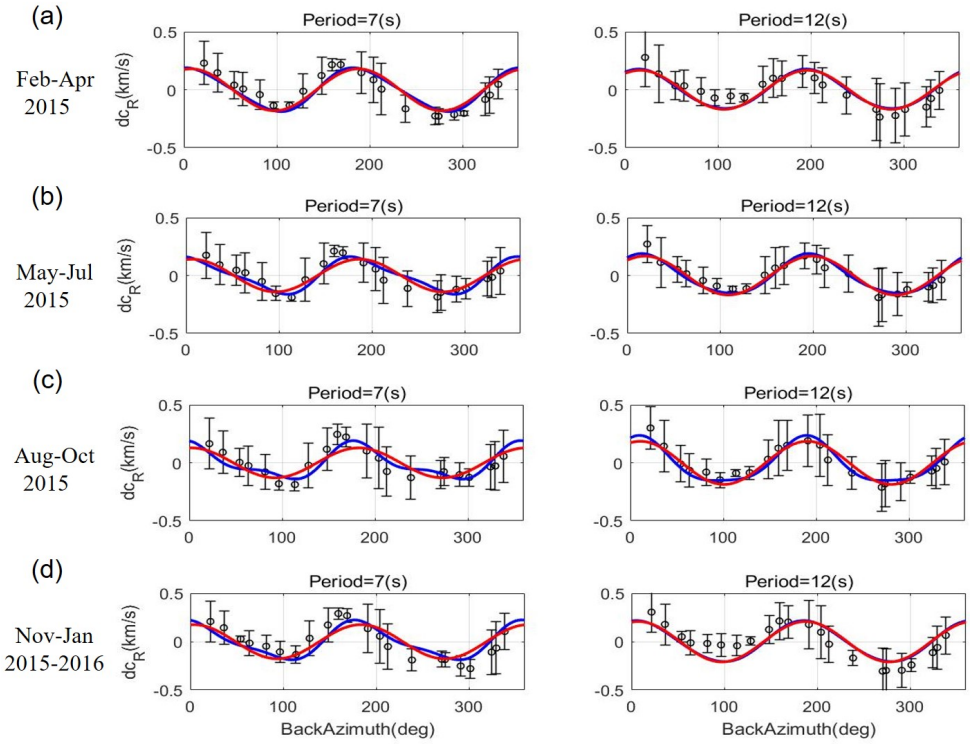

Figure 4.S3: Seasonal velocity variation (a: Spring, b: Summer, c: Autumn, d: Winter) at 7s and 12s. Red lines are the best-fit 2ψ curves and blue lines are the best-fit 2ψ and 4ψ.

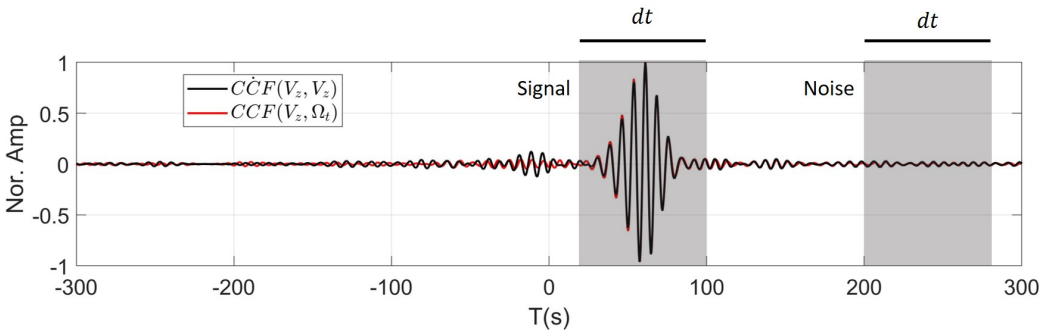

Figure 4.S4: Signal-to-noise ratio (SNR): computing the ratio of its summed squared magnitude (signal window) to that of the noise (noise window).

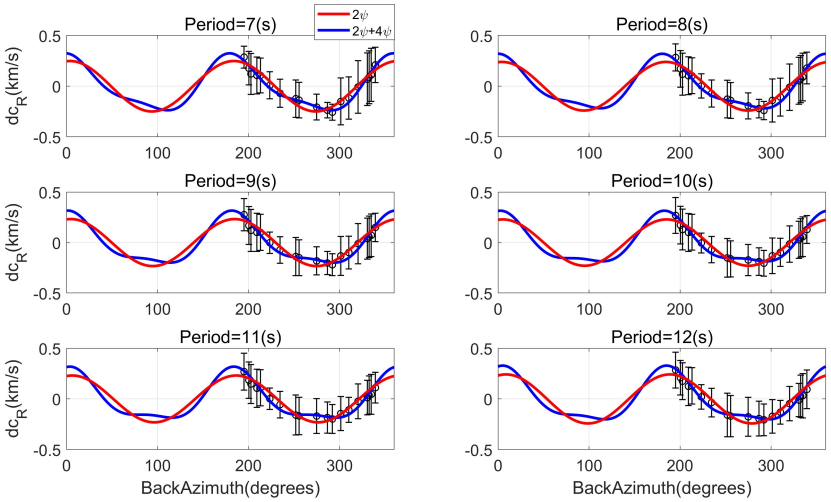

Figure 4.S5: Velocity variation of Rayleigh waves in 7-12s using one-year data after considering the real noise source direction. Red lines are the best-fit 2ψ curves and blue lines are the best-fit curves when 2ψ and 4ψ terms are included in Equation 4.4.

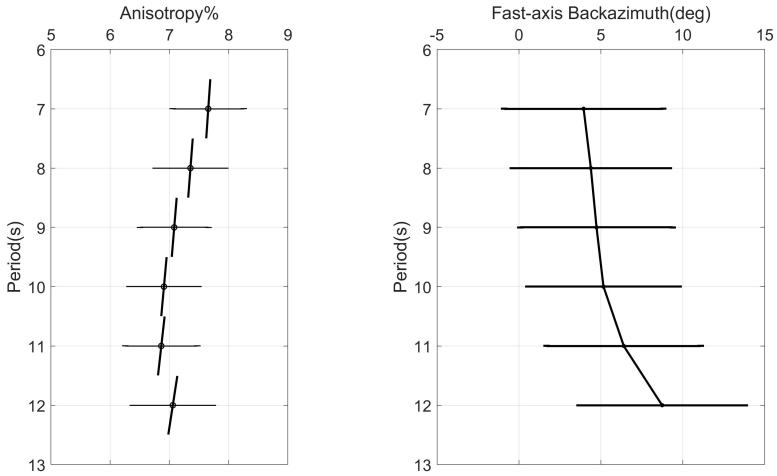

Figure 4.S6: Peak-to-peak anisotropy and fast-axis direction of Rayleigh waves in 7-12s using one-year data after considering the real noise source direction.

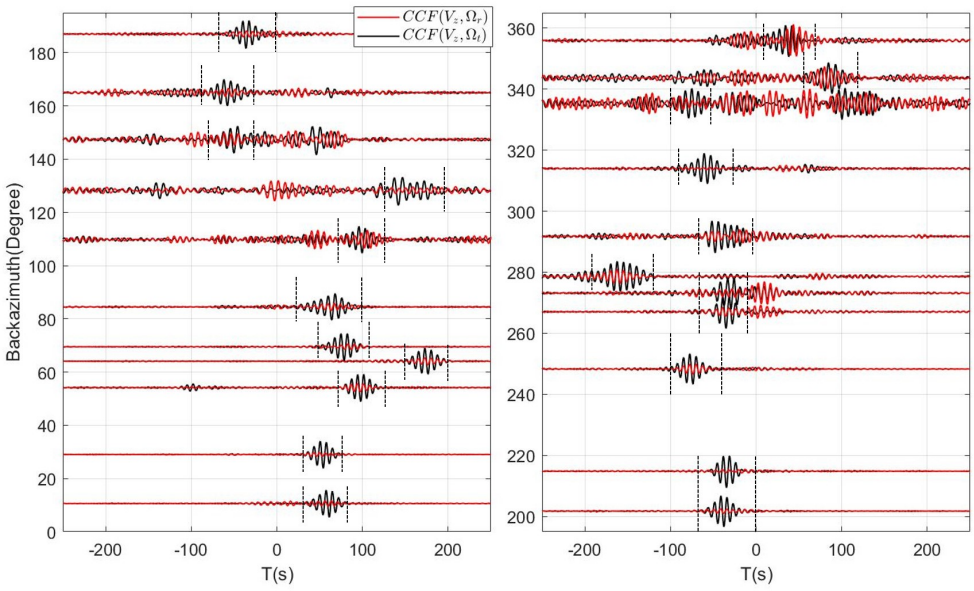

Figure 4.S7: Amplitude comparison (marked by black dashed lines) between $CCF_{(V_z,\Omega_t)}$ and $CCF_{(V_z,\Omega_r)}$ of 7-12s in the azimuth domain. The red lines represent CCFs between the vertical translation of the 3C station and the radial rotation of the 6C station. The black lines represent CCFs between the vertical translation of the 3C station and the transverse rotation of the 6C station.

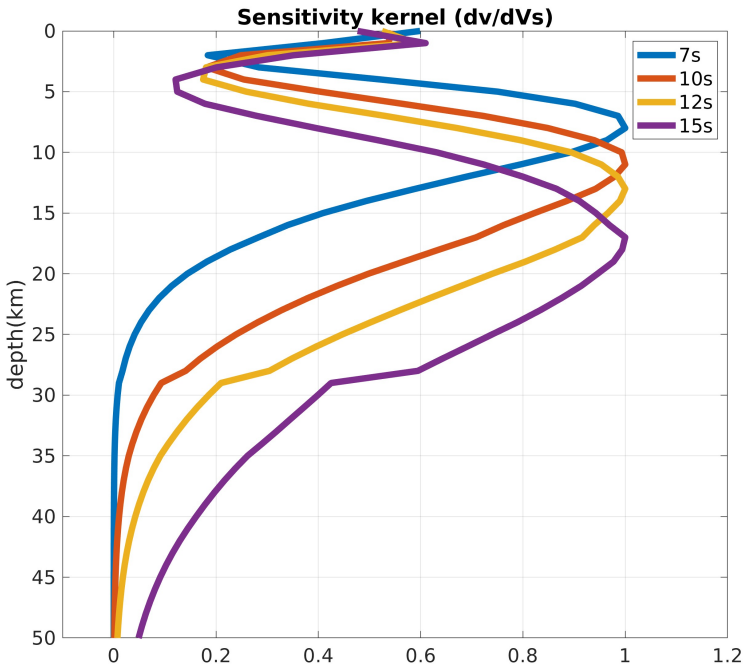

Figure 4.S8: Sensitivity kernel of Rayleigh waves corresponding to shear wave at 7s, 10s, 12s, and 15s.

Chapter 5

Seasonality of microseismic sources in Southern California from 6C ground motions

by Le Tang, Heiner Igel, Jean-Paul Montagner, Celine Hadziioannou and Frank Vernon
In preparation (2025)

5.1 Key Points

• A single 6C observation is capable of revealing the seasonality of microseismic sources.
• Array-derived rotational motions are highly sensitive to the atmospheric pressure-induced ground deformation.
• The secondary microseismic Love waves show large seasonal changes in the southern California region.

5.2 Abstract

Ocean waves interact with the solid Earth generating two dominant signals called microseisms, which carry information about energy exchange between different Earth systems. Here we show that 6C (three-component translation and three-component rotation) observations are able to resolve its seasonal azimuthal variations. We employ the rotational motions retrieved by a small seismic array at the Pinon Flat Observatory (PFO) in southern California to investigate the two dominant microseismic sources: primary and secondary microseisms. The primary microseismic Rayleigh waves show strong seasonal variations as expected, whereas the secondary microseismic Rayleigh waves show slight seasonal changes. In contrast, we find that secondary microseismic Love waves exhibit stable seasonality. This discrepancy from the secondary microseismic Rayleigh waves provides us

with new insights into the generation mechanism of Love waves. In addition, the results suggest that effectively estimating the natural seasonal variation of microseismic sources can provide constraints for the study of seismic anisotropy, while the rotational motion of primary microseisms retrieved by the seismic array is more sensitive to the atmospheric pressure-induced ground deformation.

5.3 Plain Language Summary

The ubiquitous ambient seismic noise recorded by seismographs with a period of 3-20s can be explained by the interaction between ocean waves and the solid Earth. The most convincing mechanism indicates that the interaction between two opposite ocean waves generates a pressure that causes vertical vibrations on the seafloor. Therefore, it is reasonable to observe Rayleigh waves in the secondary microseismic noise (3-10s), but it cannot explain the observed secondary microseismic Love waves. To better understand the generation mechanisms of these two different vibrations, accurately locating the source of microseismic noise is a crucial step. Rotational ground motion describes the angle change of the particle during the Earth's deformation. Theoretically, the vertical component of rotation is only sensitive to SH-type waves (e.g. Love waves), while the horizontal component only records the SV-type waves (e.g. Rayleigh waves). The combination of translational motions and rotational motions provides the feasibility of estimating wave propagation directions at a single seismometer, making it easy to track the noise source, especially the controversial Love waves, and resolve its mechanism.

5.4 Introduction

The interaction between ocean waves and the solid Earth contributes to the generation of two ubiquitous dominant microseisms (Longuet-Higgins, 1950; Iyer, 1958; Hasselmann, 1963; Obrebski et al., 2012; Stutzmann et al., 2012; Ardhuin et al., 2011, 2015, 2019; Gualtieri et al., 2020, 2021): primary microseismic noise (10-20s) and secondary microseismic noise (3-10s). It is currently widely accepted that ocean waves directly interact with seafloor in very shallow water can explain the generation mechanism of primary microseismic Rayleigh and Love waves (Gualtieri et al., 2020, 2021; Fukao et al., 2010; Saito, 2010) at the period of around 10-20s, and the origin of secondary microseismic Rayleigh waves is due to the interaction of two opposite swells, which can produce second-order pressures that interact with the seafloor anywhere (Longuet-Higgins, 1950; Obrebski et al., 2012). From a theoretical point of view, Rayleigh waves should dominate secondary microseismic events because of the pressure loaded by the ocean waves on the seafloor. However, it cannot explain the generation mechanism of secondary microseismic Love waves, which have a horizontal polarization pattern. The current hypotheses for the mechanism of the secondary microseismic Love waves suggest that the presence of bathymetric inclines enables leading to the splitting of the secondary-order pressure force in a component tangent

to inclines which can be responsible for the Love waves (Rind & Down, 1979; Gualtieri et al., 2020, 2021; Le Pape et al., 2021). In addition, lateral heterogeneity within the Earth may also lead to the generation of Love waves due to scattering effects (Rind & Down, 1979; Gualtieri et al., 2020). Despite this, seismologists have been arguing about the origin of secondary microseismic Love waves for decades. To better understand the generation mechanisms of these two different vibrations, especially the Love waves, accurately locating and tracking microseismic sources has always been a big challenge.

Northern Hemisphere storms have stronger winter peaks compared to Southern Hemisphere storms (Colosi et al., 2021), and the seasonality of storms suggests that the interaction between ocean waves and the solid Earth follows seasonal variations. It is expected and understandable that the microseismic source shows seasonality (Schulte-Pelkum et al., 2004; Grob et al., 2011; Schimmel et al., 2011; Stutzmann et al., 2012; Shabtian et al., 2024; Tanimoto et al., 2006, 2016). Due to their different generation mechanisms, the azimuth of the primary microseismic Rayleigh waves has strong seasonal variations (Stehly et al., 2006), while the azimuth variation of the secondary microseismic Rayleigh waves is not significant in the Southern California region (Stehly et al., 2006). It is not clear whether the seasonal variation of secondary microseismic Love waves is as slight as that of Rayleigh waves in this region, but its seasonal observation is crucial for the study of the Love wave generating mechanism.

In the past few years, the emergence of rotational instruments such as ring lasers (Schreiber et al., 2014; Igel et al., 2005, 2021) or fibre-optic gyros (Schreiber et al., 2009) techniques makes it possible to directly measure the rotational ground motion. This additional observation provides new constraints on the local seismic velocity and seismic anisotropy, allowing the investigation of the direction of the plate motion and the stress field (Tang et al., 2023a,c, 2024; Tang & Fang, 2023). The previous study demonstrates the possibility of estimating the microseismic noise source direction based on 6C observations (Hadziioannou et al., 2012; Gualtieri et al., 2020). In addition, the 6C ground motion can naturally separate the microseismic Rayleigh waves into the horizontal rotational components and separate the microseismic Love waves into the vertical rotational component (Hadziioannou et al., 2012; Tang & Fang, 2021a; Tang et al., 2024), thus playing its great advantage of improving the Love wave source measurements. Therefore, we aim to track the seasonal variation of noise sources combining the 6C ground motion, rather than using the conventional noise source imaging approaches (e.g. the beamforming method (Pelaez Quiñones et al., 2023), polarization method (Iyer, 1958; Schimmel et al., 2011) and the cross-correlation method (Stehly et al., 2006)).

Here, we apply the emerging 6C observation to the estimation of seasonal variation of microseismic noise sources. Since currently no (portable) rotation sensing system exists in most regions around the world that allows the analysis of long-term ambient noise observations, we employ the so-called array-derived rotation (ADR) (Spudich et al., 1995; Spudich & Fletcher, 2008; Donner et al., 2017; Tang et al., 2023a, 2024) that makes use of wavefield gradient estimations from surface seismic arrays in appropriate frequency bands. The PFO dense broadband seismic network (Frank Vernon, 2014) has been in operation for several years. The array-derived rotational motion of microseisms can be used to study

the seismic anisotropy (Tang et al., 2024), and allows us to study the long-term changes in microseismic noise sources. We emphasize that the atmospheric pressure-induced ground deformation is highly sensitive to the rotational motions derived by the seismic array, especially the primary microseismic Love waves, which is crucial for characterizing the Earth low noise model of rotational motions (Brotzer et al., 2024). Furthermore, we investigate how to resolve the seasonal azimuthal variations of Rayleigh and Love waves separately from a single 6C observation.

5.5 Methods

5.5.1 Azimuth estimation of surface waves from a single 6C observation

Previous studies have shown that a single 6C observation can estimate the arrival azimuth of an S-type wave (Igel et al., 2007; Hadziioannou et al., 2012; Yuan et al., 2021). Theoretically, it can obtain the azimuth of the surface wave by finding the maximum correlation coefficient between the acceleration (m/s^2) and the rotation rate (rad/s) in the azimuth domain. However, from the observation point of view, since the waveform is affected by noise, the azimuth corresponding to the maximum correlation coefficient is not necessarily the correct azimuth. The azimuth can also be estimated by calculating only the change in the sign of the correlation coefficient (Yuan et al., 2021). After the coordinate system is defined, a grid search is performed in the azimuth domain. The angle in the middle of the positive correlation coefficient region indicates the propagation direction of the surface wave (see Figure 5.1a). For a given noise window with N sampling points, the backazimuth Ψ of Rayleigh waves can be expressed as:

$$\Omega_T(\psi) = \Omega_E cos(\psi) - \Omega_N sin(\psi); \psi \in [0, 2\pi] \tag{5.1}$$

$$r(\psi) = \frac{\sum_{i=1}^{N}(A_{z_i} - \overline{A_z})(\Omega_{T_i} - \overline{\Omega_T})}{\sqrt{(\sum_{i=1}^{N}(A_{z_i} - \overline{A_z})^2)(\sum_{i=1}^{N}(\Omega_{T_i} - \overline{\Omega_T})^2)}}; min(\frac{\partial r}{\partial \psi}) \mid_{\psi=\psi_1}; max(\frac{\partial r}{\partial \psi}) \mid_{\psi=\psi_0} \tag{5.2}$$

$$\begin{cases} \Psi = (\psi_0 + \psi_1)/2; & \psi_0 <= \psi_1 \\ \Psi = (\psi_0 + \psi_1)/2 - \pi; & \psi_0 > \psi_1, (\psi_0 + \psi_1)/2 > \pi \\ \Psi = (\psi_0 + \psi_1)/2 - \pi; & \psi_0 > \psi_1, (\psi_0 + \psi_1)/2 < \pi \end{cases} \tag{5.3}$$

where ψ is the backazimuth from 0 to 2π. Ω_N and Ω_E represent the rotational rate in the north and east components, respectively. Ω_T represents the rotated horizontal rotational rate at a certain ψ. r is the Pearson correlation coefficient between vertical acceleration A_z and transverse rotation rate Ω_T, while $\overline{A_z}$ and $\overline{\Omega_T}$ are their mean values. ψ_0 and ψ_1 are the maximum and minimum values of the first-order partial derivative of r with respect to ψ, respectively. Ψ is the estimated backazimuth.

For Love waves, Ω_T, Ω_E, Ω_N, and A_z are replaced by A_T (transverse acceleration), $-A_E$ (acceleration in the east component), $-A_N$ (acceleration in the north component), and Ω_z (vertical rotation rate), respectively.

5.5.2 Azimuthal seismic anisotropy from 6C amplitude measurements

Our recent paper (Tang et al., 2023c,a, 2024) demonstrate that the amplitude ratio of acceleration to rotation rate or strain rate is equal to the analytical azimuth-dependent phase velocity of the corresponding surface wave (Smith & Dahlen, 1973). The dispersion equation of the Rayleigh wave from the amplitude ratio can be expressed as (Tang et al., 2023c):

$$\begin{cases} |\frac{A_z(\omega,\psi)}{\Omega_T(\omega,\psi)}| = c_{R0}(\omega) + \frac{1}{2c_{R0(\omega)}}[R_1(\omega) + R_2(\omega)cos(2\psi) + R_3(\omega)sin(2\psi) \\ \qquad\qquad +R_4(\omega)cos(4\psi) + R_5(\omega)sin(4\psi)] \end{cases} \tag{5.4}$$

where $A_z(\omega, \psi)$ is the vertical acceleration and $\Omega_T(\omega, \psi)$ is the transverse rotational velocity. ψ is the backazimuth of the wavenumber vector measured clockwise from the north direction. $c_{R0}(\omega)$ is the phase velocity of the Rayleigh wave for the isotropic medium considered as a reference model. $R_i(\omega)$ $(i = 1, 2, 3, 4, 5)$ are respectively depth integration functions that involve some elastic parameters and eigenfunctions, where we used a simple integration expression derived by (Montagner & Nataf, 1986), whose explicit expressions can be found in Equations (2), (4), and (5) of (Montagner & Nataf, 1986). Equation 5.4 provides a method for estimating phase velocities in anisotropic media which only depends on amplitude information.

5.6 Data

Considering that broadband rotational seismometers with sufficient sensitivity have not been permanently deployed widely, we select three-component broadband seismometers at Piñon Flat Observatory in southern California as the reference 6C station (see Figure 5.1b) to retrieve rotational ground motions using the ADR approach (Spudich et al., 1995; Spudich & Fletcher, 2008; Tang et al., 2023a, 2024). The ambient noise data comes from the PY seismic networks (Frank Vernon, 2014), IRIS data center. We select 8 three-component stations (see Figure 5.1b) and use four-years ambient noise data from January 2016 to January 2020 to investigate the seasonal variation of microseismic noise sources. In the following air-pressure data analysis, we use the co-located pressure station near the PY.BPH03 station (see Figure 5.1b). Figure 5.1b shows the geometry of seismic stations and the black triangles are the distributions of 3C stations, where the aperture of the seismic array is about 500m. The period range of wavefield gradients from the virtual 6C station is about 3-50s (Donner et al., 2017), allowing the retrieval of rotational motions from two dominant microseismic noise data (5-10s: Secondary microseismic noise. 10-20s:

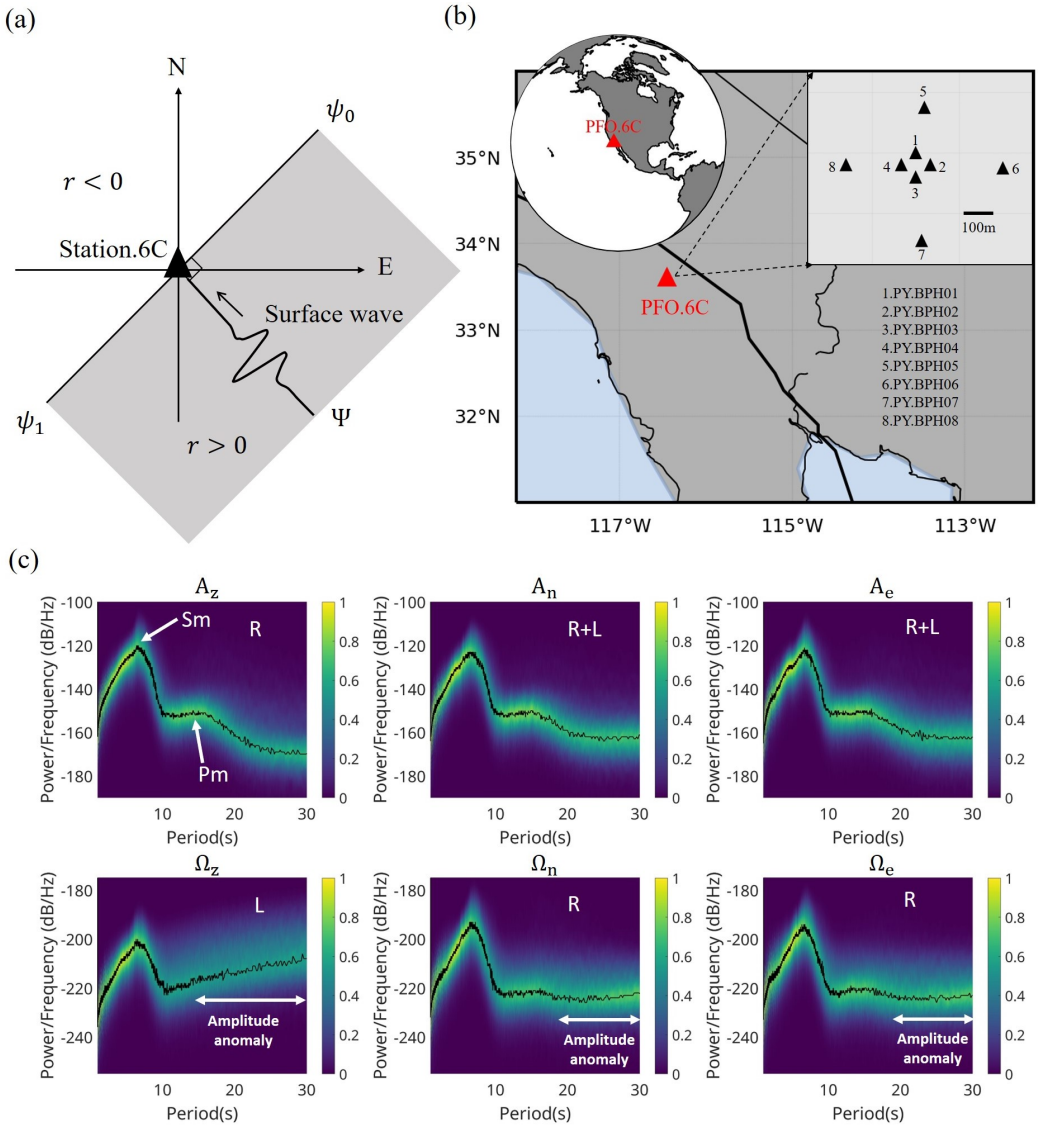

Figure 5.1: (a) Schematic diagram of the principle (see Equations 5.1-5.3) of azimuth estimation for a single 6C station. r is the Pearson correlation coefficient between vertical acceleration and transverse rotation rate. ψ_0 and ψ_1 are the maximum and minimum values of the first-order partial derivative of r with respect to ψ, respectively. Ψ is the real backazimuth of surface waves. (b) Distributions of selected 8 broadband seismic arrays in the Pinon Flats Observatory. The small array can be regarded as a virtual 6C station. The maximum aperture of this array is about 500m. (c) PSD of 6C microseisms in the winter (2018.September-2018.December and 2018.January-2018.February). The double white arrows indicate the identifiable period range of the amplitude anomaly on PSD. 'R' and 'L' represent the Rayleigh and Love wave, respectively. 'Pm' and 'Sm' represent the primary microseisms and secondary microseisms, respectively.

Primary microseismic noise). We calculate the azimuth of the microseismic noise source with a 10s moving window. In each 10s waveform window, we search for its incident azimuth Ψ in the azimuth range of 0-2π based on Equations (5.1-5.3) and estimate the local velocity using the Equation 5.4. To eliminate the interference of other waves as much as possible, we set a threshold here, that is, when the maximum correlation coefficient r of this time window is larger than 0.8, the waveform of this time window is considered to be the signal of interest, otherwise this window is skipped.

5.7 Results

5.7.1 Atmospheric pressure effect on array-derived rotational motions

We divide the one-year microseismic data into winter (September-December and January-February) and summer (March-August) to examine the seasonal variations of microseismic sources. Figure 5.1c shows the power spectral density (PSD) of the array-derived 6C observations in winter (see Figure 5.S1 for the PSD in summer) at the PFO array, where 'L' means that the Love wave dominates in the microseismic noise data and 'R' indicates Rayleigh waves. The primary microseismic noise (10–20s) marked by 'Pm' and the secondary microseismic noise (5–10s) marked by 'Sm' in Figure 5.1c can be identified from the PSD of the acceleration (A). In addition, the PSD of three-component rotation shows that the secondary (5-10s) microseismic Rayleigh waves and Love waves show obvious peaks at 7s in both winter and summer (see Figure 5.1c and Figure 5.S1) (Ω_z records Love waves while Ω_n and Ω_e record Rayleigh waves). However, compared with the acceleration, the PSDs in the primary microseisms and longer period range show an unfavorable trend in rotational motions, which is marked by white double arrows in Figure 5.1c. Theoretically, the PSDs of rotational motions should have similar patterns as the acceleration, while the amplitude anomaly in Figure 5.1c and Figure 5.S1 is not expected to appear in the rotational motions. For Rayleigh waves recorded in horizontal rotational components, its PSD is mainly contaminated above 20s (see Ω_n and Ω_e in Figure 5.1c). Therefore, the peak of the primary microseismic Rayleigh wave (10-20s) is still visible, and the summer value is relatively weak (see Figure 5.S1). Compared with Rayleigh waves, the PSD of Love waves in the vertical rotation component is more seriously contaminated starting from 10s (see Figure 5.1c), making it difficult to distinguish the primary microseismic Love waves.

In theory, the lateral heterogeneity within the seismic array can also lead to amplitude anomalies using the ADR method. Considering that the PFO region is relatively homogeneous, indicates that the heterogeneity effect probably is not the main reason. It has been demonstrated that the ambient seismic noise at periods of 20-100s is mostly generated by wind-related surface pressure change when surface pressure is large (Tanimoto & Wang, 2021). To investigate whether the rotation amplitude anomalies are related to the pressure-induced ground deformation, we filter the seismic noise and pressure data to a given frequency range and compare their PSDs. Figure 5.2a shows the scatter density plot

(each data point represents the PSD of one-hour time window) of the PSD calculated using two months data (June to July 2018) in the period range of 10–20s. It shows that the coherence between acceleration and pressure is smaller than 0.1 (see Figure 5.2a), indicating the acceleration of primary microseisms is less affected by the air pressure-induced noise.

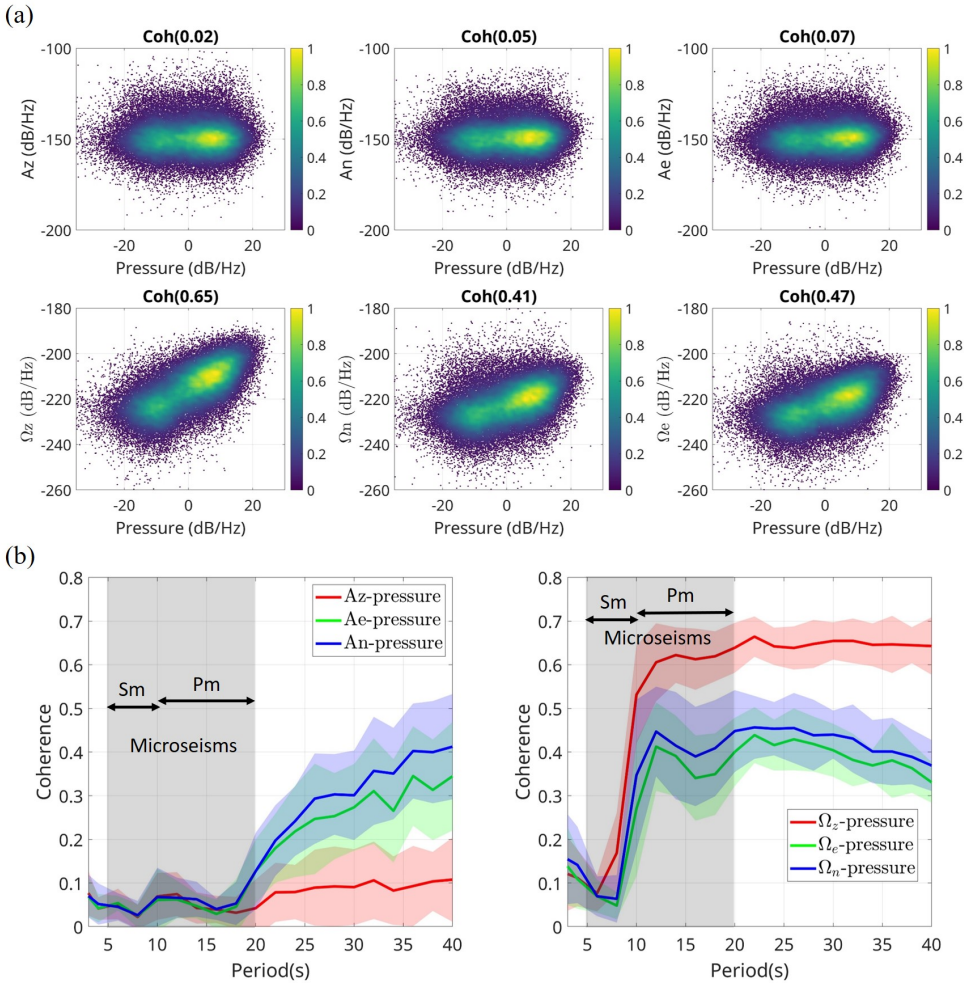

Figure 5.2: Air pressure effect on the amplitude of microseisms. (a) The scatter density spectra between the pressure PSD (dB/Hz) and the seismic noise PSD (dB/Hz) of two months data (2018.June-2018.July) in the period range of 10-20s. The coherence (Coh<0.1) between pressure and acceleration (A) is much smaller than the coherence (Coh>0.4) between pressure and rotational rate (Ω). (b) Coherence comparison between acceleration-pressure (left panel) and rotation-pressure (right panel) in different periods (3-40s). In the left panel, red, green, and blue lines represent the vertical, east, and north acceleration components, respectively. In the right panel, red, green, and blue lines represent the vertical, east, and north rotational components, respectively. 'Sm' and 'Pm' with arrows represent the period range of the secondary microseismic noise and the primary microseismic noise.

In contrast, the rotational motions of 10-20s are highly related to the pressure data, especially the Love wave (see Figure 5.2a and 5.2b) in the vertical rotational motion, whose coherence is larger than 0.6, implying that the three-components rotation is more sensitive to pressure-induced ground deformation than translations. As shown in Figure 5.2b, the small coherence between acceleration and pressure suggests that the pressure effect on acceleration can be negligible in the two dominant microseismic noise range. However, the rotational component is suddenly affected from the 10s (Figure 5.2b), indicating that the PSD anomaly on rotations (Figure 5.2c) is highly related to the atmospheric pressure. It suggests that the rotational motion of secondary microseisms is more reliable, whereas the results of primary microseisms must be carefully evaluated when estimating the direction of the noise source.

5.7.2 Seasonal azimuth variation of microseismic sources

Figures 5.3(a-d) shows the backazimuth density spectrum of microseismic noise sources estimated by Equations (5.1-5.3) from January 2016 to January 2020. As shown in Figure 5.3a, the secondary microseismic Rayleigh waves are mostly distributed between 200 and 250 degrees, while the winter noise source is slightly shifted to the northwest direction, and has an obvious seasonal cycle. Although a high correlation coefficient threshold (see the Data section) is set to evaluate each time window when estimating the noise azimuth, the error caused by the overlap of noise sources cannot be completely eliminated. Compared with the slight seasonal variation of the secondary microseismic Rayleigh wave in Figure 5.3a, the seasonal variation of the secondary microseismic Love wave (Figure 5.3b) is obvious and accompanied by a large disturbance range. It is mainly distributed in 275-315 degrees in winter and in 210-270 degrees in summer. In addition, there is also some energy in the azimuth range of 120-180 degrees (Figure 5.3a and Figure 5.3b), which indicates that secondary Love waves have few noise sources coming from this direction.

As illustrated in Figure 5.2b, the amplitude of the primary microseisms seems to be severely contaminated by atmospheric pressure-induced ground deformation, especially Love waves. It is worth investigating how the pressure-induced ground deformation affects the backazimuth estimation since the coherence for the primary microseismic Rayleigh wave is below 0.5, probably can lead to a reliable solution. Therefore, we also filter the seismic noise data to 10–20s and calculate the backazimuth using Equations (5.1–5.3) with the same moving time window (see Data section). Figure 5.3c shows that the primary microseismic Rayleigh waves (10–20s) have strong seasonal backazimuth variations, while the winter noise mainly comes from two dominant directions, 0–45 and 270–350 degrees, and the summer noise is around 200–270 degrees. The primary Love wave in Figure 5.3d shows a complex noise distribution, which appears in almost all backazimuths. It indicates that the main source comes from around 300-350 degrees, and there is also a recognizable energy cycle at around 135 degrees, and slight seasonal changes are visible.

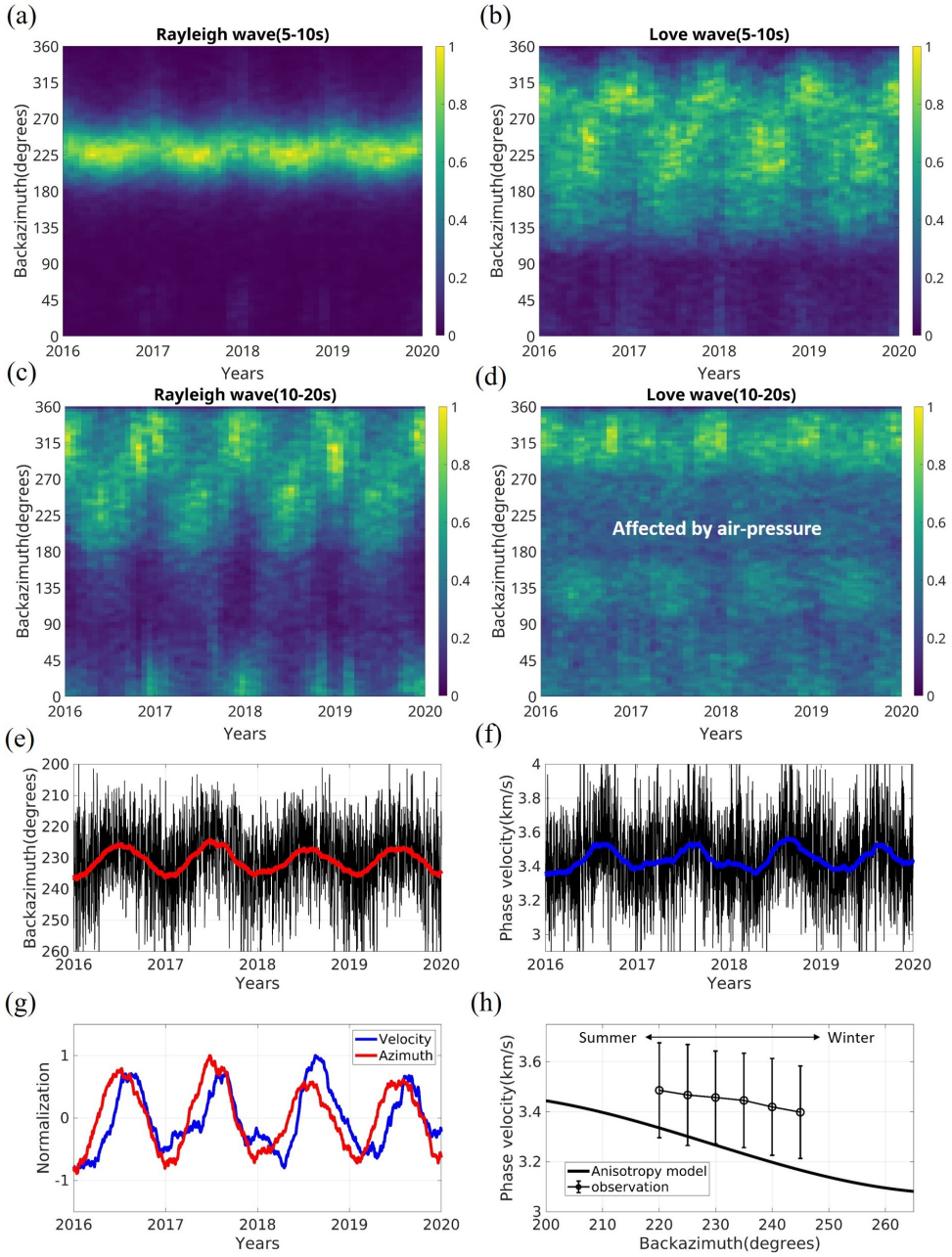

Figure 5.3: Seasonal variations in microseismic backazimuth and velocity from 2016 to 2020 using the array-derived 6C observation. (a) and (b) represent the seasonal backazimuth variation of the secondary microseismic Rayleigh and Love wave (5-10s), respectively. (c) and (d) represent the seasonal backazimuth variation of the primary microseismic Rayleigh and Love wave (10-20s), respectively. (e) and (f) represent the backazimuth and phase velocity of secondary microseismic Rayleigh wave (5-10s), respectively, where the black data points are obtained by using Equations (5.1-5.4) with a one-day smoothing window. Here we only keep the backazimuth between 200 and 260 degrees and velocity between 2.8 and 4.0 km/s. The red and blue lines in (e-g) are the smoothing result using the black data points with a three-month time moving window. (h) The anisotropy model is obtained by Tang et al. (2024) using the 6C cross-correlation method. The observation data represents the phase velocity variation with a 10 degrees smoothing window based on the black data points of (e-f).

However, this can be an error affected by atmospheric pressure because of the contamination of the primary Love wave (see Figure 5.1c and Figure 5.2b).

5.8 Discussion

5.8.1 Local seismic anisotropy by seasonal azimuth variations

As shown in Equation 5.4, a single 6C observation enables estimating the local seismic anisotropy by employing the azimuth-dependent amplitude ratio between acceleration and rotation (Tang et al., 2023c,a, 2024). Therefore, the obvious seasonal variation of microseisms in Figures 5.3(a-d) makes it possible to extract the azimuth-dependent seismic phase velocity to constrain the Earth's anisotropy. Considering that the amplitude of the primary microseismic surface waves is contaminated by pressure-induced ground deformation (see Figure 5.1c and Figure 5.2), and the Love wave is easily contaminated by coupled waves in general anisotropic media (Tang et al., 2023c), we aim to measure the phase velocity of secondary microseismic Rayleigh waves. The black data points in Figures 5.3(e-f) represent the daily backazimuth and phase velocity changes. Their mean value (red line: backazimuth, blue line: velocity) obtained by a three-month time window shows consistent seasonal disturbances. This indicates that the observed velocity changes in Figure 5.3f are probably associated with the noise source change in Figure 5.3e. Although seasonal temperature changes (Richter et al., 2014) and fluctuations in groundwater levels (Mao et al., 2022) can also lead to velocity variations, these factors appear insufficient to explain the velocity fluctuations of about 0.4 km/s in the upper crust (see Figure 5.3f). To better illustrate that the seasonality of seismic velocity is related to azimuths, we compare the estimated velocity with the local anisotropy model (see Figure 5.3h) of the Rayleigh waves (5-10s), which is obtained by the cross-correlation function method (Tang et al., 2024). The observed results (see Figure 5.3h) show that the azimuth is smaller and the phase velocity is larger in summer, while the opposite is true in winter, and the trend is consistent with the azimuth anisotropy model (black line in Figure 5.3h). Although the extracted velocities deviate from the model and have large uncertainties, the local strong anisotropy (Tang et al., 2024) can explain the velocity variation of about 0.3 km/s in the small azimuth range of 220-250 degrees. Consequently, the seasonal change in velocity is more likely to be the azimuthal anisotropy caused by the change in the azimuth of the noise source, providing information on the anisotropy of the upper crust.

5.8.2 Origin of microseismic Rayleigh and Love wave sources

We compare our results with those of a relatively large array-based beamforming approach (Schröer, 2019) (see Figure 5.4 and Figures S(5.S2-5.S4), where the aperture of the seismic array is about 103km) and project the dominant backazimuth of the noise sources for both approaches in the global map shown in Figure 5.4 (see Figures S(5.S2-5.S4) for the detailed beamforming results). As illustrated in Figure 5.4, the dominant primary and secondary

microseismic Rayleigh waves are consistent with the results of the beamforming methods. It demonstrates the reliability of the 6C method and suggests that the effects of atmospheric pressure can be neglected when estimating seasonal Rayleigh wave sources. The generation mechanism of the secondary microseismic Rayleigh waves at a backazimuth of about 200-250 degrees (Figure 5.4a) is due to the continuous interaction of two opposite swells that exerts strong second-order pressure on the seafloor (the black pentagram in Figure 5.4a indicates the approximate source position of the secondary microseismic Rayleigh wave in a specific period). The generation of primary microseisms is due to the direct interaction between ocean waves in shallow waters and the seafloor (Ardhuin et al., 2011, 2015, 2019; Fukao et al., 2010; Saito, 2010), and is therefore strongly related to the seasonal changes in global ocean waves (Colosi et al., 2021). It indicates that the primary microseismic Rayleigh waves mainly come from three directions (Figure 5.4b), among which the sources around 4-45 degrees are generated by the interaction between Atlantic waves and the solid Earth, and the sources around 220-270 degrees and 280-350 degrees are excited by the interaction between Pacific waves and the seabed (Stehly et al., 2006). Although the primary microseismic Love wave is inevitably affected by the air pressure (see Figure 5.2b), its source region (around 290-340 degrees in Figure 5.4d) seems to be similar to the results (around 290-335 degrees in Figure 5.4h) of the beamforming method in winter. However, it is difficult to compare the 6C results in summer with the beamforming results because the low energy (Figure 5.3d) and strong atmospheric pressure effect (Figure 5.2b) make it unreliable.

As shown in Figures 5.4c and 5.4g, the backazimuth of the secondary microseismic Love wave source from the 6C and beamforming methods is consistent. However, the result of the beamforming method (Schröer, 2019) shows that there are stable sources that come from 110-150 degrees in both winter and summer, which may be due to data errors or other reasons. We cannot reasonably explain this phenomenon and need more observations. The generation mechanism of secondary microseismic Love waves has always been controversial. Previous studies (Rind & Down, 1979; Gualtieri et al., 2020; Le Pape et al., 2021) have shown that it can be generated by the horizontal force split from the interaction between the second-order pressure of waves in any sea area and the inclined seabed, or it can be converted in a heterogeneous medium. Both hypotheses can explain the secondary microseismic Love waves around 210-270 degrees in summer (Figure 5.4c), because there are a large number of Rayleigh wave sources at around 200-250 degrees (see Figure 5.4a), which can produce scattering and conversion. However, a considerable number of secondary microseismic Love wave sources are observed around 275-315 degrees (Figure 5.4c), and it seems difficult to convert the Rayleigh wave sources of around 220-270 degrees (Figure 5.4a) into Love wave sources in winter. The possible reason is that the strong ocean waves from the North Pacific in winter (Colosi et al., 2021) and the ocean waves reflected from the coast generate pressure, which interacts with the inclined seabed near the coast, and the split horizontal force promotes the generation of Love waves.

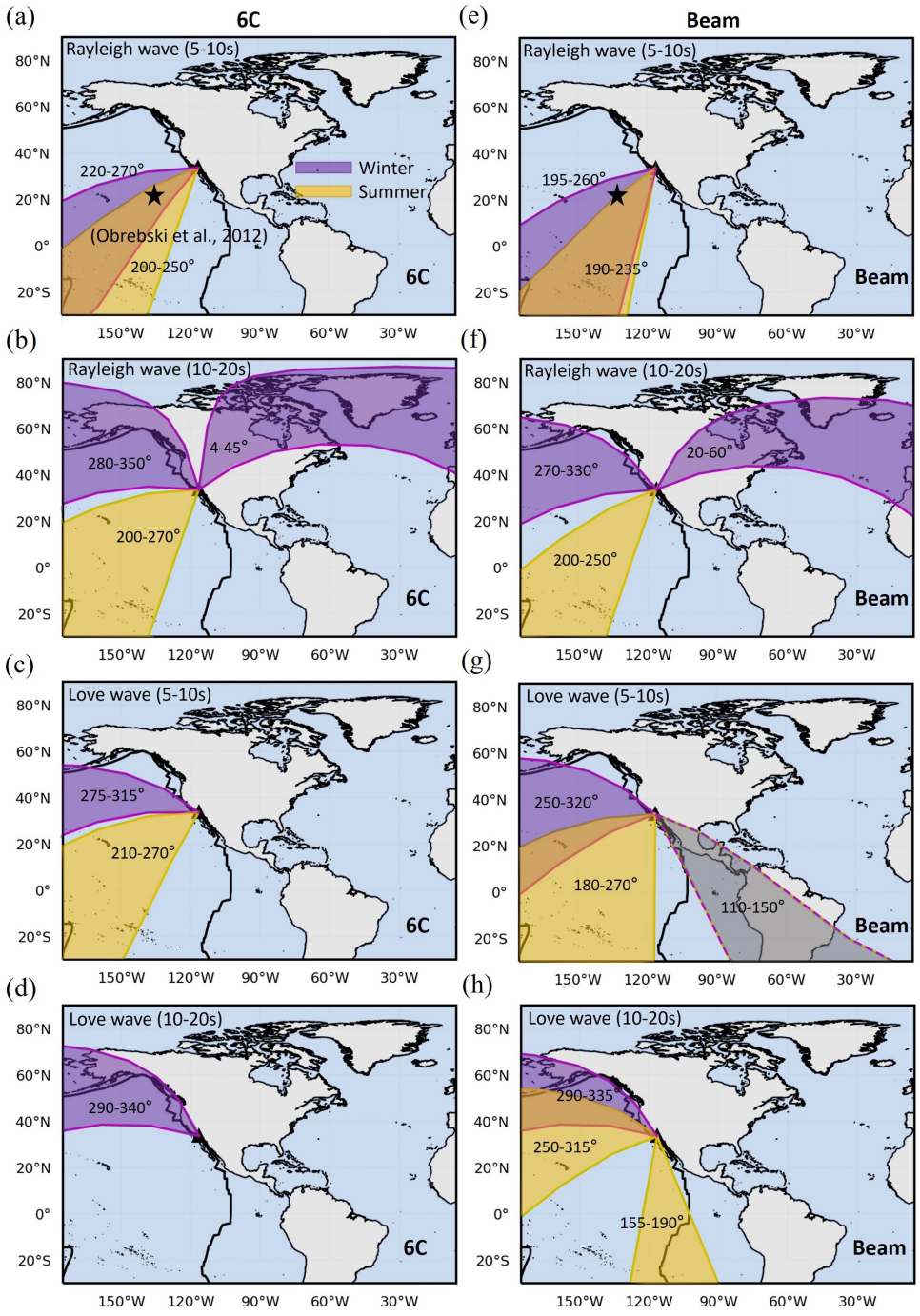

Figure 5.4: Projection of dominant microseismic noise sources in 2016-2017. (a-d) represent the noise source estimated using the 6C method based on the PFO.6C array. (e-h) represent the noise source estimated using the beamforming method based on a large seismic array (see Figures S(2-4), the aperture is about 103km) (Schröer, 2019). The yellow and purple shaded zones represent the noise source projections in summer and winter, respectively. The grey shaded zone in (g) indicates the overlap of the yellow and purple shaded zones. The black pentagram indicates the location of the main secondary microseismic Rayleigh wave source obtained by combining observations and numerical simulations (Obrebski et al., 2012).

However, these observations and hypotheses need to be combined with accurate velocity models and storm sources to provide more evidence by simulating the complex interaction between ocean waves and the solid Earth (Gualtieri et al., 2020). Besides, in further studies, we need to deploy more seismic arrays or available rotational seismometers to accurately locate the source region.

5.9 Conclusion

We observe for the first time seasonal variations in the microseismic noise source from 6C ground motions, especially allowing us to track the secondary microseismic Love waves. Such azimuthal seasonality of microseismic sources can provide constraints on the study of local seismic anisotropy. The discrepancy between the sources of secondary microseismic Rayleigh and Love wave indicates the complexity of the secondary microseismic Love wave mechanism, which provides us with new insight into the generation mechanism of the secondary microseismic Love wave. The rotational motion can be used to separate Love waves, which is crucial for the study of the Love wave generation mechanism. It is expected that when more available rotational seismometers are deployed, a more accurate explanation for the origin of the Love wave source can be provided. The current 6C approach should further motivate the development of portable rotational sensors with sensitivity below the Earth's low noise level. In the future, the 6C technique could be applied to portable rotational seismometers, which is expected to be particularly useful whenever seismic arrays are not affordable or difficult to implement (e.g., planetary or ocean bottom observations, volcanology, urban seismology).

5.10 Acknowledgments

This work is funded by the European Union's Horizon 2020 research and innovation program under the Marie Skłodowska-Curie grant agreement No 955515 (www.spin-itn.eu). Heiner Igel is grateful for the Cecil and Ida Green visiting scholarship at the Institute of Geophysics and Planetary Physics of the University of Southern California at La Jolla in 2022 and 2023.

5.11 Open Research

The ambient noise data is publicly available and accessed from the PY network (Frank Vernon, 2014), where the three-component stations are PY.BPH01, PY.BPH02, PY.BPH03, PY.BPH04 PY.BPH05 PY.BPH06, PY.BPH07, and PY.BPH08. The array-derived rotation (ADR) code and noise source estimation code are available from tangle0129 (2023).

5.12 Appendix: Supplementary materials

Contents of this file
Figures 5.S1 to 5.S4

5.12.1 Supplementary figures

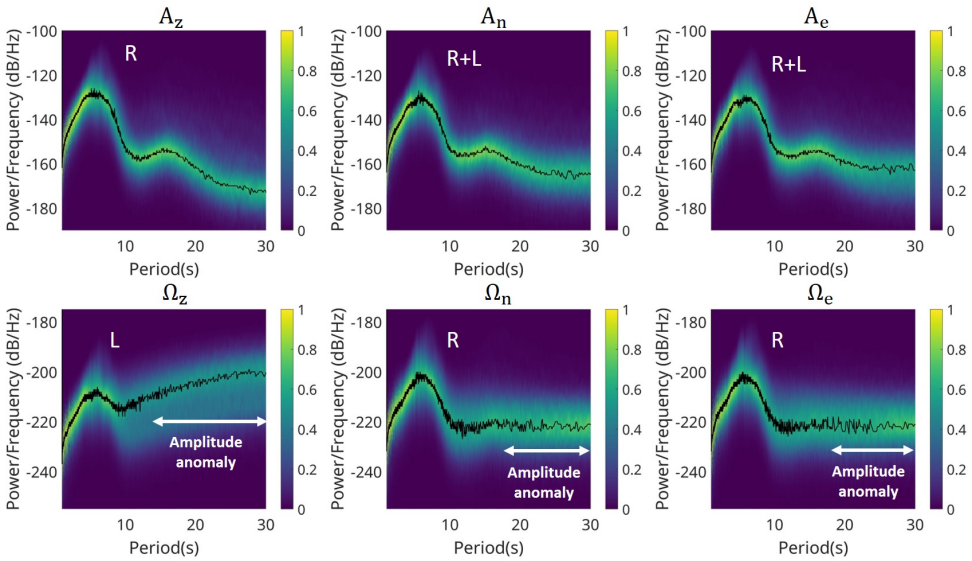

Figure 5.S1: PSD of 6C microseisms in the summer (2018.March-2018.August). The double white arrows indicate the identifiable period range of the amplitude anomaly on PSD. 'R' and 'L' represent the Rayleigh and Love wave, respectively.

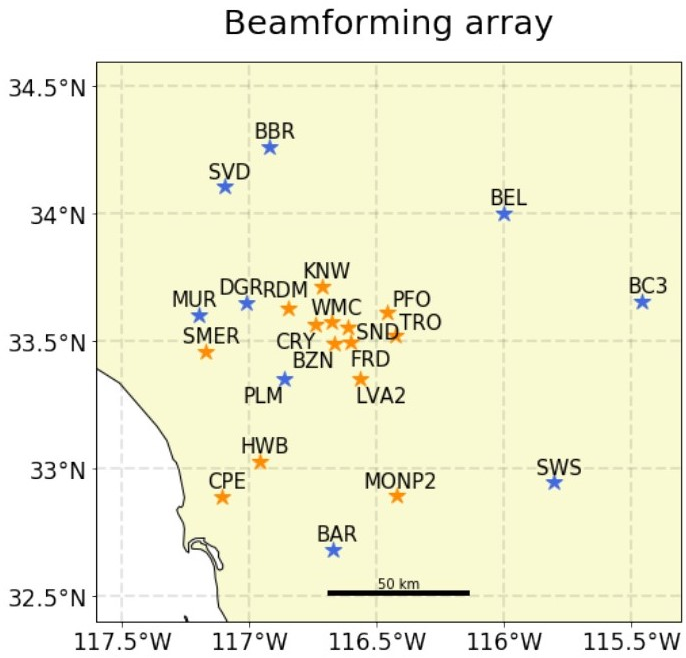

Figure 5.S2: Structure of the array used for beamforming. Stations marked in red appear in both variants while stations marked in blue are only used for the primary oceanic microseism. For the smaller array the maximum aperture is 103km and 180km for the larger array (Schröer, 2019).

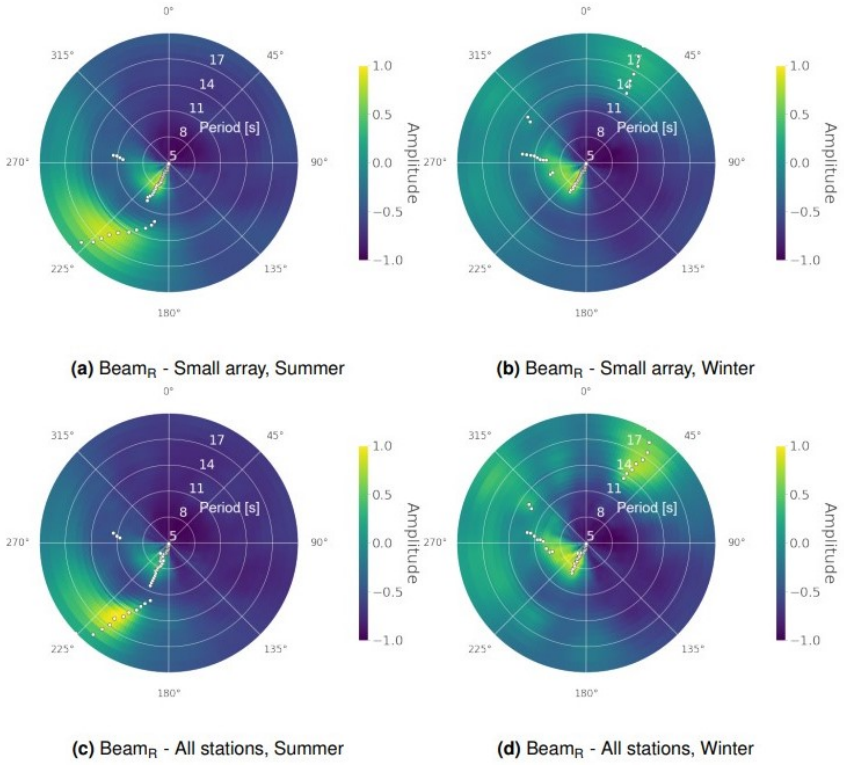

Figure 5.S3: The backazimuth of Love waves, averaged over summer and winter, using a slowness of 0.26s/km. (a) and (b) show the results using the small array for summer and winter respectively, while (c) and (d) display the results using all stations. The correlations are plotted for all backazimuths and periods. High values are colored yellow, with a white dot plotted on the highest beamformer values found within a time or period window (Schröer, 2019).

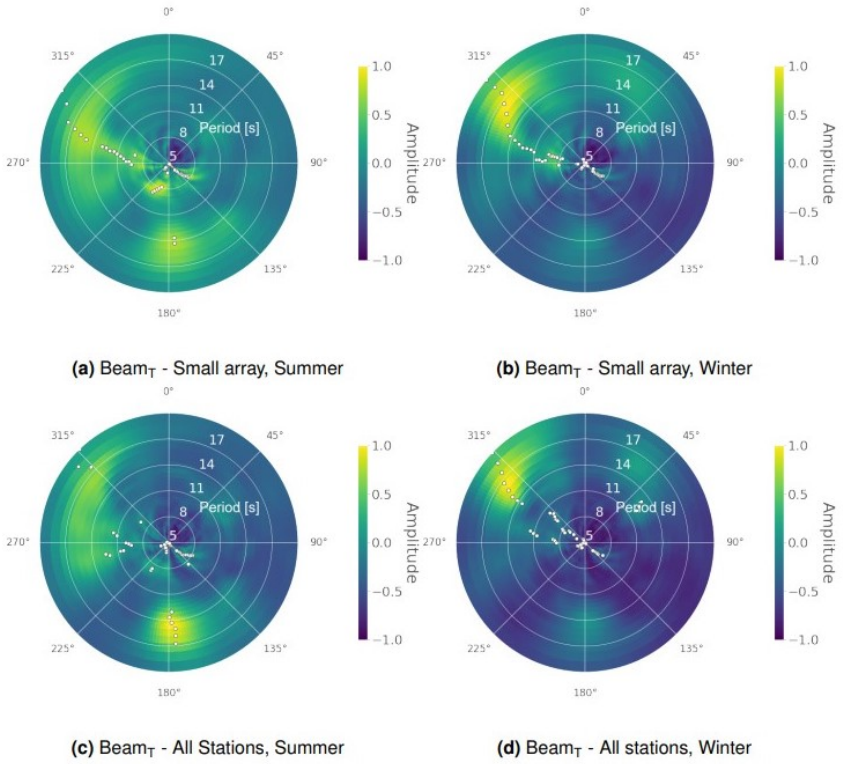

Figure 5.S4: The backazimuth of Rayleigh waves from beamforming methods, averaged over summer and winter, using a slowness of 0.3s/km. (a) and (b) show the results using the small array for summer and winter respectively, while (c) and (d) display the results using all stations. The correlations are plotted for all backazimuths and periods. High values are colored yellow, with a white dot plotted on the highest beamformer values found within a time or period window (Schröer, 2019).

Chapter 6

Conclusion and Outlook

This thesis proposes a novel theory for investigating 6C anisotropy in surface waves and applies it to various data types, from seismic events to ambient seismic noise data. The agreement between the theory and actual observations demonstrates the practicality of the 6C anisotropy theory. This paves the way for advancements in rotational seismology and provides a new approach to examining seismic anisotropy and studying the Earth's interior.

First, the thesis presents a concise polarization form for rotation and strain in weakly anisotropic media using first-order perturbations. This form provides a clear description of particle motion and allows for the verification of primary surface waves by comparing them with numerical results. However, verifying the dispersion relation of coupled waves is challenging due to their typically small amplitude in weakly anisotropic media. The first-order perturbation theory demonstrates that the rotation vector is perpendicular to the wavenumber vector, resulting in the radial rotation component Ω_r always being equal to zero. From an observational point of view, recorded seismograms, especially in the short period range, will contain scattered waves from all directions due to the structure heterogeneity of the Earth. Hence, the signal in the radial rotational component of an earthquake event comes from the scattered waves, not the effect of anisotropy. As the frequency decreases, the Earth's structure generally becomes more uniform, and the amplitude of the radial rotation component tends toward zero.

Furthermore, this thesis proposes a 6C amplitude-based method for calculating dispersion curves in weakly anisotropic media using a single 6C observation. Existing seismic anisotropy observation methods struggle to provide reliable resolution in both lateral and vertical directions. For instance, travel-time tomography lacks good lateral resolution, while amplitude polarization analysis based on a single station can not accurately resolve depth. Therefore, the proposed 6C surface wave anisotropy theory aims to address these limitations by simultaneously providing good lateral and vertical resolution. The proposed amplitude-based dispersion measurement method requires extremely high accuracy of amplitude measurement, as even a minor amplitude disturbance can lead to significant deviation. Thus, using multiple seismic records is essential to obtain reliable velocities. This theory also indicates that the fundamental mode of Rayleigh wave is relatively stable,

as its dispersion curve is well isolated from those of other modes and does not couple too strongly with adjacent modes. On the contrary, the fundamental mode of Love wave is influenced by the fundamental mode of Rayleigh wave and higher modes.

Next, we test the proposed 6C anisotropy theory by studying upper mantle anisotropy in southern California. This region has a complex tectonic and geodynamic environment, making it an ideal location for our new method. Since no portable rotational sensing systems can analyze multi-azimuth observations, we use the array-derived rotation (ADR) method, which utilizes wavefield gradient estimates from a surface seismic array. Our results demonstrate that we can extract local structure and anisotropy with good lateral and vertical resolution by considering the amplitude ratio between translation and rotation. This allows us to understand the upper mantle's azimuthal anisotropy and study depth-varying plate deformation and local mantle flow, providing new insights into southern California's geodynamic processes and tectonic evolution. Our findings also provide valuable constraints on the stratification of upper mantle anisotropy, complementing current seismic observation methods such as SKS splitting or surface wave tomography.

In addition, extending the 6C anisotropy theory to ambient seismic noise allows us to study seismic anisotropy without waiting for an earthquake to occur. Therefore, this thesis proposes a pioneering method for studying local seismic anisotropy based on 6C ambient noise data. Based on the ambient noise cross-correlation technique, we focus on amplitude information and extract the azimuth-dependent velocity anisotropy by calculating the amplitude ratio of the cross-correlation function of two stations. We analyze the stability of this method and show that after a long period of noise cross-correlation, the velocity based on the amplitude ratio can stably converge to the absolute velocity. However, the premise is that a high signal-to-noise ratio cross-correlation waveform is required. We also analyze the impact of noise sources on the ratio of cross-correlation waveforms, and the results show that the noise source deviation can theoretically be solved by azimuth correction. However, it still produces significant uncertainties in actual data. We apply this method to the PFO array in southern California and resolve local seismic anisotropy within the period of secondary microseismic noise. It reveals stress-induced seismic anisotropy with slightly varying azimuths at different depths, providing new insights into the origin of depth-dependent anisotropy.

The thesis also analyzes the potential of 6C ground motions in resolving microseismic source mechanisms. Observing seasonal variations in microseismic noise sources based on 6C ground motions allows us to track secondary microseismic Love waves. This seasonal variation in the microseismic source azimuth is expected to provide valuable constraints for studying local seismic anisotropy. The differences between secondary microseismic Rayleigh and Love wave sources indicate the complexity of the secondary microseismic Love wave generation mechanism and provide new insights. The potential of rotational motion to separate Love waves is a crucial step in studying their generation mechanism. With the deployment of more rotational seismometers, the origin of Love wave sources is expected to be explained more precisely.

Currently, only a few areas of the world have broadband rotational seismometers with sufficient sensitivity. To showcase the potential of our method, we have opted to use the

ADR method to retrieve rotational waveforms from seismic arrays. Although it has some limitations, ADR is our sole option for obtaining rotational waveforms. The aperture of the seismic array, the noise level, and the instrument amplitude errors restrict the period range. The wavelength-scale heterogeneity beneath the array overturns the homogeneity assumption of the ADR approach. Additionally, the inhomogeneity of the geometric distribution of stations impacts the phase and amplitude of the retrieved rotational waveforms. Even minor waveform errors can result in significant deviations in estimated velocity. Consequently, there is an urgent need for the development and deployment of portable broadband rotational seismometers with low noise levels, as direct observation of rotation can eliminate the period limitation of the ADR method and errors caused by irregular station deployment and reduce the influence of structural heterogeneity.

The current 6C method should further promote the development of portable rotational sensors with sensitivity below the low noise level of the Earth. In the future, the 6C technique can be applied to portable rotational seismometers, which is expected to be particularly useful in expensive or challenging seismic array implementations, such as planetary or seafloor observations, volcanology, and urban seismology.

Appendix A

Elastic tensor of anisotropic media

The elastic tensor of VTI media can be expressed as:

$$\mathbf{C}_{VTI} = \begin{pmatrix} C_{11} & C_{11}-2\cdot C_{66} & C_{13} & 0 & 0 & 0 \\ & C_{11} & C_{13} & 0 & 0 & 0 \\ & & C_{33} & 0 & 0 & 0 \\ & & & C_{44} & 0 & 0 \\ & \textbf{sym.} & & & C_{44} & 0 \\ & & & & & C_{66} \end{pmatrix} \tag{A-1}$$

The elastic tensor of orthorhombic media can be expressed as:

$$\mathbf{C}_{orth} = \begin{pmatrix} C_{11} & C_{12} & C_{13} & 0 & 0 & 0 \\ & C_{22} & C_{23} & 0 & 0 & 0 \\ & & C_{33} & 0 & 0 & 0 \\ & & & C_{44} & 0 & 0 \\ & \textbf{sym.} & & & C_{55} & 0 \\ & & & & & C_{66} \end{pmatrix} \tag{A-2}$$

The elastic tensor of monoclinic media can be expressed as:

$$\mathbf{C}_{mono} = \begin{pmatrix} C_{11} & C_{12} & C_{13} & 0 & 0 & C_{16} \\ & C_{22} & C_{23} & 0 & 0 & C_{26} \\ & & C_{33} & 0 & 0 & C_{36} \\ & & & C_{44} & C_{45} & 0 \\ & \textbf{sym.} & & & C_{55} & 0 \\ & & & & & C_{66} \end{pmatrix} \tag{A-3}$$

Appendix B

Linear regression solution of the amplitude ratio

In this appendix, we introduce the linear regression least-square solution of the ratio equation.
We first use the time-frequency transformation method (e.g the wavelet transformation) to obtain the time-frequency spectra of translational displacement and rotation or radial strain, which have been successfully used in previous studies (Igel et al., 2007; Kurrle et al., 2010), and then combine the least-square algorithm to calculate the dispersion curves. We use the dispersion eq. 2.17 of isotropic media as an example to demonstrate how to calculate a stable phase velocity. In the time-frequency spectra, eq. 2.17 can be expressed as

$$c_L(\omega) = |\frac{\dot{u}_t(\omega, t_i)}{2\Omega_z(\omega, t_i)}| \tag{B-1}$$

Where $t_i (i = 1..N)$ represents any time point in the time window for quasi-Love wave. N is the number of data points. Eq. B-1 is written in the form of a matrix

$$G_0 m = d_0 \tag{B-2}$$

Where $G_0 = 2[|\Omega_z(\omega, t_1)|, \ldots, |\Omega_z(\omega, t_N)|]^T$, $m = c_L(\omega)$ and $d_0 = [|\dot{u}_t(\omega, t_1)|, \ldots, |\dot{u}_t(\omega, t_N)|]^T$.
To select the appropriate data point, we introduce a weight function $wf(\omega, t_i)$ for each data point whose value is equal to 1 or 0. Consequently, eq. B-2 can be given as

$$Gm = d \tag{B-3}$$

Where $G = 2[wf(\omega, t_1)|\Omega_z(\omega, t_1)|, \ldots, wf(\omega, t_N)|\Omega_z(\omega, t_N)|]^T$.
And $d = [wf(\omega, t_1)|\dot{u}_t(\omega, t_1)|, \ldots, wf(\omega, t_N)|\dot{u}_t(\omega, t_N)|]^T$. Consequently, the least-square solution of eq. B-3 can be expressed as;

$$c_L(\omega) = \frac{\sum_{i=1}^{N} wf(\omega, t_i)^2 |\Omega_z(\omega, t_i)\dot{u}_t(\omega, t_i)|}{2\sum_{i=1}^{N} wf(\omega, t_i)^2 \Omega_z(\omega, t_i)^2} \tag{B-4}$$

When $wf(\omega, t_i)$ is equal to 0 which means that we remove this data point.

Appendix C

Polarization of rotation and strain in anisotropic media

In isotropic media, the polarization of rotation and strain at the surface ($z = 0$) can be expressed in Cartesian coordinate as:
For the Love wave;

$$\begin{cases} \Omega_x = 0 \\ \Omega_y = 0 \\ \Omega_z = i\kappa_{l0}W/2 \end{cases} \tag{C-1}$$

$$\begin{cases} \varepsilon_{xx} = -i\kappa_{l0}sin\psi cos\psi W \\ \varepsilon_{yy} = i\kappa_{l0}sin\psi cos\psi W \\ \varepsilon_{zz} = 0 \\ \varepsilon_{xy} = iW\kappa_{l0}(cos\psi^2 - sin\psi^2)/2 \\ \varepsilon_{xz} = 0 \\ \varepsilon_{yz} = 0 \end{cases} \tag{C-2}$$

For the Rayleigh wave;

$$\begin{cases} \Omega_x = -\kappa_{r0}sin\psi U \\ \Omega_y = \kappa_{r0}cos\psi U \\ \Omega_z = 0 \end{cases} \tag{C-3}$$

$$\begin{cases} \varepsilon_{xx} = i\kappa_{r0}cos\psi^2 V \\ \varepsilon_{yy} = i\kappa_{r0}sin\psi^2 V \\ \varepsilon_{zz} = -\frac{\lambda}{(\lambda+2\mu)}i\kappa_{r0}V \\ \varepsilon_{xy} = i\kappa_{r0}sin\psi cos\psi V \\ \varepsilon_{xz} = 0 \\ \varepsilon_{yz} = 0 \end{cases} \tag{C-4}$$

where we again omit the exponential term $e^{i\kappa(cos\psi x + sin\psi y) - i\omega t}$. For the sake of simplicity, the following derivation will also omit the term.
In orthorhombic media, the polarization of rotation and strain at the surface ($z = 0$) can

be expressed in Cartesian coordinate as
For the quasi-Love wave;

$$\begin{cases} \Omega_x = -\kappa_l sin\psi TU \\ \Omega_y = \kappa_l cos\psi TU \\ \Omega_z = i\kappa_l W/2 \end{cases} \tag{C-5}$$

$$\begin{cases} \varepsilon_{xx} = -i\kappa_l cos\psi(cos\psi TV - sin\psi W) \\ \varepsilon_{yy} = i\kappa_l sin\psi(sin\psi TV + cos\psi W) \\ \varepsilon_{zz} = -\frac{C_{13}}{C_{33}} i\kappa_l cos\psi(cos\psi TV - sin\psi W) - \frac{C_{23}}{C_{33}} i\kappa_l sin\psi(sin\psi TV + cos\psi W) \\ \varepsilon_{xy} = i\kappa_l(2sin\psi cos\psi TV + cos\psi^2 W - sin\psi^2 W)/2 \\ \varepsilon_{xz} = 0 \\ \varepsilon_{yz} = 0 \end{cases} \tag{C-6}$$

For the quasi-Rayleigh wave;

$$\begin{cases} \Omega_x = -\kappa_r sin\psi U \\ \Omega_y = \kappa_r cos\psi U \\ \Omega_z = -i\kappa_r TW/2 \end{cases} \tag{C-7}$$

$$\begin{cases} \varepsilon_{xx} = i\kappa_r cos\psi(cos\psi V + sin\psi TW) \\ \varepsilon_{yy} = i\kappa_r sin\psi(sin\psi V - cos\psi TW) \\ \varepsilon_{zz} = -\frac{C_{13}}{C_{33}} i\kappa_r cos\psi(cos\psi V + sin\psi TW) - \frac{C_{23}}{C_{33}} i\kappa_r sin\psi(sin\psi V - cos\psi TW) \\ \varepsilon_{xy} = i\kappa_r(2sin\psi cos\psi V - cos\psi^2 TW + sin\psi^2 TW)/2 \\ \varepsilon_{xz} = 0 \\ \varepsilon_{yz} = 0 \end{cases} \tag{C-8}$$

In general anisotropic media, the polarization of rotation and strain at the surface ($z = 0$) can be expressed in Cartesian coordinate as
For the quasi-Love wave;

$$\begin{cases} \Omega_x = -(\kappa_l sin\psi TU + cos\psi W' + sin\psi TV')/2 \\ \Omega_y = (cos\psi TV' + \kappa_l cos\psi TU - sin\psi W')/2 \\ \Omega_z = i\kappa_l W/2 \end{cases} \tag{C-9}$$

$$\begin{cases} \varepsilon_{xx} = i\kappa_l cos\psi(cos\psi TV - sin\psi W) \\ \varepsilon_{yy} = i\kappa_l sin\psi(sin\psi TV + cos\psi W) \\ \varepsilon_{zz} = -\frac{i\kappa_l}{C_{33}}[C_{13}(-sin\psi cos\psi W + cos\psi^2 TV) + C_{23}(sin\psi cos\psi W + sin\psi^2 TV) + \\ \frac{C_{36}}{2}(2sin\psi cos\psi TV + cos\psi^2 W - sin\psi^2 W)] \\ \varepsilon_{xy} = i\kappa_l(2sin\psi cos\psi TV + cos\psi^2 W - sin\psi^2 W)/2 \\ \varepsilon_{xz} = (cos\psi TV' - \kappa_l cos\psi TU - sin\psi W')/2 \\ \varepsilon_{yz} = (cos\psi W' + sin\psi TV' - T\kappa_l sin\psi U)/2 \end{cases} \tag{C-10}$$

For the quasi-Rayleigh wave;

$$\begin{cases} \Omega_x = -(\kappa_r sin\psi U - cos\psi TW' + sin\psi V')/2 \\ \Omega_y = (cos\psi V' + \kappa_r cos\psi U + sin\psi TW')/2 \\ \Omega_z = -i\kappa_r TW/2 \end{cases} \tag{C-11}$$

$$\begin{cases} \varepsilon_{xx} = i\kappa_r cos\psi(cos\psi V + sin\psi TW) \\ \varepsilon_{yy} = i\kappa_r sin\psi(sin\psi V - cos\psi TW) \\ \varepsilon_{zz} = -\frac{i\kappa_r}{C_{33}}[C_{13}(cos\psi^2 V + sin\psi cos\psi TW) + C_{23}(-sin\psi cos\psi TW + sin\psi^2 V) + \\ \frac{C_{36}}{2}(2sin\psi cos\psi V + (sin\psi^2 - cos\psi^2)TW)] \\ \varepsilon_{xy} = i\kappa_r(2sin\psi cos\psi V - cos\psi^2 TW + sin\psi^2 TW)/2 \\ \varepsilon_{xz} = (cos\psi V' - \kappa_r cos\psi U + sin\psi TW')/2 \\ \varepsilon_{yz} = (-cos\psi TW' + sin\psi V' - \kappa_r sin\psi U)/2 \end{cases} \tag{C-12}$$

It should be noted that under the free surface boundary condition, $W'(0) = \partial_z W|_{z=0} = \sigma_{yz} = 0$ in the reference isotropic media (Takeuchi & Saito, 1972).

Bibliography

Aki, K., 1957. Space and time spectra of stationary stochastic waves, with special reference to microtremors, *Bulletin of the Earthquake Research Institute*, **35**, 415–456.

Aki, K. & Richards, P. G., 2002. *Quantitative seismology*.

Al-Lazki, A. I., Sandvol, E., Seber, D., Barazangi, M., Turkelli, N., & Mohamad, R., 2004. Pn tomographic imaging of mantle lid velocity and anisotropy at the junction of the arabian, eurasian and african plates, *Geophysical Journal International*, **158**(3), 1024–1040.

Albuquerque Seismological Laboratory (ASL)/USGS, 1990. United states national seismic network.

Alvizuri, C. & Tanimoto, T., 2011. Azimuthal anisotropy from array analysis of rayleigh waves in southern california, *Geophysical Journal International*, **186**(3), 1135–1151 [Dataset].

Anderson, D. L., 1965. Recent evidence concerning the structure and composition of the earth's mantle, *Physics and Chemistry of the Earth*, **6**, 1–131.

Anderson, D. L. & Dziewonski, A. M., 1982. Upper mantle anisotropy: evidence from free oscillations, *Geophysical Journal International*, **69**(2), 383–404.

Anderson, D. L., Minster, B., & Cole, D., 1974. The effect of oriented cracks on seismic velocities, *Journal of Geophysical Research*, **79**(26), 4011–4015.

Ardhuin, F., Stutzmann, E., Schimmel, M., & Mangeney, A., 2011. Ocean wave sources of seismic noise, *Journal of Geophysical Research: Oceans*, **116**(C9).

Ardhuin, F., Gualtieri, L., & Stutzmann, E., 2015. How ocean waves rock the earth: Two mechanisms explain microseisms with periods 3 to 300 s, *Geophysical Research Letters*, **42**(3), 765–772.

Ardhuin, F., Gualtieri, L., Stutzmann, E., Nakata, N., & Fichtner, A., 2019. Physics of ambient noise generation by ocean waves, *Seismic ambient noise*, pp. 69–108.

Arizona Geological Survey, 2007. Arizona broadband seismic network.

Aster, R. C. & Shearer, P. M., 1991. High-frequency borehole seismograms recorded in the san jacinto fault zone, southern california. part 1. polarizations, *Bulletin of the Seismological Society of America*, **81**(4), 1057–1080.

Atwater, T. M., 1998. Plate tectonic history of southern california with emphasis on the western transverse ranges and northern channel islands.

Barbot, S., 2020. Mantle flow distribution beneath the california margin, *Nature Communications*, **11**(1), 4456 [Dataset].

Barruol, G., Wuestefeld, A., & Bokelmann, G., 2009. Sks-splitting database, *Université de Montpellier, Laboratoire Géosciences*, p. [Dataset].

Becker, T. W., Lebedev, S., & Long, M., 2012. On the relationship between azimuthal anisotropy from shear wave splitting and surface wave tomography, *Journal of Geophysical Research: Solid Earth*, **117**(B1).

Bensen, G., Ritzwoller, M., Barmin, M., Levshin, A. L., Lin, F., Moschetti, M., Shapiro, N., & Yang, Y., 2007. Processing seismic ambient noise data to obtain reliable broadband surface wave dispersion measurements, *Geophysical journal international*, **169**(3), 1239–1260.

Bernauer, F., Behnen, K., Wassermann, J., Egdorf, S., Igel, H., Donner, S., Stammler, K., Hoffmann, M., Edme, P., Sollberger, D., et al., 2021. Rotation, strain, and translation sensors performance tests with active seismic sources, *Sensors*, **21**(1), 264.

Boness, N. L. & Zoback, M. D., 2004. Stress-induced seismic velocity anisotropy and physical properties in the safod pilot hole in parkfield, ca, *Geophysical Research Letters*, **31**(15).

Boness, N. L. & Zoback, M. D., 2006. Mapping stress and structurally controlled crustal shear velocity anisotropy in california, *Geology*, **34**(10), 825–828.

Botev, Z. I., Grotowski, J. F., & Kroese, D. P., 2010. Kernel density estimation via diffusion, *The annals of Statistics*, **38**(5), 2916–2957.

Brotzer, A., Igel, H., Stutzmann, E., Montagner, J., Bernauer, F., Wassermann, J., Widmer-Schnidrig, R., Lin, C., Kiselev, S., Vernon, F., & Schreiber, K. U., 2023. Characterizing the Background Noise Level of Rotational Ground Motions on Earth, *Seismological Research Letters*.

Brotzer, A., Igel, H., Stutzmann, E., Montagner, J.-P., Bernauer, F., Wassermann, J., Widmer-Schnidrig, R., Lin, C.-J., Kiselev, S., Vernon, F., et al., 2024. Characterizing the background noise level of rotational ground motions on earth, *Seismological Research Letters*, **95**(3), 1858–1869.

Brown, M., Lin, G., Matsuzawa, H., & Yoshizawa, K., 2022. Recovery of love wave overtone waveforms and dispersion curves from single-station seismograms using time-warping, *Geophysical Journal International*, **230**(1), 70–83.

California Institute of Technology and United States Geological Survey Pasadena, 1926. Southern california seismic network.

Campillo, M., Roux, P., & Shapiro, N. M., 2011. *Seismic, Ambient Noise Correlation*, pp. 1230–1236, Springer Netherlands, Dordrecht.

Centro de Investigación Científica y de Educación Superior de Ensenada (CICESE), Ensenada, 1980. Red sísmica del noroeste de méxico.

Chen, X., 1993. A systematic and efficient method of computing normal modes for multilayered half-space, *Geophysical Journal International*, **115**(2), 391–409.

Chen, X., 1999. Seismogram synthesis in multi-layered half-space, *Earthquake Research in China*, **13**(2).

Chou, P. C. & Pagano, N. J., 1992. *Elasticity: tensor, dyadic, and engineering approaches*, Courier Corporation.

Cliford, A., 1973. Multivariate error analysis: A handbook of error propagation and calculation in many-parameter systems.

Colosi, L. V., Villas Bôas, A. B., & Gille, S. T., 2021. The seasonal cycle of significant wave height in the ocean: Local versus remote forcing, *Journal of Geophysical Research: Oceans*, **126**(8), e2021JC017198.

Crampin, S., 1977. A review of the effects of anisotropic layering on the propagation of seismic waves, *Geophysical Journal International*, **49**(1), 9–27.

Crampin, S., 1978. Seismic-wave propagation through a cracked solid: polarization as a possible dilatancy diagnostic, *Geophysical Journal International*, **53**(3), 467–496.

Crampin, S. & Chastin, S., 2003. A review of shear wave splitting in the crack-critical crust, *Geophysical Journal International*, **155**(1), 221–240.

Crampin, S. & Lovell, J. H., 1991. A decade of shear-wave splitting in the earth's crust: what does it mean? what use can we make of it? and what should we do next?, *Geophysical Journal International*, **107**(3), 387–407.

Crampin, S., Evans, R., Üçer, B., Doyle, M., Davis, J. P., Yegorkina, G. V., & Miller, A., 1980. Observations of dilatancy-induced polarization anomalies and earthquake prediction, *Nature*, **286**(5776), 874–877.

Donner, S., Lin, C.-J., Hadziioannou, C., Gebauer, A., Vernon, F., Agnew, D. C., Igel, H., Schreiber, U., & Wassermann, J., 2017. Comparing direct observation of strain, rotation, and displacement with array estimates at piñon flat observatory, california, *Seismological Research Letters*, **88**(4), 1107–1116.

Dziewonski, A. M. & Anderson, D. L., 1981. Preliminary reference earth model, *Physics of the earth and planetary interiors*, **25**(4), 297–356.

Ekström, G., Tromp, J., & Larson, E. W., 1997. Measurements and global models of surface wave propagation, *Journal of Geophysical Research: Solid Earth*, **102**(B4), 8137–8157.

Fang, X. & Tang, L., 2021. A single station approach for subsurface anomaly detection, in *SEG/AAPG/SEPM First International Meeting for Applied Geoscience & Energy*, OnePetro.

Fang, X., Fehler, M. C., Zhu, Z., Zheng, Y., & Burns, D. R., 2014. Reservoir fracture characterization from seismic scattered waves, *Geophysical Journal International*, **196**(1), 481–492.

Fichtner, A. & Igel, H., 2009. Sensitivity densities for rotational ground-motion measurements, *Bulletin of the Seismological Society of America*, **99**(2B), 1302–1314.

Forsyth, D. W., 1975. The early structural evolution and anisotropy of the oceanic upper mantle, *Geophysical Journal International*, **43**(1), 103–162.

Forsyth, D. W., Li, A., Levander, A., & Nolet, G., 2005. Array analysis of two-dimensional variations in surface wave phase velocity and azimuthal anisotropy in the presence of multipathing interference, *GEOPHYSICAL MONOGRAPH-AMERICAN GEOPHYSICAL UNION*, **157**, 81.

Francis, T., 1969. Generation of seismic anisotropy in the upper mantle along the mid-oceanic ridges, *Nature*, **221**(5176), 162–165.

Frank Vernon, 1982. Anza regional network.

Frank Vernon, 2014. Piñon flats observatory array.

Fukao, Y., Nishida, K., & Kobayashi, N., 2010. Seafloor topography, ocean infragravity waves, and background love and rayleigh waves, *Journal of Geophysical Research: Solid Earth*, **115**(B4).

Ghosh, A. & Holt, W. E., 2012. Plate motions and stresses from global dynamic models, *Science*, **335**(6070), 838–843.

Gripp, A. E. & Gordon, R. G., 2002. Young tracks of hotspots and current plate velocities, *Geophysical Journal International*, **150**(2), 321–361.

Grob, M., Maggi, A., & Stutzmann, E., 2011. Observations of the seasonality of the antarctic microseismic signal, and its association to sea ice variability, *Geophysical Research Letters*, **38**(11).

Gualtieri, L., Bachmann, E., Simons, F. J., & Tromp, J., 2020. The origin of secondary microseism love waves, *Proceedings of the National Academy of Sciences*, **117**(47), 29504–29511.

Gualtieri, L., Bachmann, E., Simons, F. J., & Tromp, J., 2021. Generation of secondary microseism love waves: Effects of bathymetry, 3-d structure and source seasonality, *Geophysical Journal International*, **226**(1), 192–219.

Gupta, I. N., 1973. Premonitory variations in s-wave velocity anisotropy before earthquakes in nevada, *Science*, **182**(4117), 1129–1132.

Hadziioannou, C., Gaebler, P., Schreiber, U., Wassermann, J., & Igel, H., 2012. Examining ambient noise using colocated measurements of rotational and translational motion, *Journal of seismology*, **16**, 787–796.

Haney, M. M., Mikesell, T. D., van Wijk, K., & Nakahara, H., 2012. Extension of the spatial autocorrelation (spac) method to mixed-component correlations of surface waves, *Geophysical Journal International*, **191**(1), 189–206.

Hasselmann, K., 1963. A statistical analysis of the generation of microseisms, *Reviews of Geophysics*, **1**(2), 177–210.

Heidbach, O., Tingay, M., Barth, A., Reinecker, J., Kurfeß, D., & Müller, B., 2010. Global crustal stress pattern based on the world stress map database release 2008, *Tectonophysics*, **482**(1-4), 3–15.

Hess, H., 1964. Seismic anisotropy of the uppermost mantle under oceans, *Nature*, **203**(4945), 629–631.

Humphreys, E., Clayton, R. W., & Hager, B. H., 1984. A tomographic image of mantle structure beneath southern california, *Geophysical Research Letters*, **11**(7), 625–627.

Igel, H., Schreiber, U., Flaws, A., Schuberth, B., Velikoseltsev, A., & Cochard, A., 2005. Rotational motions induced by the m8. 1 tokachi-oki earthquake, september 25, 2003, *Geophysical research letters*, **32**(8).

Igel, H., Cochard, A., Wassermann, J., Flaws, A., Schreiber, U., Velikoseltsev, A., & Pham Dinh, N., 2007. Broad-band observations of earthquake-induced rotational ground motions, *Geophysical Journal International*, **168**(1), 182–196.

Igel, H., Schreiber, K. U., Gebauer, A., Bernauer, F., Egdorf, S., Simonelli, A., Lin, C.-J., Wassermann, J., Donner, S., Hadziioannou, C., Yuan, S., Brotzer, A., Kodet, J., Tanimoto, T., Hugentobler, U., & Wells, J.-P. R., 2021. ROMY: a multicomponent ring laser for geodesy and geophysics, *Geophysical Journal International*, **225**(1), 684–698.

Iyer, H., 1958. A study on the direction of arrival of microseisms at kew observatory, *Geophysical Journal International*, **1**(1), 32–43.

Karato, S.-i., 2012. On the origin of the asthenosphere, *Earth and Planetary Science Letters*, **321**, 95–103.

Keil, S., Wassermann, J., & Igel, H., 2021. Single-station seismic microzonation using 6c measurements, *Journal of Seismology*, **25**(1), 103–114.

Kohler, M. D., 1999. Lithospheric deformation beneath the san gabriel mountains in the southern california transverse ranges, *Journal of Geophysical Research: Solid Earth*, **104**(B7), 15025–15041.

Kurrle, D., Igel, H., Ferreira, A. M., Wassermann, J., & Schreiber, U., 2010. Can we estimate local love wave dispersion properties from collocated amplitude measurements of translations and rotations?, *Geophysical research letters*, **37**(4).

Le Pape, F., Craig, D., & Bean, C. J., 2021. How deep ocean-land coupling controls the generation of secondary microseism love waves, *Nature Communications*, **12**(1), 2332.

Lefevre, H. C., 2014. *The fiber-optic gyroscope*, Artech house.

Legendre, C. P., Zhao, L., & Tseng, T.-L., 2021. Large-scale variation in seismic anisotropy in the crust and upper mantle beneath anatolia, turkey, *Communications Earth & Environment*, **2**(1), 1–7.

Levshin, A. L., Pisarenko, V., & Pogrebinsky, G., 1972. On a frequency-time analysis of oscillations, in *Annales de geophysique*, vol. 28, pp. 211–218, Centre National de la Recherche Scientifique.

Lobkis, O. I. & Weaver, R. L., 2001. On the emergence of the green's function in the correlations of a diffuse field, *The Journal of the Acoustical Society of America*, **110**(6), 3011–3017.

Longuet-Higgins, M. S., 1950. A theory of the origin of microseisms, *Philosophical Transactions of the Royal Society of London. Series A, Mathematical and Physical Sciences*, **243**(857), 1–35.

Mao, S., Lecointre, A., van der Hilst, R. D., & Campillo, M., 2022. Space-time monitoring of groundwater fluctuations with passive seismic interferometry, *Nature Communications*, **13**(1), 4643.

Marone, F. & Romanowicz, B., 2007. The depth distribution of azimuthal anisotropy in the continental upper mantle, *Nature*, **447**(7141), 198–201 [Dataset].

Maupin, V., 1989. Surface waves in weakly anisotropic structures: on the use of ordinary or quasi-degenerate perturbation methods, *Geophysical Journal International*, **98**(3), 553–563.

Maupin, V., 2004. Comment on 'the azimuthal dependence of surface wave polarization in a slightly anisotropic medium'by t. tanimoto, *Geophysical Journal International*, **159**(1), 365–368.

Mochizuki, E., 1986. The free oscillations of an anisotropic and heterogeneous earth, *Geophysical Journal International*, **86**(1), 167–176.

Montagner, J.-P., 1994. Can seismology tell us anything about convection in the mantle?, *Reviews of Geophysics*, **32**(2), 115–137.

Montagner, J.-P. & Nataf, H.-C., 1986. A simple method for inverting the azimuthal anisotropy of surface waves, *Journal of Geophysical Research: Solid Earth*, **91**(B1), 511–520.

Montagner, J.-P. & Tanimoto, T., 1991. Global upper mantle tomography of seismic velocities and anisotropies, *Journal of Geophysical Research: Solid Earth*, **96**(B12), 20337–20351.

Mutlu, A. K. & Karabulut, H., 2011. Anisotropic pn tomography of turkey and adjacent regions, *Geophysical Journal International*, **187**(3), 1743–1758.

Nakahara, H., Emoto, K., & Nishimura, T., 2021. Extending the formulation of the spatial autocorrelation (spac) method to strain, rotation and tilt, *Geophysical Journal International*, **227**(1), 287–302.

Nataf, H.-C., Nakanishi, I., & Anderson, D. L., 1984. Anisotropy and shear-velocity heterogeneities in the upper mantle, *Geophysical Research Letters*, **11**(2), 109–112.

Noe, S., Yuan, S., Montagner, J., & Igel, H., 2022. Anisotropic elastic parameter estimation from multicomponent ground-motion observations: a theoretical study, *Geophysical Journal International*, **229**(2), 1462–1473.

Obrebski, M., Ardhuin, F., Stutzmann, E., & Schimmel, M., 2012. How moderate sea states can generate loud seismic noise in the deep ocean, *Geophysical Research Letters*, **39**(11).

Paitz, P., Sager, K., & Fichtner, A., 2019. Rotation and strain ambient noise interferometry, *Geophysical Journal International*, **216**(3), 1938–1952.

Pancha, A., Webb, T., Stedman, G., McLeod, D., & Schreiber, K., 2000. Ring laser detection of rotations from teleseismic waves, *Geophysical Research Letters*, **27**(21), 3553–3556.

Park, J. & Yu, Y., 1993. Seismic determination of elastic anisotropy and mantle flow, *Science*, **261**(5125), 1159–1162.

Pedersen, H. A., 2006. Impacts of non-plane waves on two-station measurements of phase velocities, *Geophysical Journal International*, **165**(1), 279–287.

Pelaez Quiñones, J., Becker, D., & Hadziioannou, C., 2023. Beamforming of rayleigh and love waves in the course of atlantic cyclones, *Journal of Geophysical Research: Solid Earth*, **128**(2).

Pham, N. D., Igel, H., de la Puente, J., Käser, M., & Schoenberg, M. A., 2010. Rotational motions in homogeneous anisotropic elastic media, *Geophysics*, **75**(5), D47–D56.

Ribe, N. M., 1989. Seismic anisotropy and mantle flow, *Journal of Geophysical Research: Solid Earth*, **94**(B4), 4213–4223.

Richter, T., Sens-Schönfelder, C., Kind, R., & Asch, G., 2014. Comprehensive observation and modeling of earthquake and temperature-related seismic velocity changes in northern chile with passive image interferometry, *Journal of Geophysical Research: Solid Earth*, **119**(6), 4747–4765.

Rind, D. & Down, W., 1979. Microseisms at palisades: 2. rayleigh wave and love wave characteristics and the geologic control of propagation, *Journal of Geophysical Research: Solid Earth*, **84**(B10), 5632–5642.

Roux, P., 2009. Passive seismic imaging with directive ambient noise: application to surface waves and the san andreas fault in parkfield, ca, *Geophysical Journal International*, **179**(1), 367–373.

Saade, M., Montagner, J., Roux, P., Cupillard, P., Durand, S., & Brenguier, F., 2015. Influence of seismic anisotropy on the cross correlation tensor: numerical investigations, *Geophysical Journal International*, **201**(2), 595–604.

Saito, T., 2010. Love-wave excitation due to the interaction between a propagating ocean wave and the sea-bottom topography, *Geophysical Journal International*, **182**(3), 1515–1523.

Savage, M., 1999. Seismic anisotropy and mantle deformation: what have we learned from shear wave splitting?, *Reviews of Geophysics*, **37**(1), 65–106.

SCEDC, 2013. Southern california earthquake center. caltech [dataset]. https://doi:10.7909/c3wd3xh1.

Schimmel, M., Stutzmann, E., Ardhuin, F., & Gallart, J., 2011. Polarized earth's ambient microseismic noise, *Geochemistry, Geophysics, Geosystems*, **12**(7).

Schmandt, B. & Humphreys, E., 2010. Seismic heterogeneity and small-scale convection in the southern california upper mantle, *Geochemistry, Geophysics, Geosystems*, **11**(5).

Schmelzbach, C., Donner, S., Igel, H., Sollberger, D., Taufiqurrahman, T., Bernauer, F., Häusler, M., Van Renterghem, C., Wassermann, J., & Robertsson, J., 2018. Advances in 6c seismology: Applications of combined translational and rotational motion measurements in global and exploration seismology, *Geophysics*, **83**(3), WC53–WC69.

Schreiber, K., Velikoseltsev, A., Carr, A., & Franco-Anaya, R., 2009. The application of fiber optic gyroscopes for the measurement of rotations in structural engineering, *Bulletin of the Seismological Society of America*, **99**(2B), 1207–1214.

Schreiber, K., Gebauer, A., Igel, H., Wassermann, J., Hurst, R. B., & Wells, J.-P. R., 2014. The centennial of the sagnac experiment in the optical regime: From a tabletop experiment to the variation of the earth's rotation, *Comptes Rendus Physique*, **15**(10), 859–865.

Schreiber, U., Igel, H., Cochard, A., & Velikoseltsev, A., 2005. The geosensor project: Rotations observable for seismology, *Observation of the Earth System from Space*, p. 427.

Schröer, C., 2019. *Locating oceanic noise sources around the Pinon Flat Observatory using Rotational Seismology and Three-Component Beamforming*, Master's thesis, University of Hamburg, [Dataset].

Schulte-Pelkum, V., Masters, G., & Shearer, P. M., 2001. Upper mantle anisotropy from long-period p polarization, *Journal of Geophysical Research: Solid Earth*, **106**(B10), 21917–21934.

Schulte-Pelkum, V., Earle, P. S., & Vernon, F. L., 2004. Strong directivity of ocean-generated seismic noise, *Geochemistry, Geophysics, Geosystems*, **5**(3).

Shabtian, H. S., Eilon, Z. C., & Tanimoto, T., 2024. Seasonality of california central coast microseisms, *Bulletin of the Seismological Society of America*, **114**(2), 873–881.

Shapiro, N. M. & Campillo, M., 2004. Emergence of broadband rayleigh waves from correlations of the ambient seismic noise, *Geophysical Research Letters*, **31**(7).

Shapiro, N. M., Campillo, M., Stehly, L., & Ritzwoller, M. H., 2005. High-resolution surface-wave tomography from ambient seismic noise, *Science*, **307**(5715), 1615–1618.

Shaw, J. H., Plesch, A., Tape, C., Suess, M. P., Jordan, T. H., Ely, G., Hauksson, E., Tromp, J., Tanimoto, T., Graves, R., et al., 2015. Unified structural representation of the southern california crust and upper mantle, *Earth and Planetary Science Letters*, **415**, 1–15.

Silver, P. G., 1996. Seismic anisotropy beneath the continents: Probing the depths of geology, *Annual review of earth and planetary sciences*, **24**(1), 385–432.

Silver, P. G. & Chan, W. W., 1988. Implications for continental structure and evolution from seismic anisotropy, *Nature*, **335**(6185), 34–39.

Smith, M. L. & Dahlen, F., 1973. The azimuthal dependence of love and rayleigh wave propagation in a slightly anisotropic medium, *Journal of Geophysical Research*, **78**(17), 3321–3333.

Sollberger, D., Greenhalgh, S. A., Schmelzbach, C., Van Renterghem, C., & Robertsson, J. O., 2018. 6-c polarization analysis using point measurements of translational and rotational ground-motion: theory and applications, *Geophysical Journal International*, **213**(1), 77–97.

Spudich, P. & Fletcher, J. B., 2008. Observation and prediction of dynamic ground strains, tilts, and torsions caused by the m w 6.0 2004 parkfield, california, earthquake and aftershocks, derived from upsar array observations, *Bulletin of the Seismological Society of America*, **98**(4), 1898–1914.

Spudich, P., Steck, L. K., Hellweg, M., Fletcher, J., & Baker, L. M., 1995. Transient stresses at parkfield, california, produced by the m 7.4 landers earthquake of june 28, 1992: Observations from the upsar dense seismograph array, *Journal of Geophysical Research: Solid Earth*, **100**(B1), 675–690.

Stehly, L., Campillo, M., & Shapiro, N., 2006. A study of the seismic noise from its long-range correlation properties, *Journal of Geophysical Research: Solid Earth*, **111**(B10).

Stehly, L., Fry, B., Campillo, M., Shapiro, N., Guilbert, J., Boschi, L., & Giardini, D., 2009. Tomography of the alpine region from observations of seismic ambient noise, *Geophysical Journal International*, **178**(1), 338–350.

Stutzmann, E., Ardhuin, F., Schimmel, M., Mangeney, A., & Patau, G., 2012. Modelling long-term seismic noise in various environments, *Geophysical Journal International*, **191**(2), 707–722.

Takeuchi, H. & Saito, M., 1972. Seismic surface waves, *Methods in computational physics*, **11**, 217–295.

Tang, L. & Fang, X., 2021a. Generation of 6-c synthetic seismograms in stratified vertically transversely isotropic media using a generalized reflection and transmission coefficient method, *Geophysical Journal International*, **225**(3), 1554–1585.

Tang, L. & Fang, X., 2021b. Numerical study of the application of six-component ambient seismic noise data for high-resolution imaging of lateral heterogeneities, in *SEG/AAPG/SEPM First International Meeting for Applied Geoscience & Energy*, OnePetro.

Tang, L. & Fang, X., 2023. Application of six-component ambient seismic noise data for high-resolution imaging of lateral heterogeneities, *Geophysical Journal International*, **232**(3), 1756–1784.

Tang, L., Igel, H., & Montagner, J.-P., 2023a. Anisotropy and deformation processes in southern california from rotational observations, *Geophysical Research Letters*, **50**(23), e2023GL105970.

Tang, L., Igel, H., & Montagner, J.-P., 2023b. Seismic anisotropy from 6c observations, Tech. rep., Copernicus Meetings.

Tang, L., Igel, H., & Montagner, J.-P., 2023c. Single-point dispersion measurement of surface waves combining translation, rotation and strain in weakly anisotropic media: theory, *Geophysical Journal International*, **235**(1), 24–47.

Tang, L., Igel, H., Montagner, J.-P., & Vernon, F., 2024. Seismic anisotropy from 6c ground motions of ambient seismic noise, *Journal of Geophysical Research: Solid Earth*, **129**(6), e2024JB028959.

tangle0129, 2023. spin-itn/6c_anisotropy: Anisotropy_rotation.

Tanimoto, T., 1986. Free oscillations of a slightly anisotropic earth, *Geophysical Journal International*, **87**(2), 493–517.

Tanimoto, T., 2004. The azimuthal dependence of surface wave polarization in a slightly anisotropic medium, *Geophysical Journal International*, **156**(1), 73–78.

Tanimoto, T. & Anderson, D. L., 1984. Mapping convection in the mantle, *Geophysical Research Letters*, **11**(4), 287–290.

Tanimoto, T. & Anderson, D. L., 1985. Lateral heterogeneity and azimuthal anisotropy of the upper mantle: Love and rayleigh waves 100–250 s, *Journal of Geophysical Research: Solid Earth*, **90**(B2), 1842–1858.

Tanimoto, T. & Prindle, K., 2007. Surface wave analysis with beamforming, *Earth, planets and space*, **59**, 453–458.

Tanimoto, T. & Wang, J., 2021. Incorporating wind information in the inversion of co-located pressure and seismic data for shallow elastic structure, *Journal of Geophysical Research: Solid Earth*, **126**(5), e2020JB021162.

Tanimoto, T., Ishimaru, S., & Alvizuri, C., 2006. Seasonality in particle motion of microseisms, *Geophysical Journal International*, **166**(1), 253–266.

Tanimoto, T., Hadziioannou, C., Igel, H., Wassermann, J., Schreiber, U., Gebauer, A., & Chow, B., 2016. Seasonal variations in the rayleigh-to-love wave ratio in the secondary microseism from colocated ring laser and seismograph, *Journal of Geophysical Research: Solid Earth*, **121**(4), 2447–2459.

Tape, C., Liu, Q., Maggi, A., & Tromp, J., 2009. Adjoint tomography of the southern california crust, *Science*, **325**(5943), 988–992.

Teanby, N., Kendall, J.-M., Jones, R., & Barkved, O., 2004. Stress-induced temporal variations in seismic anisotropy observed in microseismic data, *Geophysical Journal International*, **156**(3), 459–466.

Vinnik, L., Kosarev, G., & Makeyeva, L., 1984. Anisotropy of the lithosphere from the observations of sks and skks, in *Proc. Acad. Sci. USSR*, vol. 278, pp. 1335–1339.

Vinnik, L. P., Farra, V., & Romanowicz, B., 1989. Azimuthal anisotropy in the earth from observations of sks at geoscope and nars broadband stations, *Bulletin of the Seismological Society of America*, **79**(5), 1542–1558.

Wassermann, J., Wietek, A., Hadziioannou, C., & Igel, H., 2016. Toward a single-station approach for microzonation: Using vertical rotation rate to estimate love-wave dispersion curves and direction finding, *Bulletin of the Seismological Society of America*, **106**(3), 1316–1330.

Wassermann, J., Braun, T., Ripepe, M., Bernauer, F., Guattari, F., & Igel, H., 2022. The use of 6dof measurement in volcano seismology–a first application to stromboli volcano, *Journal of Volcanology and Geothermal Research*, **424**, 107499.

Wu, S., Jiang, C., Schulte-Pelkum, V., & Tong, P., 2022. Complex patterns of past and ongoing crustal deformations in southern california revealed by seismic azimuthal anisotropy, *Geophysical Research Letters*, **49**(15), e2022GL100233.

Yang, Y. & Forsyth, D. W., 2006. Rayleigh wave phase velocities, small-scale convection, and azimuthal anisotropy beneath southern california, *Journal of Geophysical Research: Solid Earth*, **111**(B7).

Yang, Z., Sheehan, A., & Shearer, P., 2011. Stress-induced upper crustal anisotropy in southern california, *Journal of Geophysical Research: Solid Earth*, **116**(B2).

Yao, H., van Der Hilst, R. D., & De Hoop, M. V., 2006. Surface-wave array tomography in se tibet from ambient seismic noise and two-station analysis—i. phase velocity maps, *Geophysical Journal International*, **166**(2), 732–744.

Yao, H., Beghein, C., & Van Der Hilst, R. D., 2008. Surface wave array tomography in se tibet from ambient seismic noise and two-station analysis-ii. crustal and upper-mantle structure, *Geophysical Journal International*, **173**(1), 205–219.

Yao, H., Van Der Hilst, R. D., & Montagner, J.-P., 2010. Heterogeneity and anisotropy of the lithosphere of se tibet from surface wave array tomography, *Journal of Geophysical Research: Solid Earth*, **115**(B12).

Yuan, S., Gessele, K., Gabriel, A.-A., May, D. A., Wassermann, J., & Igel, H., 2021. Seismic source tracking with six degree-of-freedom ground motion observations, *Journal of Geophysical Research: Solid Earth*, **126**(3), e2020JB021112.

Zembaty, Z., Bernauer, F., Igel, H., & Schreiber, K. U., 2021. Rotation rate sensors and their applications, *Sensors*, **21**(16).

Zhu, H. & Tromp, J., 2013. Mapping tectonic deformation in the crust and upper mantle beneath europe and the north atlantic ocean, *Science*, **341**(6148), 871–875.

Acknowledgements

Time flies, and three years of doctoral study have ended. I believe that my study results can contribute to the development of seismology, particularly in the area of rotational seismology. I have encountered numerous failures during these three years, but each unsuccessful attempt has brought me closer to success. Before starting my doctoral project, I was driven by curiosity to explore the development path of rotational seismology. Although I know it is a niche field with limited attention, I firmly believe it has the potential to become a broad research direction, especially regarding the technological breakthrough of reliable rotational seismometers.

My exploration and research path would not have been possible without the tolerance and support of several individuals. Firstly, I am deeply grateful to my parents for their unwavering support, which enabled me to pursue my doctoral degree far from home. A special thanks to Prof. Heiner Igel for his invaluable guidance and support throughout my doctoral project and his patience and care during my studies in Munich. His encouragement fueled my determination in research, and the moments spent discussing research outcomes with him are truly unforgettable. I am also grateful to Prof. Jean-Paul Montagner (IPGP, Paris) for co-supervising me during my doctoral career. His boundless curiosity and passion for anisotropy study genuinely inspired me. The SPIN project (https://spin-itn.eu/) deserves extended thanks for funding my doctoral research, and I appreciate Prof. Celine Hadziioannou's (University of Hamburg) contributions to the project. I also cherish the wonderful times spent with SPIN members, where we met, hiked, and dined together, allowing me to connect with a group of aspiring scientists. Even though the SPIN project is ending, the memories it has left me will be lifelong. I will carry them with me as I embark on a new, more challenging, and more beautiful journey.

This PhD project is funded by the European Union's Horizon 2020 research and innovation program under the Marie Skłodowska-Curie grant agreement No. 955515 (ITN SPIN).